DESIGN OF A CARDIOVASCULAR SIMULATION CIRCUIT DRIVEN BY TIME VARYING ELASTANCE

by

Doğan Onur Arısoy

B.Sc., Mechanical Engineering, Yıldız Technical University, 2012

B.Sc., Electrical Engineering, Yıldız Technical University, 2014

Submitted to the Institute of Biomedical Engineering

in partial fulfillment of the requirements

for the degree of

Master of Science

in

Biomedical Engineering

Boğaziçi University

2017

DESIGN OF A CARDIOVASCULAR SIMULATION CIRCUIT DRIVEN BY TIME VARYING ELASTANCE

APPROVED BY:

Prof. Dr. Cengizhan Öztürk .....
(Thesis Advisor)

Assoc. Prof. Dr. A. Kamuran Kadıpaşaoğlu .....
(Thesis Co-advisor)

Prof. Dr. Can Yücesoy .....

Prof. Dr. Ahmet Ademoğlu .....

Prof. Dr. Murat Sezer .....

DATE OF APPROVAL: 8 August 2017

ACKNOWLEDGMENTS

I would like to thank my advisor Cengizhan Öztürk for his support during my thesis. And I am extremely grateful to meet my co-advisor A. Kamuran Kadıpaşaoğlu. I am deeply indebted to him, for all the time he invested to teach me how to research and write a scientific paper.

I would also like to thank my colleagues Mehmet İşcan and Gamze Balkan for their support and contributions during my thesis.

I would like to thank my lifelong friends Kenan Müderrisoğlu, A. Oğuzhan Ahan, Berkay Volkaner, Semih Arıkan, Akın Şanlı, Taha Çalışkan, Kübra Gündüz and Deniz Yantemur for their support and encouragement.

I would also like to thank my close friends Günnur Onak, Çağla Özsoy, Çiğdem Özkolaçık, İlayda Duru and Alican Onur Çankaya. The times would not pass in BOUN BME without them.

I am grateful to have such a dedicated family who encouraged and supported me through all my life.

Finally, I would like to thank my dear soul mate, Burcu Arslan, for her support and being my safe heaven.

ACADEMIC ETHICS AND INTEGRITY STATEMENT

I, Doğan Onur Arısoy, hereby certify that I am aware of the Academic Ethics and Integrity Policy issued by the Council of Higher Education (YÖK) and I fully acknowledge all the consequences due to its violation by plagiarism or any other way.

Name :

Signature:

Date:

ABSTRACT

DESIGN OF A CARDIOVASCULAR SIMULATION CIRCUIT DRIVEN BY TIME VARYING ELASTANCE

Chronic Heart Failure (CHF) is a major cause of death for which only known non-palliative treatment is Heart Transplantation (HTx). Due to donor shortage, only a small cohort of people can be treated. Left Ventricular Assist Devices (LVADs) are widely used to sustain patients on the HTx waiting lists. LVADs are pumps that are implanted between the ventricular apex and ascending aorta, unloading the left ventricle. Before clinical use, LVADs must be thoroughly tested in-vitro, commonly with Cardiovascular Mock Circuits (CVMCs), for safety and efficacy. The first step to design a CVMC is mathematical modeling, and validation of its efficacy, stability, robustness and limitations. In this thesis, a zero-dimensional lumped model of the cardiovascular system, consisting of left and right hearts, and systemic, pulmonary and coronary circulations, was established. A novel time-varying elastance generation method, originating from biomechanical characteristics of the myocardium, was created based on previously published experimental data, and a unique auxotonic length-tension-velocity relationship for the myocardial sarcomere was derived. Tension values were converted into ventricular pressures, and controlled with a binary activation signal to introduce myocardial active state. The resulting time course of state variables, load-dependent and -independent performance indexes were observed to be in accordance with the literature. The system showed stability and robustness against external disturbances and parameter variations under various physiological conditions (normal/disease and rest/exercise). In conclusion, the model constituted a very promising simulation platform to test LVAD performance.

Keywords: Cardiovascular mock circuit, Mathematical modeling, Myocardial mechanics, Time-varying elastance, Feedback control.

ÖZET

ZAMANLA DEĞİŞEN ELASTANS İLE SÜRÜLEN BİR KARDİYOVASKÜLER SİMÜLASYON DEVRESİNİN TASARIMI

Kronik kalp yetmezliğinin tek bilinen kalıcı çözümü kalp naklidir. Donör azlığı nedeniyle sadece küçük bir grup insan tedavi edilebilmektedir. Sol Ventrikül Destek Pompaları (SVDP) kalp nakil listelerinde sıra bekleyenleri yaşatmak için sıklıkla kullanılırlar. SVDP ventrikülün apeks noktasıyla çıkan aort arasına takılırlar ve kalbin yükünü paylaşırlar. SVDP klinik kullanımlarından önce laboratuvar ortamında, çoğunlukla Yapay Kardiyovasküler Devreler (YKVD) ile, güvenlik ve etkinlik testlerine derinlemesine tabi tutulabilirler. YKVD tasarımının ilk adımı matematiksel modelleme ile etkinlik, kararlılık ve sınırlamaların belirlenmesidir. Bu tezde, kardiyovasküler sistemin, sol ve sağ kalp ile sistemik, pulmoner ve koroner dolaşımları içeren, sıfır boyutlu kümelenmiş bir modeli kurulmuştur. Hali hazırda yayımlanmış deneysel veriler kullanılarak ve kalp kasının biyomekanik özelliklerinden faydalanılarak yeni bir zamana bağlı elastans üretim metodu geliştirilmiştir. Bu sayede, myokardiyal sarkomerin özgün bir oksotonik uzunluk-gerilim-hız bağıntısı elde edilmiştir. Aktif durumu dahil etmek için gerilimler basınca çevrilerek lojik bir aktivasyon sinyali ile kontrol edilmiştir. Sonuçta elde edilen durum değişkenlerinin zamana bağlı değerleri, yüke bağımlı ve bağımsız performans parametreleri literatürle uyumlu çıkmıştır. Sistem çeşitli fizyolojik koşullar (normal/hasta ve dinlenme/egzersiz) altında bozucu girdilere ve parametre değişimlerine karşı kararlılık ve gürbüzlük göstermiştir. Netice olarak model, SVDP performansının test edilebileceği bir platform teşkil etmektedir.

Anahtar Sözcükler: Yapay Kardiyovasküler Devre, Matematiksel modelleme, Kalp kası mekaniği, Zamanala değişen elastans, Geri beslemeli kontrol

TABLE OF CONTENTS

LIST OF FIGURES

LIST OF TABLES

LIST OF SYMBOLS

P	Pressure
V	Volume
C	Compliance
E	Elastance
F	Force
A	First Constant of Hill's Two Element Muscle Model
B	Second Constant of Hill's Two Element Muscle Model
l	Length
T	Tension
R	Resistance
Q	Flow
r	Radius
L	Inertance
D_{O2}	Myocardial Oxygen Demand
M	Mass
t	Time
u	Binary Activation Signal
a	Control Signal
x	Dummy Variable
y	Dummy Variable
f	Frequency
K_{c2}	Coronary Capillary Resistance Coefficient
K_{im}	Coronary Capillary Vasculature Compression Coefficient
S_{O2}	Myocardial Oxygen Supply
CAV_{O2}	Coronary Arteriovenous Oxygen Difference
n	Number of Cardiac Cycles
m	Dummy Variable
K_P	Discrete Proportional Controller Coefficient

z	Dummy Variable
w	Wall Thickness
h	Height
ϑ	Velocity
μ	Dynamic Viscosity
ρ	Density
γ	Magnitude
ϵ	Strain
β_T	Isometric Myocardial Inotropic Coefficient
β_ϑ	Isotonic Myocardial Inotropic Coefficient
ξ_P	Passive Myocardial Biomechanical Coefficient
α	Tension-Pressure Conversion Coefficient
ε	Oxygen Deficit (Error)
η	Efficiency
θ	Volume-Varying Tension-Pressure Conversion Coefficient

LIST OF ABBREVIATIONS

CHF	Chronic Heart Failure
WHO	World Health Organization
HTx	Heart Transplantation
LVAD	Left Ventricular Assist Device
CVMC	Cardiovascular Mock Circuit
RA	Right Atrium
RV	Right Ventricle
LA	Left Atrium
LV	Left Ventricle
TV	Tricuspid Valve
PV	Pulmonary Valve
MV	Mitral Valve
AV	Aortic Valve
ECG	Electrocardiogram
IVC	Isovolumic Contraction
IVR	Isovolumic Relaxation
EDV	End Diastolic Volume
ESV	End Systolic Volume
SV	Stroke Volume
HR	Heart Rate
CO	Cardiac Output
PVL	Pressure-Volume Loop
EW	External Work
ESPVR	End-Systolic Pressure-Volume Relationship
SEE	Series Elastic Element
PEE	Parallel Elastic Element
CE	Contractile Element
ImCE	Isometric Contraction Experiment

ItCE	Isotonic Contraction Experiment
AICE	Afterloaded Isotonic Contraction Experiment
AtCE	Auxotonic Contraction Experiment
CBF	Coronary Blood Flow
PFS	Physiological Feedback Systems
PVA	Pressure-Volume Area
PE	Potential Energy
SW	Stroke Work
KVL	Kirchhoff's Voltage Law
KCL	Kirchhoff's Current Law
CBF	Coronary Blood Flow
PL	Preload
AL	Afterload
EF	Ejection Fraction
MAP	Mean Arterial Pressure
PI	Power Index
PV	Pressure-Volume
w.r.t.	with respect to

1. INTRODUCTION

1.1 Motivation

Chronic Heart Failure (CHF) can be caused by congenital or acquired problems in the anatomy and/or physiology of the coronary circulation, ventricular geometry, heart valves etc. [1]. According to World Health Organization (WHO), only in 2015, CHF was responsible of more than 9 million deaths worldwide [2]. Although the only non-palliative treatment for CHF is Heart Transplantation (HTx), only a small group can be treated with HTx due to lack of donors and sub-optimal coordination, while others succumb to the disease. To increase the life expectancy of the people on HTx waiting lists, Left Ventricular Assist Devices (LVADs) present a viable solution [1].

LVADs are miniature hydraulic blood pumps that are surgically implanted between the ventricular apex and ascending aorta, unloading the left ventricle. As for all medical devices, LVADs must be thoroughly tested in-vitro in order to verify their safety and efficacy. Physical Cardiovascular Mock Circuits (CVMCs) are widely used for this type of pre-clinical testing of LVADs.

Physical CVMCs are hydraulic circuits that consist of steady or pulsatile pressure sources in series with compliance chambers and resistance/inertance elements. CVMCs enable the reproduction of cardiovascular hemodynamics with controllable parameters and external loading conditions, making them a reliable platform for testing LVAD performance under various physiologies. The first design step of a physical CVMC is the mathematical modeling and validation of the model in computer environment by assessing the stability, robustness, limitations and range of the system.

1.2 Aims

The dual aims of this thesis are to use the MATLAB/Simulink platform to a) design a mathematical model of the cardiovascular system and b) use this model to simulate cardiovascular hemodynamics under varying normal or pathological physiological conditions.

1.3 Outline

In the first part of this thesis (Background), a detailed description of the anatomy (design), physiology (function) and energetics of the heart, of the heart muscle (myocardium) and of the circulatory system is given. This is followed by a review of previously developed physical and mathematical CVMCs, with special emphasis placed on design methods and control strategies employed therein. Finally, the gap(s) in prior research are briefly discussed, which naturally leads to the enumeration of the general objectives and specific aims of the present research.

In the second part, the methods used to design the mathematical model for the various compartments of the cardiovascular system are described. A novel approach is proposed to generate instantaneous ventricular pressure from the micro level biomechanical properties of the myocardium, as the tension-dependent variations in sarcomere length are converted to ventricular volume variations. The explanation of how physiologic constraints, such as load-dependent and independent mechanical performance and myocardial energy equilibrium, are embedded into the mathematical model concludes the section.

In the last part, the output of the system under various loading conditions is shared. Results are compared to prior art with respect to improvements and limitations. The potential and ease of creating a physical mock circuit based on the developed model is evaluated. To conclude the thesis, planned future work on the current sys-

tem is discussed, particularly in relation to which feedback control mechanisms will be incorporated into the mathematical model, and how the optimality of the chosen criterion functional (e.g. stroke work, cardiac power, mechanical efficiency) will be realized given the choice of the input variable (systolic duration ratio, time-varying LV elastance, rate of change of LV pressure, etc.).

2. BACKGROUND

In the first part of this chapter, the physiology of the human heart and physiologic control mechanisms of the cardiovascular system are discussed, along with the introduction of related terminology. In the second part, various approaches for modeling the anatomy, physiology and control of the cardiovascular system are described.

2.1 Physiology of the Cardiovascular System

2.1.1 Heart

The heart is the engine that sustains life in all complex biological organisms. It may be thought as a pulsatile pump that supplies enough blood, therefore nutrition, to all tissues of the organism and removes waste products from them. It does this by taking in blood at low pressure and delivering it back at high pressure. This produces a pressure gradient through the body, hence resulting in flow. Backflow of blood due to the same pressure gradient is prevented thanks to unidirectional valves within the heart.

2.1.1.1 Physiology of the Heart. In the heart there are four chambers referred as Right Atrium (RA), Right Ventricle (RV), Left Atrium (LA) and Left Ventricle (LV). RA and RV form the start of the pulmonary circulation. Deoxygenated blood from the body returns to the RA from where it is transferred to RV through the Tricuspid Valve (TV). From the RV, blood is pumped through Pulmonary Valve (PV) into lungs for oxygenation. Oxygenated blood is collected in the LA and transferred to the LV through the Mitral Valve (MV). Blood accumulated in the LV is pressurized and then ejected through the Aortic Valve (AV) into the Aorta at relatively high pressure, and travels in the systemic circulation (Figure 2.1) [3].

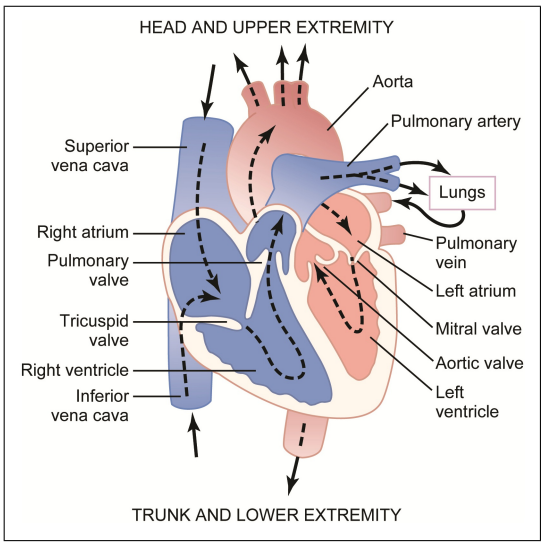

Figure 2.1 Functional structure of the heart [3]

2.1.1.2 Cardiac Cycle. A cardiac cycle can be defined as the sum of events occurring within a single heartbeat. Each cycle begins with the action potential generated by the Sinus Node located in the RA wall (Figure 2.2). This creates the depolarization wave of P in electrocardiogram (ECG) (Figure 2.3). During the P-R interval muscles in both atria contract and push the blood into their respective ventricles. As the depolarization wave propagates towards the A-V Node and Purkinje Fibers in the outer walls of the ventricles, depolarization commences through the Left and Right Bundle Branches located in Interventricular Septum creating a so called QRS complex in ECG. This marks the beginning of ventricular contraction. During the S-T interval, muscles in ventricles contract and push the blood towards their respective arteries. T wave in the ECG shows the repolarization of the ventricles. After the T wave, muscles in ventricles relax and internal pressure drops, preparing the heart for the next cycle. Similar to ventricular relaxation, muscles in atria relax and repolarize. However their repolarization wave is relatively small and occurs during QRS complex. Therefore it becomes masked by QRS complex and cannot be seen in a normal ECG [3].

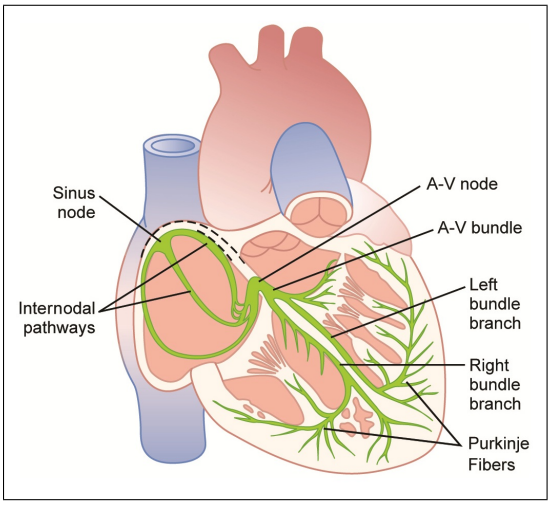

Figure 2.2 Cardiac neural pathways [3]

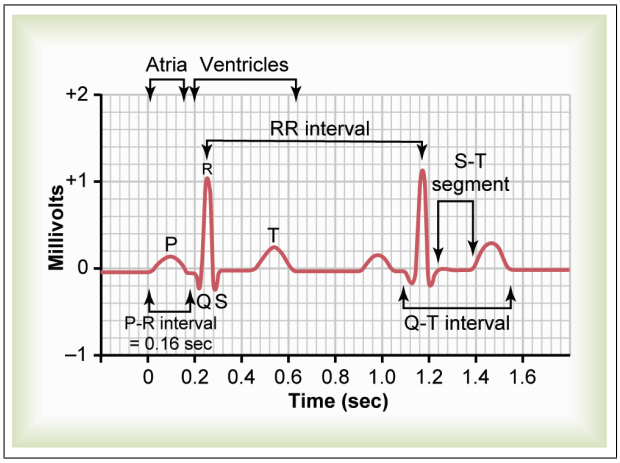

Figure 2.3 Normal human ECG [3]

Even though anatomic structures and physiological working conditions differ between the right and left sides of the heart, in a rough sense both sides do the same job in a synchronized fashion. For simplicity, only events regarding LV in a cardiac cycle will be explained with more detail within the focus of this thesis.

In a cardiac cycle, the LV changes states between contraction and relaxation. These states produce pressure changes in the LV. The interaction of LV pressure (P_{LV}) with LA and Aortic pressures (P_{LA} and P_{Ao}, respectively) splits the cardiac cycle into four parts (Figure 2.4) [3].

The first part can be defined as the Isovolumic Contraction (IVC) starting with the closing of the MV while the AV is not yet open. During IVC, ventricular muscles contract and apply a tension around the chamber. This tension increases P_{LV} at constant volume due to the incompressibility of blood and the uni-directionality of the heart valves, and P_{LV} rises from P_{LA} to P_{Ao} [3].

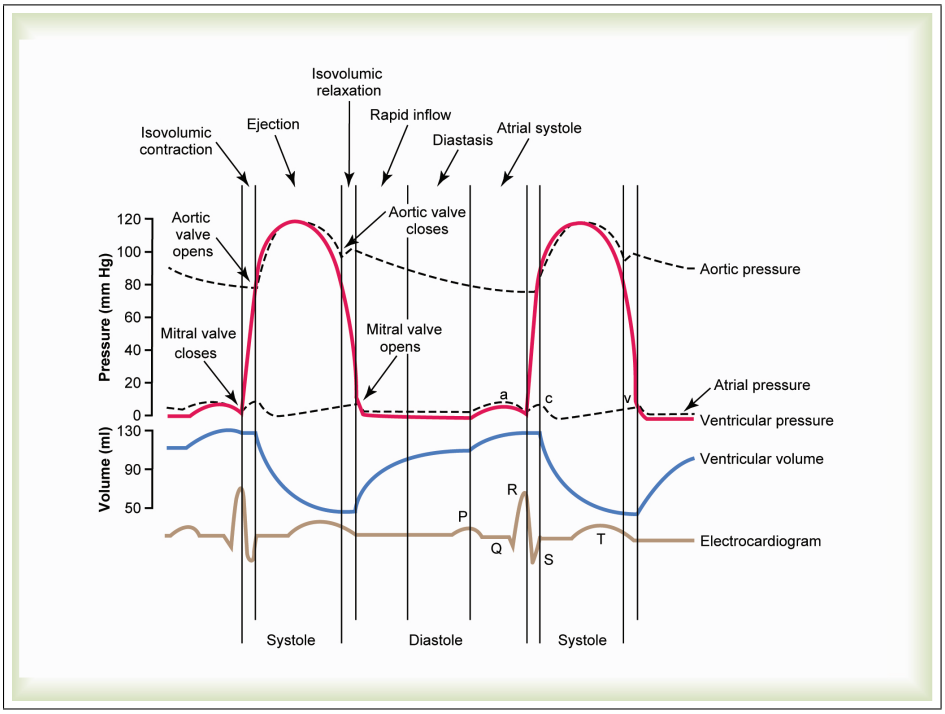

Figure 2.4 Time domain graphs of left ventricular function [3]

When the P_{LV} reaches P_{Ao}, AV opens and blood starts to leave the heart. At this point P_{Ao} is at the minimum of around 80 mmHg in average for a healthy human during rest. With the opening of AV the second part of the cardiac cycle begins, referred to as Ejection. During Ejection, both P_{LV} and P_{Ao} rise reaching a maximum of around 120 mmHg in average for a healthy human during rest, after which point both start to fall [3].

P_{LV} falls more rapidly than P_{Ao} due to the relaxation of ventricular muscles. When the P_{LV} decreases enough below P_{Ao}, AV closes marking the beginning of the third part, Isovolumic Relaxation (IVR). During IVR, ventricular muscles relax and P_{LV} drops at constant volume since the MV has not yet opened [3].

Finally, when P_{LV} becomes equal to P_{LA}, the MV opens. Thence the fourth part, Filling, begins. During Filling, blood from LA fills the LV, therefore preparing it for the next cycle. Filling stops as soon as ventricle starts to contract and the difference between P_{LV} and P_{LA} closes the MV [3].

IVC and Ejection together are referred to as Systole; while IVR and Filling together are referred to as Diastole. In other words, LV is actively pressurizes then ejects blood during Systole; and passively depressurizes then fills with blood during Diastole [3].

The switching points between Systole and Diastole are important due to their impact on the hemodynamics of the cardiovascular system. At the end of Diastole (closure of MV), LV becomes isolated from the rest of the cardiovascular system therefore it cannot increase its volume. This is the maximum volume of LV for a cardiac cycle and is referred to as End Diastolic Volume (EDV). Similarly at the end of Systole (closure of AV), LV becomes isolated from the rest of the cardiovascular system and, therefore, cannot decrease its volume. This is the minimum volume of LV for a cardiac cycle and is referred to as End Systolic Volume (ESV). The difference between the EDV and ESV is the Stroke Volume (SV), which is the blood pumped to the body during a single cardiac cycle (Equation 2.1) [3].

$$SV = EDV - ESV \tag{2.1}$$

One cardiac cycle is called a beat. The total number of times the heart beats in a minute is the Heart Rate (HR). The volume output of the heart per minute is called Cardiac Output (CO) and is given by Equation 2.2 [3].

$$CO = SV \times HR \tag{2.2}$$

2.1.1.3 Frank-Starling Mechanism. Named after the physiologists Otto Frank and Ernest Starling, Frank-Starling Mechanism defines a fundamental relationship between the inflow and outflow of the heart [3].

While filling, cardiac muscle stretches to accommodate incoming blood. The more the incoming blood accumulates in the ventricles the more stretched the muscle fibers are, and the more the heart contracts to eject the extra blood back to the circulation [3].

This relation shows the ability of the heart to adapt its SV to the venous return on a beat-to-beat basis. Thus an equilibrium is established between the inflow and outflow through the ventricles, preventing the ventricles to overfill or overeject during diastole and systole respectively. In Guyton and Hall's words "Within physiological limits, the heart pumps all blood that returns to it by the way of the veins." [3].

When atrial pressure increases, more blood fills the ventricle therefore more blood is ejected from the heart resulting in increased CO, until excessive loading occurs resulting with a decrease in CO (Figure 2.5) [4].

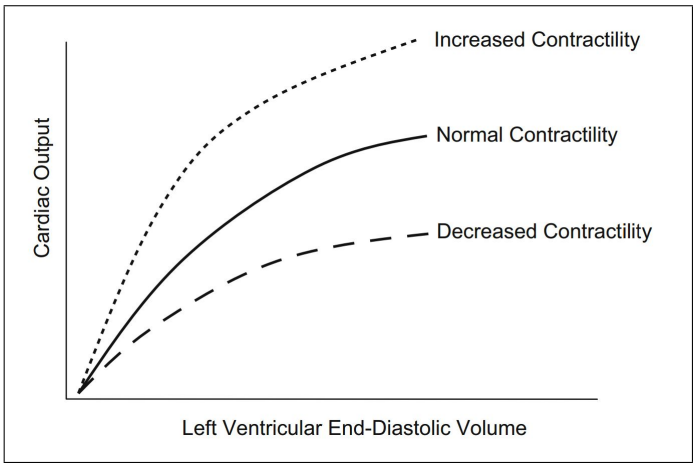

Figure 2.5 Relationship between CO and left ventricular EDV for different contractile states [4]

2.1.1.4 Pressure-Volume Loop. The primary workhorse of the cardiovascular system is the LV and there is much need to understand and evaluate its capabilities in a quantitative and intuitive manner. A graph called Pressure-Volume Loop (PVL) is used for this purpose. The PVL is generated by plotting the instantaneous P_{LV} against the instantaneous Left Ventricular Volume (V_{LV}) (Figure 2.6), i.e. eliminating the variable of time from Figure 2.4. This graph presents the events of the Cardiac Cycle as explained in Section 2.1.1.2 in a more intuitive fashion and enables direct observation of the changes in ventricular elastance and compliance during systole and diastole, respectively (see Section 2.1.1.5) [3].

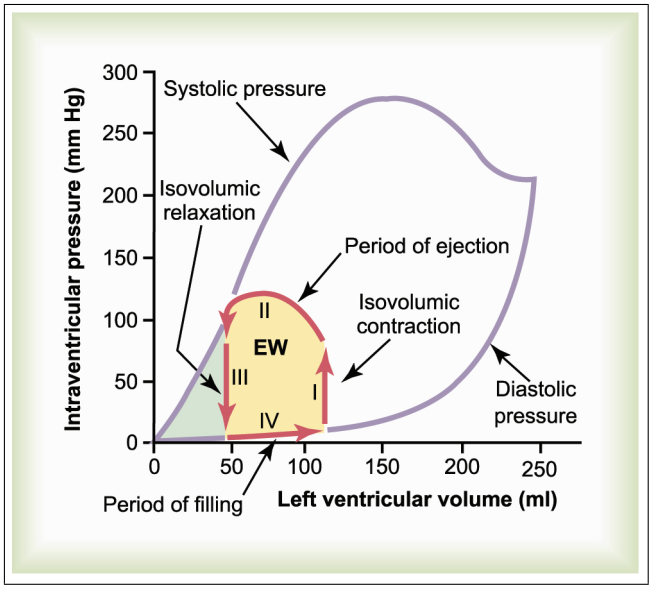

Figure 2.6 Pressure-Volume Loop of normal human LV [3]

In Figure 2.6, the lilac curves denoted by "Diastolic pressure" and "Systolic pressure" represent the physiological limits of the heart. These curves are generated in experiments involving filling the heart with increasing volumes of blood for each loop and measuring the pressure and volume over time both before and during the contraction. Therefore, the PVL (curves in red, marked I, II, III, and IV) is constrained by the Diastolic and Systolic pressure curves [3].

As mentioned before, PVL gives a more intuitive understanding of LV hemodynamics. This is achieved via better visualization of instantaneous pressure and volume relative to each other. PVL also helps clarify different parts of the cardiac cycle as described in Section 2.1.1.2 [3].

In Figure 2.6, IVC, during which P_{LV} increases at constant V_{LV}, may be visualized with the red curve denoted with the Roman numeral "I". Ejection, where P_{LV} increases first reaching a maximum then dropping while V_{LV} decreases continuously, may be visualized with red curve denoted with the Roman numeral "II". IVR, during which P_{LV} decreases at constant P_{LV} may be visualized with the red curve denoted with the Roman numeral "III". Finally, the fourth part of the cardiac cycle, Filling, during which both P_{LV} and V_{LV} increase as the ventricle fills with blood may be visualized with the red curve denoted by the Roman numeral "IV" [3].

In fluid dynamics, External Work (EW) done by a system is defined as the product of pressure at which the work is being done and the volume that is being transferred. If the PVL is divided into infinitesimal slices of volume, ΔV_{LV}, and each slice is multiplied with its respective pressure, the sum of all infinitesimal products will represent the work done during that part of the graph [3].

During the IVC and IVR, which occur at constant volume ($\Delta V_{LV} = 0$), no EW is done. During Ejection, both P_{LV} and V_{LV} change resulting in positive EW done on the circulation system. This can be seen in the PVL depicted in Figure 2.6 as the area under the curve II. By contrast, during Filling, both P_{LV} and V_{LV} increase passively due to work done by the circulation system on the LV hence, EW is negative. This is the area under the curve IV in Figure 2.6. As a result net EW done by the LV becomes the area between the curve II and IV. This area is shown painted yellow and denoted by letters "EW" in Figure 2.6 (Equation 2.3) [3].

$$EW = \int P_{II} dV - \int P_{IV} dV \tag{2.3}$$

PVL also allows the monitoring of external loading conditions, preload and afterload, which directly affect the working dynamics of the heart. Preload is defined as the volume which accumulates in the LV during filling. This volume stretches the fiber in cardiac muscle, performing negative work and loading the heart before the muscle is electrically activated. In accordance with the Frank-Starling Mechanism, preloading the heart to a particular EDV determines the SV [3].

Afterload is defined as the pressure distal to the AV, i.e. the pressure the LV has to overcome in order to eject blood into the circulatory system. As the LV pumps blood into the Aorta, it increases P_{Ao}. Therefore the LV increases its own afterload during the ejection phase, and has to overcome more and more pressure to eject more blood [3].

In summary, preload is the pressure of the circulation system while filling the LV with volume to prepare the heart for another cycle of ejection and afterload is the pressure crated by the LV in the circulation system while pumping blood back into it [3].

2.1.1.5 Compliance and Elastance. Compliance and elastance define the relationship between pressure and volume in a hydraulic system.

Compliance (C) is the amount of change in the volume (ΔV) of a deformable vessel as its internal pressure changes (ΔP). (Equation 2.4) [3].

$$C = \frac{\Delta V}{\Delta P} \tag{2.4}$$

Elastance (E) is the inverse of compliance, i.e. the amount of change in the internal pressure (ΔP) of a deformable vessel as its volume changes (ΔV) (Equation 2.5) [5].

$$E = \frac{\Delta P}{\Delta V} \tag{2.5}$$

$$E = \frac{1}{C} \tag{2.6}$$

In cardiovascular hemodynamics, compliance is used to express the elastic properties of the compartments such as the ventricles, atria, aorta, arteries, veins etc. as they passively stretch during filling. Elastance, on the other hand, can be both active and passive. In the case of the ventricles, elastance is used to describe the intrinsic power of the muscular walls as they actively reduce the internal volume and pressurize blood for ejection. But in the case of the aorta and the pulmonary artery, elastance is the passive elastic recoil of the arterial wall during diastole (when outflow from respective ventricles has ceased), causing blood to be propelled in the distal circulation.

On the PVL, Elastance corresponds to the slope of a line drawn from theoretical zero-pressure volume (V_0) to any point on lines enclosing the loop (Figure 2.7).

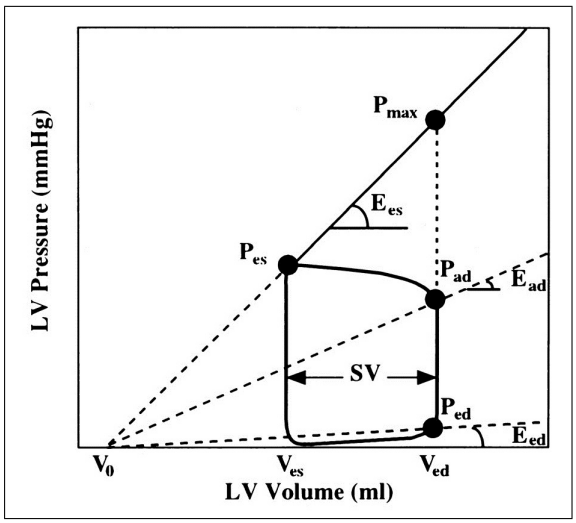

Figure 2.7 Elastance lines on PVL [6]

LV elastance reaches its maximum level (E_{max} or E_{es}) at the end of systole, when the AV closes. In Figure 2.8, the end systolic point for a normal heart is shown to follow a straight line with constant slope (E_{max}) as preload and afterload are changed. This line is called the End-Systolic Pressure-Volume Relationship (ESPVR). Also in the same graph, the slope, E_{max}, of ESPVR is seen to increase as the inotropic state of the

heart is increased by epinephrine injection. The concept of E_{max} as an intrinsic load-independent index of LV function (contractility), sensitive only to myocardial inotropic state, was first used by Suga et. al in 1973; and has been used extensively in modeling ventricular function ever since.

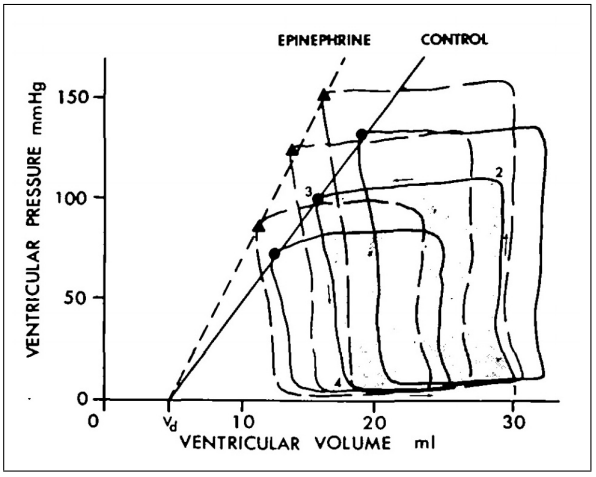

Figure 2.8 Independence of E_{max} to preload and afterload, and dependence to myocardial inotropic state [5]

When elastance of each point on PVL plotted with respect to time and normalized respectively Figure 2.9 is acquired.

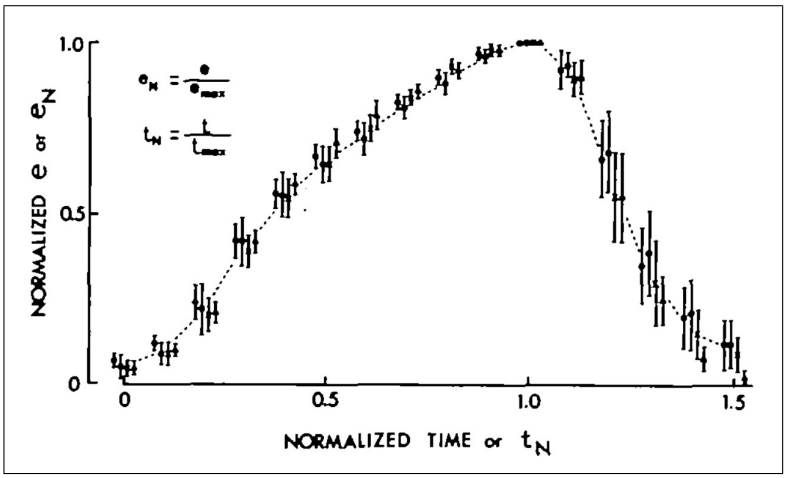

Figure 2.9 Normalized elastance w.r.t. E_{max} plotted on normalized time w.r.t. time to E_{max} [5]

2.1.2 Cardiac Muscle

Ventricular walls are mostly built up by cardiac muscle (myocardium), which has three main types: These are atrio-ventricular muscle, specialized muscle and conductive muscle. Contraction characteristics of atrio-ventricular muscle fibers show close similarities to skeletal muscle except in the cardiac muscle contraction lasts longer. Specialized and conductive muscle fibers do not influence contractile power noticeably as their purpose of action is restricted to the conduction of electrical activation [3].

Anatomy of cardiac muscle is defined by Guyton A.C. and Hall J.E. as "fibers arranged in a latticework, with the fibers dividing, recombining, and then spreading again" (Figure 2.10). Cardiac muscle fibers have striated muscle patterns similar to skeletal muscle. Due to the fact that myocardium has actin and myosin myofibrils identical to skeletal muscle, they contract in the same way at the filamental level [3].

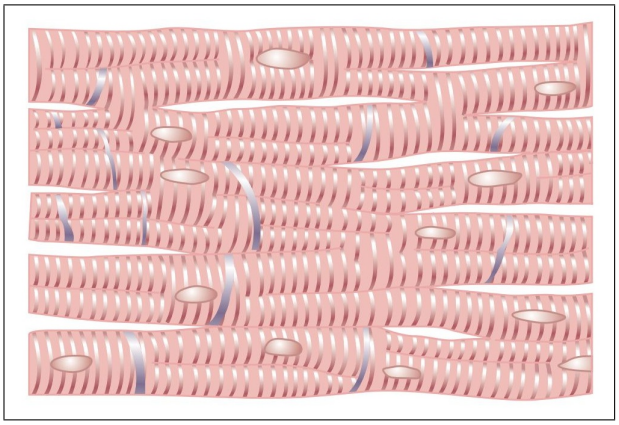

Figure 2.10 Syncytial pattern of myocardial fibers [3]

This inter-connected (syncytial) pattern of cardiac muscle as seen in Figure 2.10 allows connections between individual cells marked in grey called gap junctions. Here ions can easily be transferred from one cell to another therefore resulting with fast action potential transfer through the entire myocardium. Atria and ventricles have separate syncytia that allow independent contraction [3].

2.1.2.1 Sliding Filament Theory. A muscle consists of muscle fascicles that is a bundle of muscle fibers (muscle cells) that have several hundred to several thousand myofibrils in it. Each myofibril is, in turn, built up by several hundred to several thousand sarcomeres that are arranged in series and parallel fashion (Figure 2.11) [3].

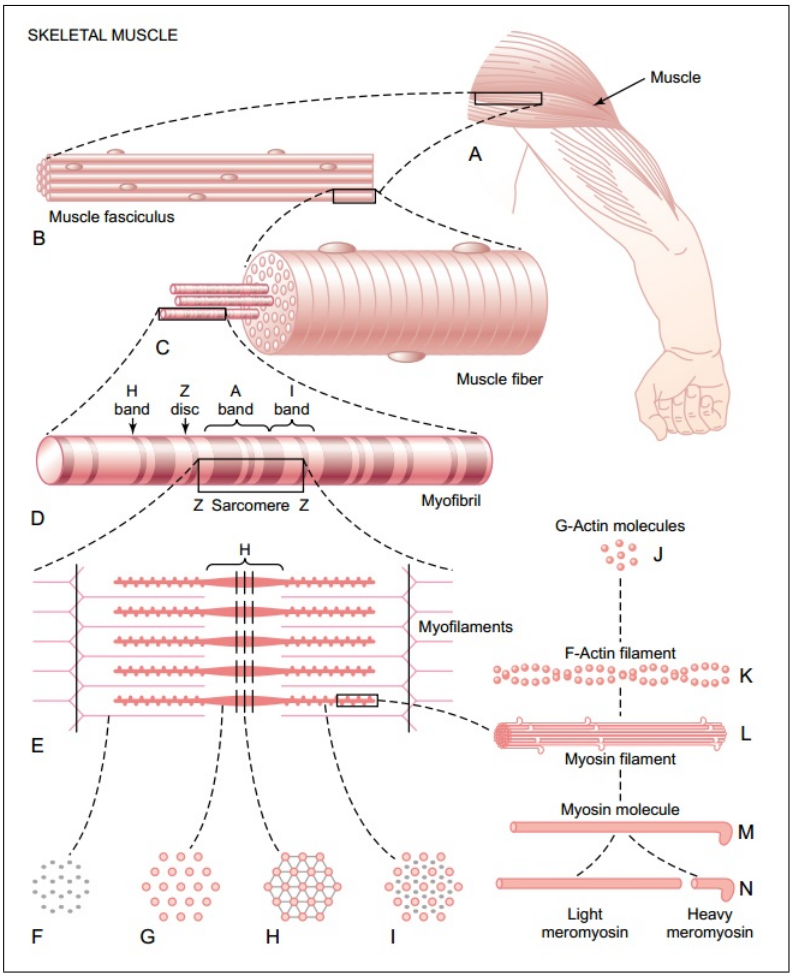

Figure 2.11 Structural representation of skeletal muscle [3]

Sarcomeres, the smallest muscle elements, are the force generation structures in muscles. The fundamental building blocks of sarcomeres are actin and myosin molecules. The sliding filament theory of skeletal muscle has been proposed in 1954 simultaneously but independently by Huxley A.F. & Niedergerke R. and by Huxley H.E. & Hanson J. In their landmark studies, both group of investigators present similar conclusions for the mechanism of force generation in muscle due to the interaction between actin and myosin molecules [7, 8].

Contraction begins with the arrival of electrical stimuli from motor neurons. These cause the release of Ca^{+2} ions from the sarcoplasmic reticulum. Ca^{+2} ions bond to the troponin molecules on the actin filament, opening up the myosin bonding sites. Myosin heads then bond to specific receptor sites on the actin filaments forming cross-bridges. Bonding creates a conformational change in the myosin heads, which makes them pull themselves (the power stroke) and slide over the actin, generating force and movement (Figure 2.12). Then the cross-bridge bonds between actin and myosin get separated with ATP therefore preparing the myosin heads for new bond formation [3].

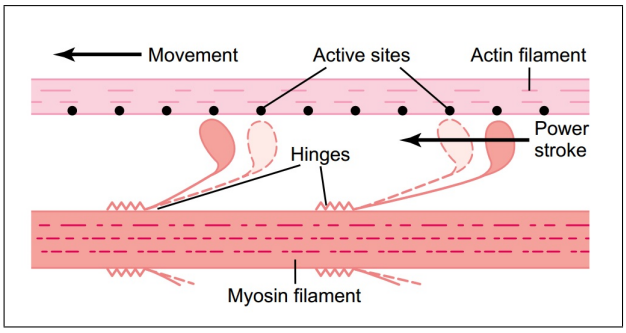

Figure 2.12 Mechanism of force and motion generation in sarcomere [3]

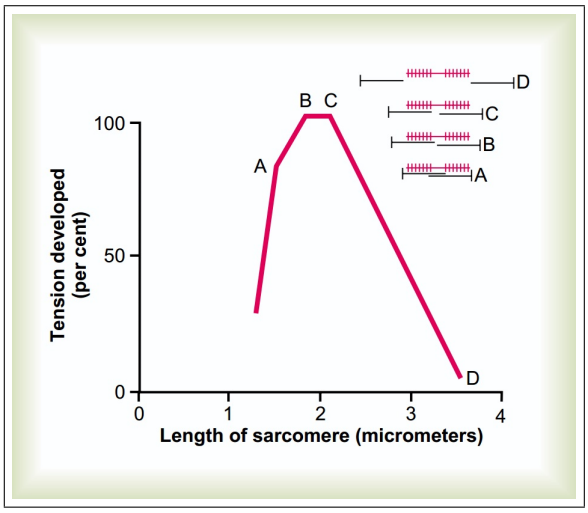

Figure 2.13 Length-tension relationship of sarcomere [3]

To generate enough force in a sarcomere, enough myosin heads must come in close proximity of actin receptor sites, creating overlapping segments with each other. If the length of the sarcomere is too long (i.e. if the sarcomere is over-stretched) filaments

are separated from each other so as there is no overlap and myosin heads cannot be able to find bonding sites. Therefore force generation does not occur. In contrast, if the sarcomere is too short myosin filaments get squished and actin filaments on the opposing sides entangle with each other. In this case myosin heads and bonding sites get disoriented, therefore no or small number of bonds can be formed. This results with less or no force generation. In between these extremes of too short or too long sarcomere lengths, first the generated force increases, which then reaches a plateau where overlap is maximum and finally drops down to zero (Figure 2.13) [3].

2.1.2.2 Models of Muscle. To explain the proposed models of cardiac muscle, the structure (anatomy) and the function (physiology) of the skeletal muscle sarcomeres have to be understood. As explained in the previous sections cardiac and skeletal muscles are similar both at the molecular level and in their working principles. However at larger scales their passive and contractile properties differ from each other. In this section, models that have been developed for skeletal muscles are given first. Their expanded versions for cardiac muscles are discussed next.

To acquire the phenomenological aspects of the contracting muscle A.V. Hill proposed a model which consists of a contractile element and an elastic spring connected in series (Figure 2.14). This model is known as Hill's two element model. In this model equations can be written using the force-velocity relation for the contractile element and the force-distance relation for the elastic element. Force velocity relation of contractile element as defined by the Hill A.V. is given in Equation 2.7 [9].

$$(F + A)\vartheta = B(F_0 - F) \tag{2.7}$$

where F and F_0 are instantaneous and maximal isometric forces, respectively, ϑ is the instantaneous velocity, and A and B are constants.

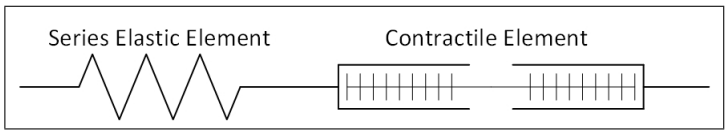

Figure 2.14 Hill's two element muscle model

Although Hill's two element model is quite good at approximating the contractile phenomena of skeletal muscle, it was poor in terms of explaining myocardial contractions, the reason being the difference at the beginning of the passive tension region. In skeletal muscle passive tension starts to rise after the maximum isometric active tension point is reached whereas in the myocardium passive tension starts to build up while the active tension is still ascending (for increasing lengths). This creates an important difference while modeling the myocardium. Therefore within physiological limits even though the two element model is well suited to model the skeletal muscle, it cannot accurately model the myocardium. To overcome this issue and to model myocardial contractile phenomena, a parallel elastic element was added to account for the early rise of the passive force. Thus three element models that consist of a serial elastic element (SEE), a parallel elastic element (PEE) and a contractile element (CE) in two alternative configurations, Voigt (Figure 2.15) and Maxwell (Figure 2.16) models, were proposed. Thus, with the addition of the parallel elastic element it became possible to model the passive tension of the myocardium alongside the active tension [10, 11].

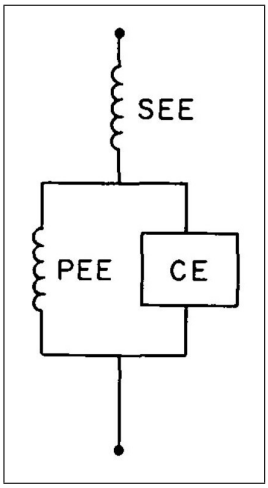

Figure 2.15 Voigt muscle model [11]

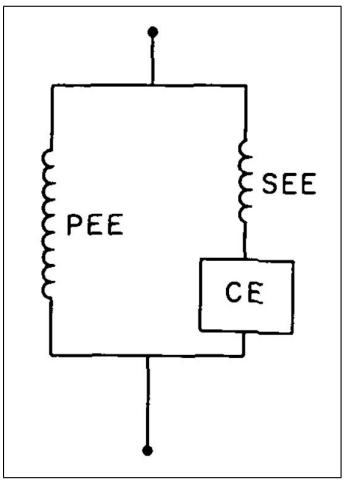

Figure 2.16 Maxwell muscle model [11]

2.1.2.3 Muscle Experiments. To understand the underlying mechanism of muscular contraction, physiologists isolate muscle fibers to conduct four major categories of experimental conditions. These are isometric contraction, isotonic contraction, afterloaded isotonic contraction, auxotonic contraction, quick stretch and quick release experiments. These experiments were first conducted on skeletal muscles of frogs, rats, rabbits etc. and later applied to cardiac muscle (papillary muscle for ease of isolation).

1. Isometric Contraction Experiment

   Isometric contraction experiment (ImCE) as the name suggest is performed on muscle strips, which are clamped on both ends so that the muscle is allowed to develop force without being able to change its length. A typical ImCE setup consists of a muscle fiber, a force transducer and a stimulator (Figure 2.17). The muscle is attached to the mechanical ground on one end and to the force transducer, also connected to the mechanical ground, on the other end. The mechanical ground can be moved on a linear track and can be fixed at the desired position, enabling the researcher to set the initial muscle length (i.e. initial stretch, which corresponds to the preload) before electrical stimulation.

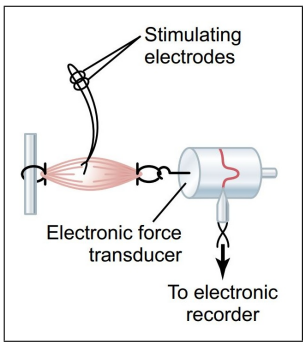

Figure 2.17 Isometric contraction experiment setup [3]

Experimental procedure is as follows: First, muscle is set to a certain length and its passive force is measured. After that, muscle is stimulated to contract isometrically and maximum total force it has generated at this preload is measured. The active force generated by the muscle is calculated simply by subtracting the total force from the passive force. This process is repeated for different initial muscle lengths (i.e. preloads) and an isometric length-force graph is plotted (Figure 2.18).

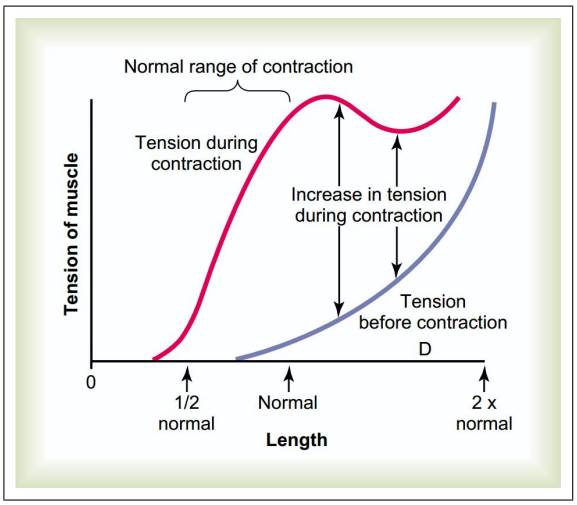

Figure 2.18 Isometric length-tension relationship of muscle [3]

2. Isotonic Contraction Experiment

Isotonic contraction experiment (ItCE) is conducted with the load on the contracting muscle being kept constant while the muscle is being allowed to shorten. A generic ItCE setup consists of an isolated muscle fiber, attached to the me-

chanical ground on one end and to the business end of a lever system on the other end. The fulcrum point of the lever is on the mechanical ground. Weights, a displacement transducer and a stimulator are also part of the setup (Figure 2.19). Different weights can be attached to the other end of the lever to apply a constant force on the muscle after activation.

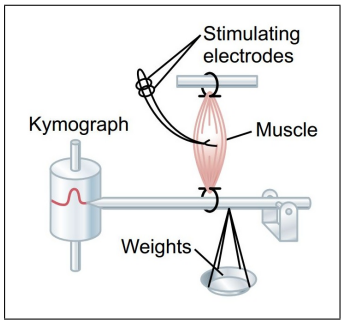

Figure 2.19 Isotonic contraction experiment setup [3]

Experimental procedure is as follows: First, a known weight is attached to the lever that touches the mechanical ground. After that, muscle is stimulated and displacement on the lever is measured. With simple lever equations attached weight and lever displacement, that is measured, is converted to the force and displacement of the muscle. When displacement is plotted against force an isotonic force-length relationship graph is acquired (Figure 2.20).

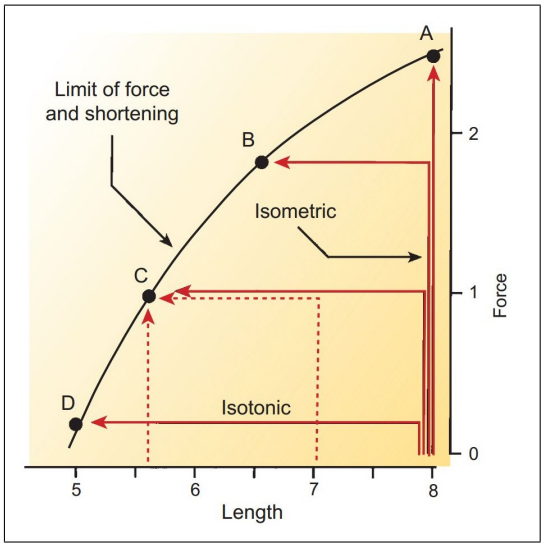

Figure 2.20 Isotonic length-tension relationship of muscle [12]

3. Afterloaded Isotonic Contraction Experiment

Afterloaded Isotonic Contraction Experiment (AICE) are isotonic experiments which are done with the addition of an afterload on a preloaded muscle; therefore resulting with an augmented response from the muscle. AICE has the same setup as ItCE with differences in its procedure.

Experimental procedure is as follows: First, a known preload weight is attached to the lever that touches the mechanical ground and an additional afterload is attached to the preload. After that, muscle is stimulated and the muscle is forced to lift both the preload and afterload together. The displacement on the lever is measured, then both the force and displacement on the lever are converted to the ones of the muscle. Velocity of the muscle is estimated from the time derivative (slope) of the displacement. The experiment is repeated for different preloads and afterloads, and the maximum shortening velocities are recorded. Finally, force and velocity data are plotted against each other giving the force-velocity relation graph (Figure 2.21)

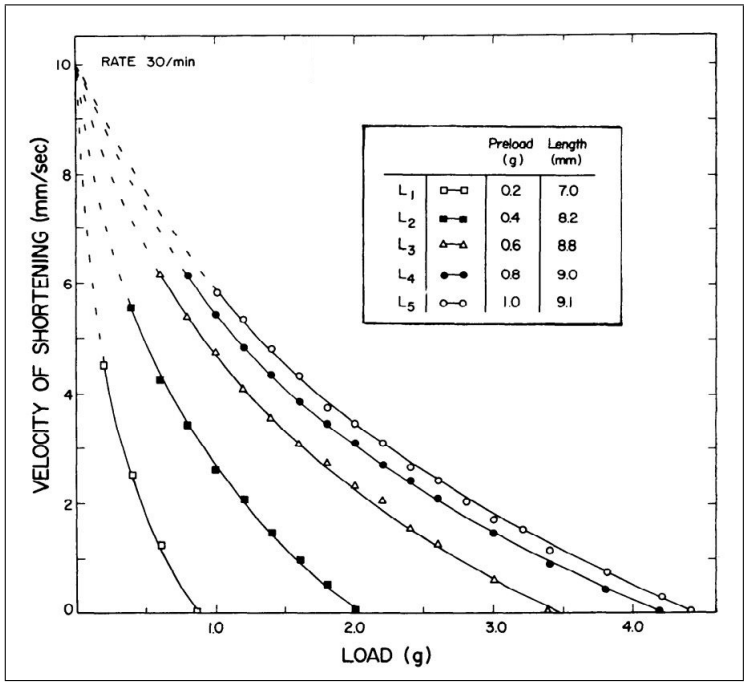

Figure 2.21 Afterloaded isometric tension-velocity relationship of muscle [13]

Notice that, in Figure 2.21, the abscissa intercept of each curve (max total force-preload plus afterload- for which muscle velocity is zero) is a point located on the isometric force curve.

4. Auxotonic Contraction Experiment

   Auxotonic Contraction Experiment (AtCE) is similar to AICE, where the muscle is loaded with a preload and contracted. After the contraction, afterloads are added incrementally such that afterload is increased while the muscle is shortening. Thus AtCE is able to mimic the cardiac function as the heart increases its afterload during ejection.

   Experimental procedure is as follows: First, a known preload weight is attached to the lever that touches the mechanical ground and additional afterloads are attached first to the preload and each other, such a way that afterload on the muscle would increase for each incremental shortening muscle experience. After that, muscle is stimulated and forced to lift the preload and afterloads together. The displacement on the lever is measured, then both the force and displacement on the lever are converted to the ones of the muscle. Velocity of the muscle is estimated from the time derivative (slope) of the displacement. The experiment is repeated for different preloads and the shortening velocities and loads lifted are recorded. Finally, force and velocity data are plotted against each other giving the auxotonic force-velocity relation.

5. Quick Release and Quick Stretch Experiments

   Quick release and quick stretch experiments are similar experiments that are done to determine the dynamic characteristics of elements in muscle models (see Section 2.1.2.2).

   Setup for quick release experiment consists of a lever, a muscle, a catch mechanism, weights, a stimulator, a force transducer and a displacement transducer. Muscle is attached onto the one side of lever and the catch mechanism onto the other side of the lever. Other end of the muscle is connected to the mechanical ground. Weights are attached to the same side as the catch mechanism (Figure 2.22).

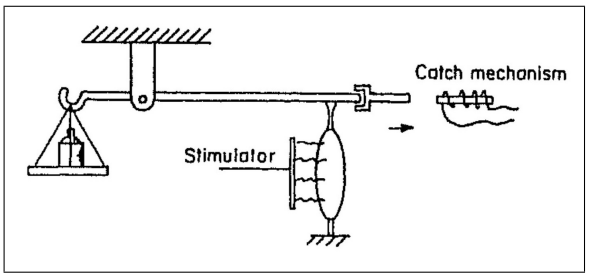

Figure 2.22 Quick release experiment setup [14]

First, the muscle is stimulated. As the catch mechanism is holding the lever, muscle does an isometric contraction. When the catch mechanism is released, weights make sure that the force on the muscle is constant. As soon as the catch mechanism is released the muscle shortens immediately then it continues to shorten slowly in a first order system fashion. Displacement and forces on the muscle are recorded with their respective transducers (Figure 2.23).

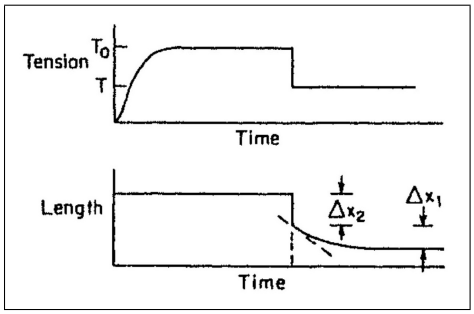

Figure 2.23 Quick release experiment graphs of muscle; top: time-tension graph and bottom: time-length graph [14]

Quick stretch experiment serves the same purpose with small changes to the experimental approach. In quick release extensional displacement is imposed on the muscle from isometric contraction. As soon as the muscle is stretched, force on the muscle makes a spike then drops down to a higher steady-state in first order system fashion. Displacement and forces on the muscle are recorded with their respective transducers (Figure 2.24).

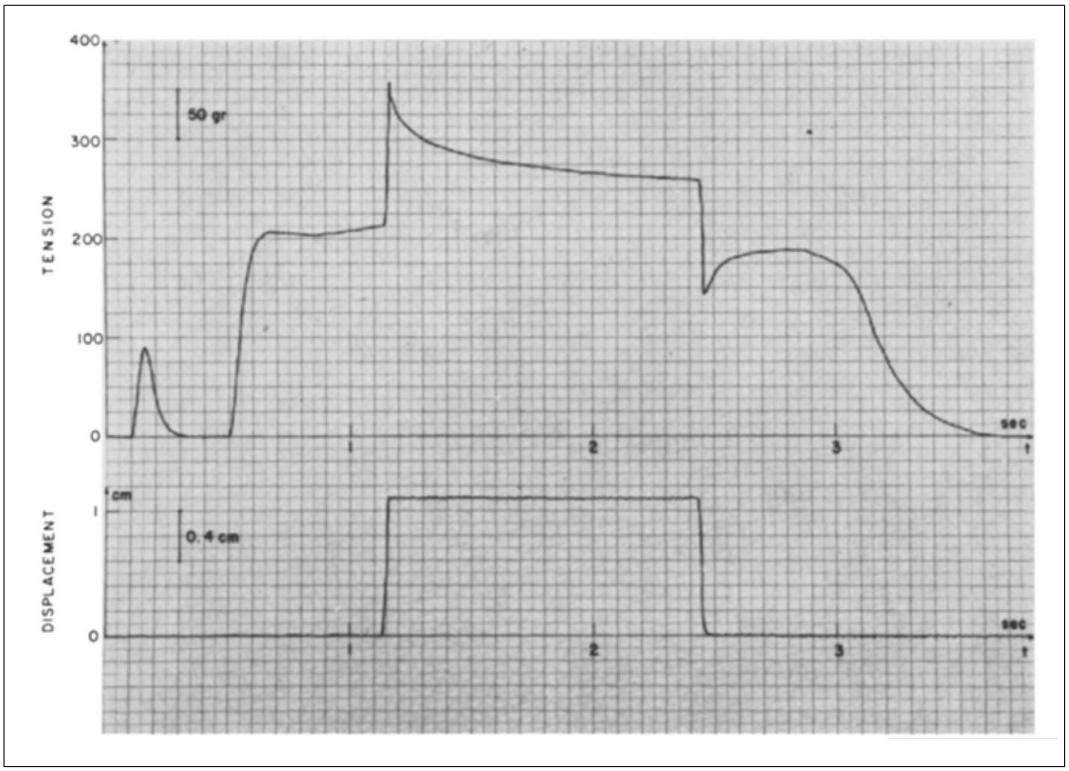

Figure 2.24 Quick stretch experiment graphs of muscle; top: time-tension graph and bottom: time-length graph [15]

2.1.2.4 Length-Tension Relationship in Cardiac Muscle. Length-tension relationship of a muscle indicates the maximum tension generated in the isometric state as the muscle (i.e. sarcomere) length changes due to the preload. In isometric state a muscle can produce a tension without any activation, due to the stiffness of its series & parallel elastic elements. This force is called the passive force. On the other hand when activated, the muscle produces a total tension which is the sum of the passive tension caused by elastic properties and the active tension produced by the sarcomeres (Figure 2.25).

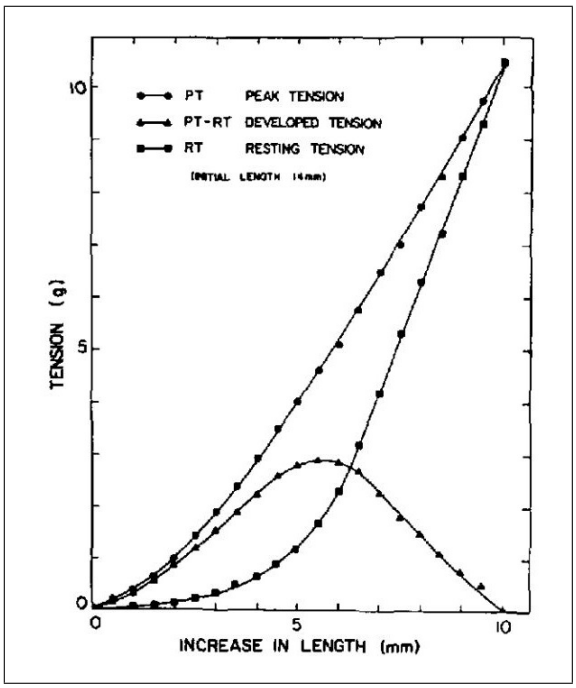

Figure 2.25 Length-tension relationship of a canine papillary muscle [16]

Another important aspect about tension generation is its time dependency. Due to the elastic properties of the tissue within the muscle and the shortening of sarcomeres, generated tension cannot peak instantly. Hence it rises with a slope and reaches its maximum over a time period (Figure 2.26).

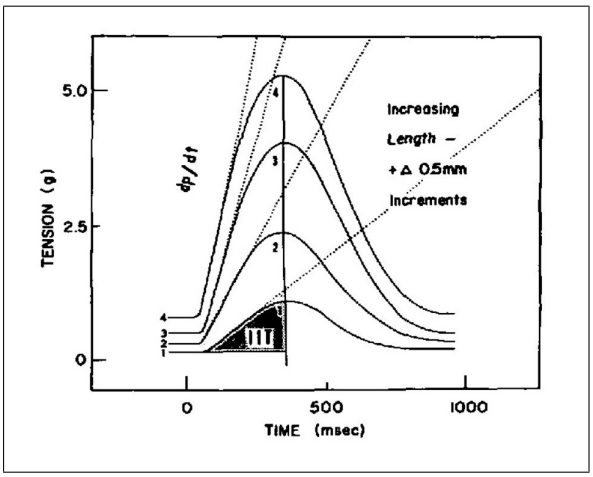

Figure 2.26 Tension generation of a canine papillary muscle over time [16]

Siegel et al. (1963) studied the isometric sarcomere length-tension relationship on canine papillary muscle and isovolumetric cardiac volume-pressure relationship on canine hearts. Additionally they reported their findings on the time evolution of passive and active myocardial tension. Their results showed a rising trend of active isometric tension as the length increases while passive tension increased relatively slowly until the stretch reached 20% of the initial length, after which point the slope became significantly higher. At higher stretches, total tension continued to rise due to the increase in passive tension, even though active tension reached a plateau and stated to decline (Figure 2.25). Amount of initial stretch had no effect on peak tension time (Figure 2.26). Furthermore, administration of positive inotropic agents (norepinephrine and calcium) increased active tension while passive tension was unaffected. The results of their isovolumic experiments on whole myocardium were in parallel with these findings with sarcomeres [16].

Sonnenblick et al. (1964) researched the relation between length-tension relationship of sarcomere and the Frank-Starling Law of the heart on isolated cat papillary muscles. They stated that within physiologic limits, myocardial active tension is directly related to cardiomyocyte length, therefore to the initial stretch of the sarcomere and that, therefore, the Frank-Starling Law of the heart can be represented in terms of the sarcomere's isometric length-tension relationship. They proposed a limiting range for the myocardial sarcomere between 1.5 μm, corresponding to zero active tension at end-systole, and 2.2 μm, corresponding to maximum tension at end-diastole. They stated that the heart cannot exceed or even reach these limits physiologically since, under isotonic conditions, it is the passive tension (i.e. preload) that defines the initial length and the afterload that limits the final length. Therefore they suggested a nominal working range for the sarcomere between 1.7 μm and 2.1 μm. In summary they stated that the Frank-Starling Law of the heart relates the SV to the EDV, and the underlying mechanism is dependent on the length-tension relationship of the sarcomere [17].

Spotnitz et al. (1966) studied myocardial ultrastructure in intact canine and feline hearts. Their main objective was to investigate sarcomere length as it relates to LV filling pressure and volume. They reported that average sarcomere length, both in canine and feline hearts, changes from 1.9 to 2.25 μm at 0 to 12 mmHg filling pressures, respectively; but that after 2.25 μm, sarcomere length increase at a slower rate with increasing pressure. They also report their findings on the relationship between LV volume and myocardial sarcomere length (Figure 2.27). When normalized to filling volume at 10 mmHg the curve presents an exponential rise similar to the passive tension curve and may be used the find the relation between sarcomere length and LV volume. As relates to active tension, they report that zero active tension occurs at 1.5 μm sarcomere length while maximum active tension is reached around 2.18-2.24 μm. Based on this information and the filling pressure limits of the heart, Spotnitz et al. concluded that "normal left ventricle functions only along the ascending portion of the length tension curve" [18].

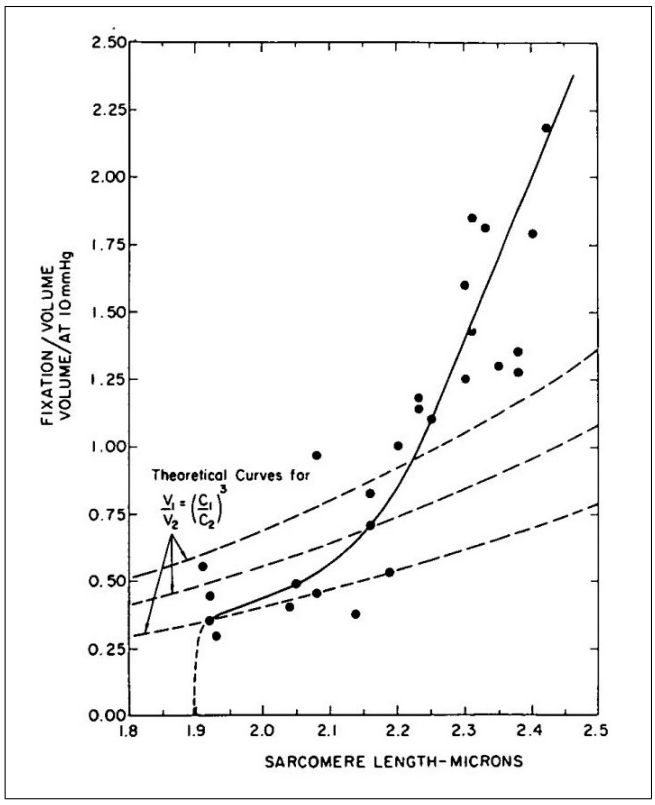

Figure 2.27 Relationship between myocardial sarcomere length and normalized ventricular fixation volume w.r.t. the volume at 10 mmHg [18]

Page (1974), gives a broad review of the myocardial sarcomere length measurements and discusses the length where the active tension is maximum. She states that due to preparation processes there were shrinkages on the specimens. Therefore maximum length measured (l_{max}) on those specimens had an error about 10-12%, when corrected for shrinkage l_{max} became in average 2.3-2.35 μm [19].

Winegrad (1974) studied passive tension and length relationship of sarcomeres on frog atrial trabeculae to show that zero passive tension occurs at a sarcomere length of 1.88 μm and that, after 2.3 μm, passive tension abruptly rises with irreversible structural damage occurring beyond the length of 2.7 μm [20].

Julian et al. (1975) researched the active and passive tension relationship with respect to sarcomere length on rat papillary muscles. They reported that the maximum active tension happened at 2.3 μm (l_{max}), with passive tension corresponding to l_{max} being measured as 1.3 g/mm^2. They also report that, beyond l_{max} active tension reduces slightly while passive tension increases abruptly and that reducing the length to 0.9 l_{max} halves the active tension (Figure 2.28) [21].

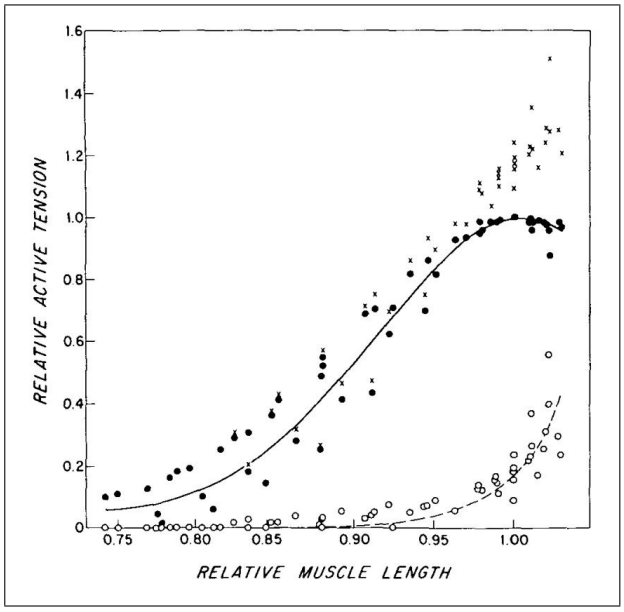

Figure 2.28 Active (full circles) and passive (empty circles) length-tension relationship of myocardium normalized w.r.t. l_{max} and maximum tension at l_{max} [21]

2.1.2.5 Tension-Velocity Relationship in Cardiac Muscle. The tension-velocity relationship of the muscle gives information about the contraction of the muscle under afterloaded conditions. Contraction velocities are measured in isotonic experiments as the afterload is successively increased at a given preload (Figure 2.29) and as the power strokes generated by the sarcomeres moves loads that remain below the maximum tension muscle can create at the specific preload.

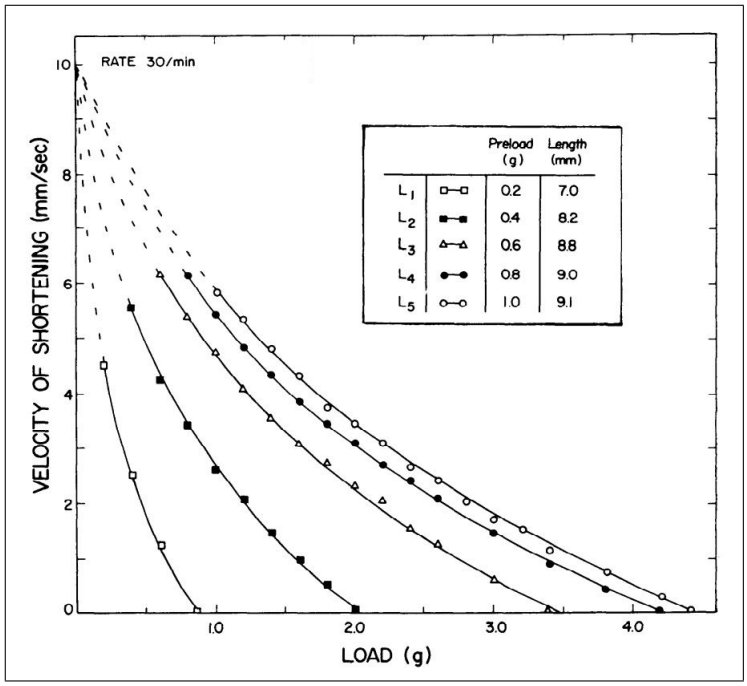

Figure 2.29 Tension-velocity relationship of a cat papillary muscle [13]

The generated tension which contracts the muscle and lifts the load is time dependent due to the elastic properties of the tissue within the muscle which dampen the shortening velocity of the sarcomeres. The tension rises exponentially (as in a first order spring-damper system) until it equals the load and then stays constant at this level. The length of the muscle, on the other hand, remains constant until generated tension equalizes with the load and then begins to shorten (Figure 2.30).

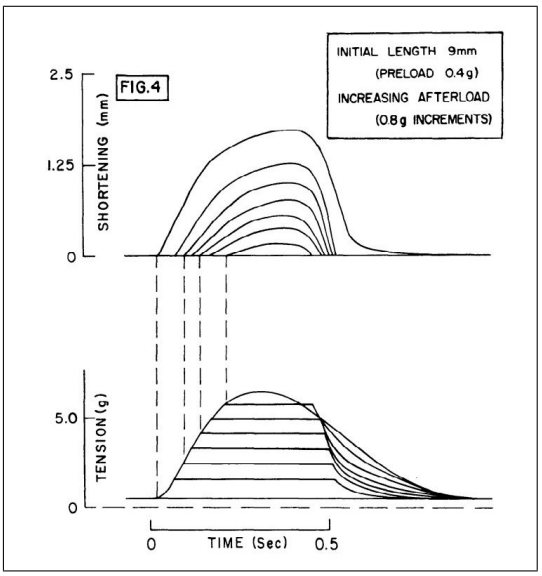

Figure 2.30 Time domain graphics of shortening length (top) and tension (bottom) of an auxotonically loaded cat papillary muscle [13]

Sonnenblick (1962) also studied myocardial tension-velocity relationship on cat papillary muscles. Under isotonic conditions and for constant preloads, he decreased the afterload incrementally and observed that shortening velocity increased and reached a maximum when afterload was zero. He thus generated a family of curves for each constant preload. Since the preload on the muscle can never be reduced to zero (considering the muscle's own weight), he was not able to determine the velocity axis intercept of the curves, where total force (preload plus afterload) would be zero. However, he hypothesized that all curves, when extrapolated to zero load, would meet a theoretical point, which he called ϑ_{max}. On the other hand, it was possible to determine the maximum afterload for each preload (hence the total load, or tension,), at which the velocity of contraction is zero (in other words, the muscle would not be able to generate enough tension to lift the load). Obviously, this T_{max} corresponded to the isometric maximum tension for each preload. Regarding the effects of preload on the tension-velocity relationship, he concluded that increasing the preload and/or the afterload increases the T_{max} while remained unchanged (Figure 2.29) and that, therefore, ϑ_{max} may be considered as a characteristic performance indicator independent of external loading conditions, i.e. as an intrinsic measure of myocardial contractility [13].

In order to support his hypothesis, Sonnenblick first calculated two load-dependent parameters, i.e. myocardial work and power at various preload and afterloads. He observed that both quantities increased with increasing external loads until a maximum around 0.4 T_{max} is reached, beyond which they both decreased continuously and reached zero as the loading condition on the muscle forces it to act isometrically (Figure 2.31). But when he measured the effects of chronotropic (altering the frequency of contraction) and inotropic (altering intracellular calcium ion or norepinephrine concentrations) interventions at constant external loading conditions, he observed that ϑ_{max} was significantly affected, while T_{max} increased initially only to plateau after a certain point (see Fig. 32) [13]. Sonnenblick's assumption that ϑ_{max} is a measure of myocardial contractility would later be criticized by Pollack (1970).

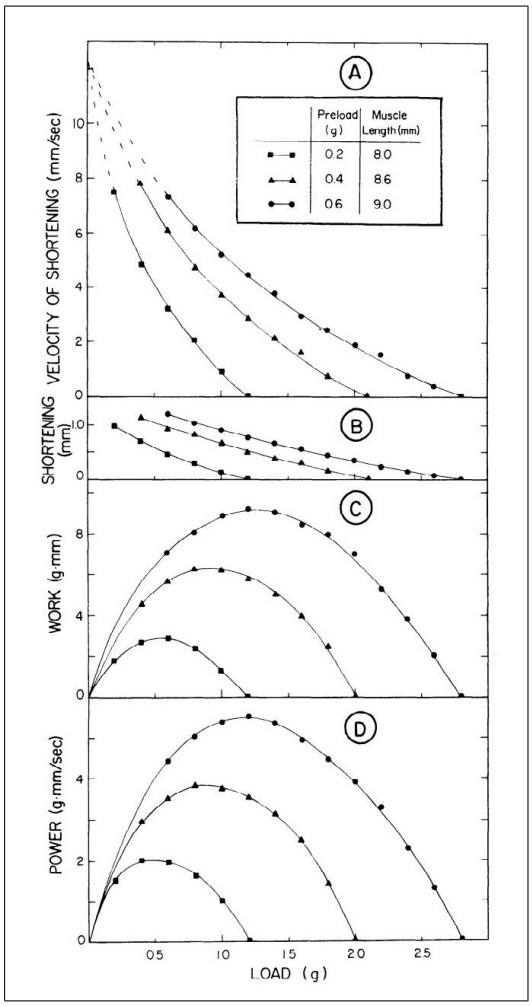

Figure 2.31 Effect of preload on velocity of shortening (A), shortening length (B), work (C) and power (D) of a cat papillary muscle [13]

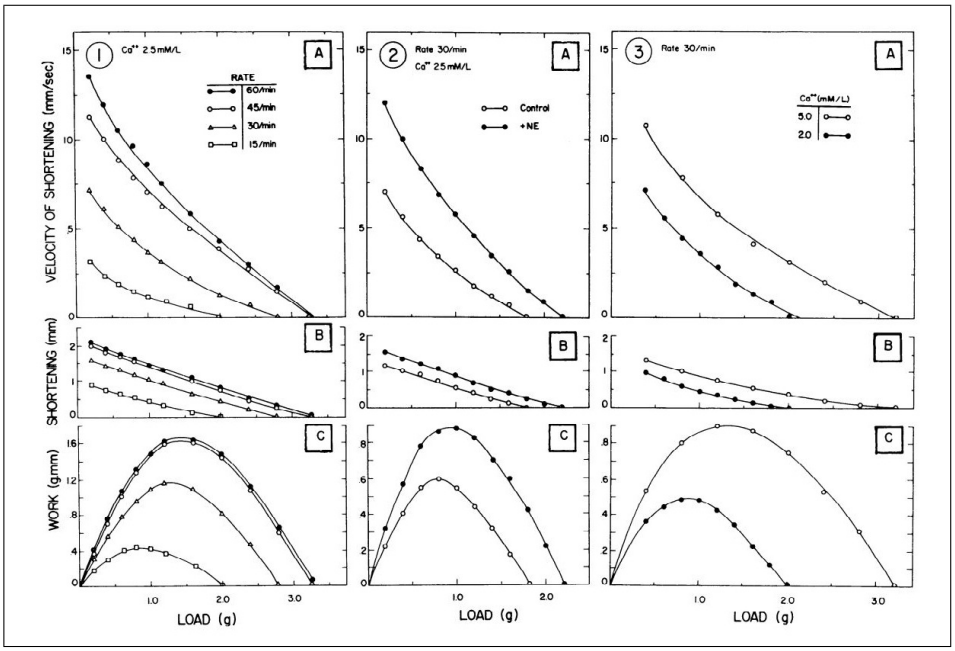

Figure 2.32 Effects of chronotropy (1) and inotropy (norephineprine (2) calcium ion concentration (3)) on velocity of shortening (A), shortening length (B), work (C) of a cat papillary muscle [13]

Sonnenblick (1965) also studied the effect of instantaneous length on the velocity and tension in cat papillary muscles. He stated that instantaneous velocity and tension of a muscle are not a function of its initial length as the maximum isometric tension is, but that, instead, they depend on its instantaneous length. He used a three-dimensional length-velocity-tension plot to illustrate this relationship (Figure 2.33). It can be seen in this plot that if the total tension on the muscle is kept constant (even when the initial lengths are changed), the velocity of shortening follows the same path once the maximum velocity is reached (i.e. initial velocity). He compares this idea with Hill's two element muscle model and claims that shortening velocity and tension of the muscle under isotonic conditions are directly equal to those of the contractile element. Therefore it may be said that the dynamics of the contractile element depend on tension, velocity, length and duration of the active state; and that it may be possible to represent the myocardium with this tension-velocity-length plot, keeping in mind that time is a hidden variable changing the path the muscle takes on the graph (Figure 2.34) [22].

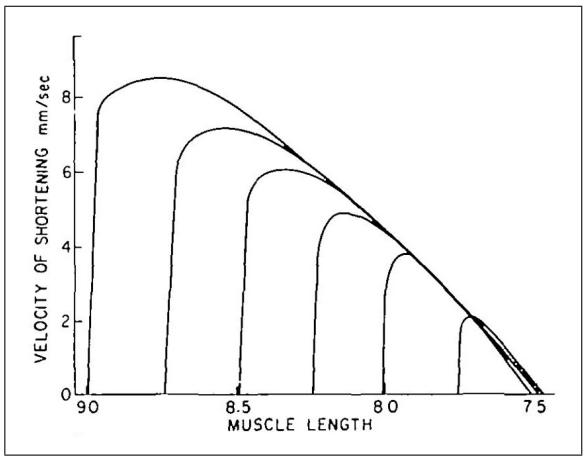

Figure 2.33 Instantaneous muscle length and velocity of shortening relationship of a cat papillary muscle for constant total load and changing preloads [22]

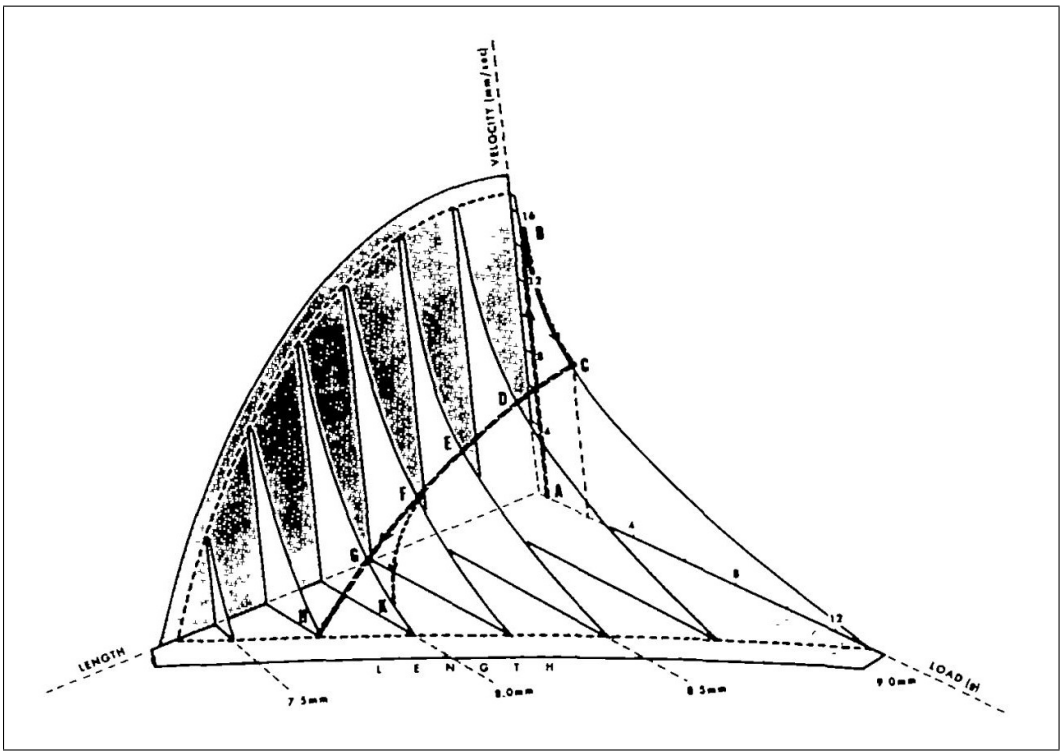

Figure 2.34 Three dimensional relationship between muscle length-velocity-tension(load) [22]

Brutsaert et al. (1969) studied the tension-velocity-length relationship of myocardial sarcomere on cat papillary muscles. Their findings were consistent with those of Sonnenblick (1965), showing the independence from preload of the relation between

velocity of contraction and instantaneous length, therefore, supporting the argument that the myocardium can be represented with a three dimensional surface, the coordinates of which are instantaneous tension, velocity and length. Additionally, this surface is affected by the activation state of the myocardium but not the time of activation [23].

Based on the observed differences between passive tension in skeletal vs. cardiac muscles, Pollack (1970) criticized conclusions on myocardial tension-velocity relationship reached in earlier studies. His main objection was to using Hill's two element model in order to define mechanisms underlying contractile phenomena. He suggested the use of more complex three-element models- such as those proposed by Voigt and Maxwell- as he found them more adequate for explaining myocardial dynamics. A natural outcome of Hill's two element muscle model is the fact that muscle tension and velocity are equal to those of the contractile element. This may be true for skeletal muscle within physiologic limits; however, it cannot represent the case for myocardium as myocardial passive tension is much higher within the same physiologic limits. However, upon repeating the calculations for a three-element muscle model, results show that ϑ_{max} depends on the initial length of (i.e. preload on) the muscle and, further that, the preload-dependence of ϑ_{max} is indistinguishable from its dependence on inotropic conditions. Thus, ϑ_{max} cannot be considered a load-independent index of myocardial contractility but that earlier results, which state that ϑ_{max} in cardiac muscle is independent of the initial length, may have been affected by experimental conditions (artifacts). Pollack also argued that ϑ_{max} calculated for the whole muscle must be different from the ϑ_{max} of the contractile element [11].

In an attempt to resolve the controversy on the preload-independence of ϑ_{max}, Parmley et al. (1972) independently studied isotonic tension-velocity relationship on cat papillary muscles. As they estimated ϑ_{max} by extrapolating the tension-velocity curves to zero load, they observed that, at preloads lower than l_{max}, even though ϑ_{max} values calculated for each constant-preload curve were close to each other, they were still dependent on the preload and increased as preload increased. The values of ϑ_{max} reached a peak at l_{max}, beyond which, as preload increased, ϑ_{max} started to decline

(Figure 2.35). When these experimental results were compared to and found consistent with simulations using either Hill's two-element or Voigt and Maxwell's three-element models, the authors concluded that ϑ_{max} cannot be used as a load-independent index of myocardial contractility [24].

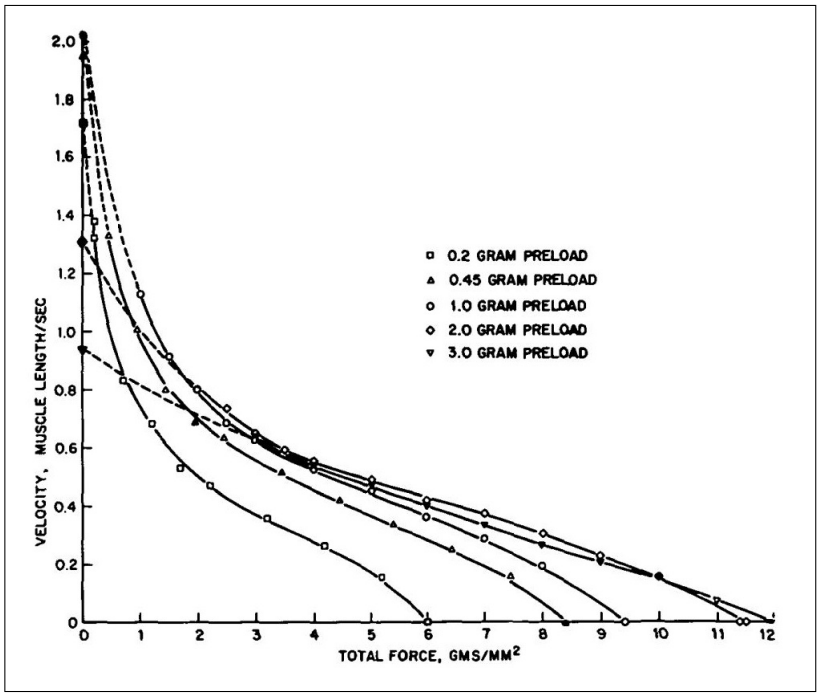

Figure 2.35 Tension(force)-velocity relationship of an auxotonically loaded cat papillary muscle [24]

2.1.3 Circulatory System

Circulatory system consists of vessels that accommodate blood as a medium to keep the homeostasis of the organism. It delivers the necessary nutrition, oxygen etc. to and removes waste products away from the tissues.

Circulatory system is mainly divided into the systemic and pulmonary circulations, according to the physiology and anatomy of each system. In Figure 2.36 a representation of human circulatory system is given.

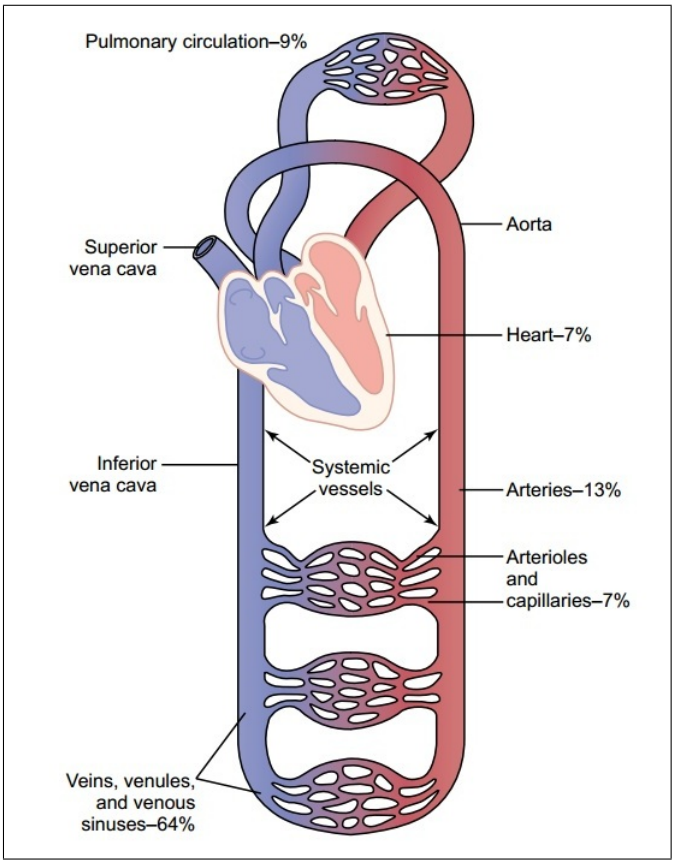

Figure 2.36 Representation of human circulatory system and its parts [3]

2.1.3.1 Systemic Circulation. Systemic circulation starts at the LV, which delivers blood to the tissues through the aorta and systemic arteries and capillaries. Nutrition and oxygen are delivered and waste products such as carbon dioxide are collected at the level of the capillaries. From there, blood continues to flow through the systemic veins to the inferior and superior venae cavae, pouring into the RA (Figure 2.36) [3].

Systemic circulation begins at high pressure in aorta and large arteries at an average pressure of 100 mmHg (120 mmHg systolic and 80 mmHg diastolic pressures). Past the large arteries, pressure drops to around 35 mmHg in small arteries and arterioles and further down to 10 mmHg in the capillaries. Pressure keeps dropping continuously inside the veins all the way to the caval opening to the right atrium, where it is almost at 0 mmHg (Figure 2.37) [3].

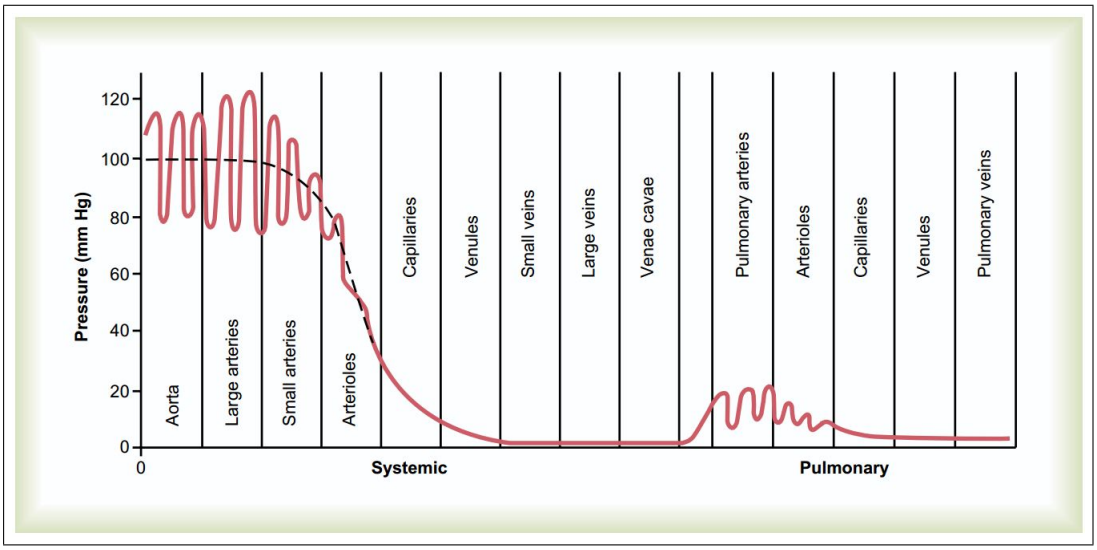

Figure 2.37 Nominal average blood pressures along the human cardiovascular system [3]

2.1.3.2 Pulmonary Circulation. Pulmonary circulation starts at the RV, continues through pulmonary arteries and capillaries and reaches the alveoli, where carbon dioxide is exchanged with oxygen. Traveling through the pulmonary veins, oxygenated blood reaches the LA and the LV, and is pumped back into the aorta (Figure 2.36) [3].

Pulmonary circulation begins at relatively high pressures in the pulmonary arteries at an average pressure of 16 mmHg (25 mmHg systolic pressure and 8 mmHg diastolic pressure). Average pressure drops to 7-9 mmHg in the pulmonary capillaries and in the LA (Figure 2.37). Despite lower pressures in the pulmonary system, blood flow is the same in pulmonary and systemic circulation [3].

2.1.3.3 Coronary Circulation. Coronary arteries and capillaries supply blood to the working muscle of the heart (Figure 2.38). Left coronary artery perfuses the anterior and lateral walls of the left ventricle and the septum between the ventricles, while right coronary artery supplies blood to the whole right ventricle and the posterior and inferior walls of the left ventricle [3].

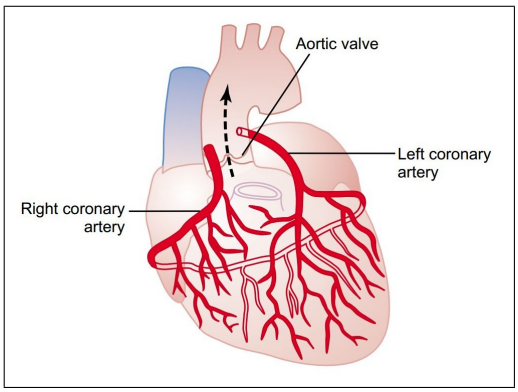

Figure 2.38 Coronary circulatory system [3]

Coronary Blood Flow (CBF) begins at the aorta and ends at the right Atrium. Under normal conditions in humans, average coronary CBF is 225 ml/min (or 3.75 ml/s), delivering 70% of its oxygen content to the myocardium and it has a considerable flow reserve for instantaneous increases in oxygen demand. Coronary flow is directly proportional to cardiac work, supplying additional oxygen in case of increased work (i.e. exercise). Excess flow is controlled via dilation of the coronary vessels [3].

Another important aspect regarding the coronary circulation is the phasic changes in the flow thorough the cardiac cycle. CBF decreases, especially in the left ventricle, as the contraction of the ventricle compresses the coronary vessels during systole, then increases again with the relaxation of the ventricle in diastole (Figure 2.39) [3].

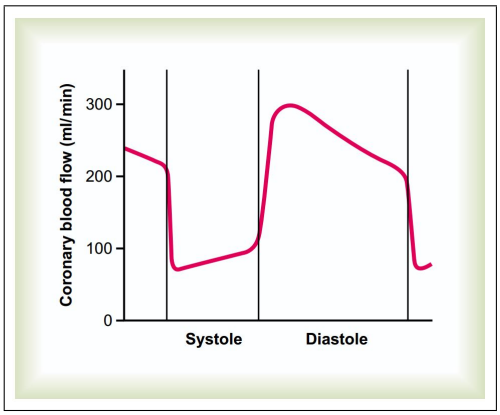

Figure 2.39 Phasic blood flow in coronary capillaries [3]

2.1.3.4 Compliance. Body vasculature displays elastic properties and as the volume within the vessel increases, internal pressure also increases. Compliance (C) is a measure of this elastic property and is expressed as the ratio of volume change (ΔV) to pressure change (ΔP) as shown in Equation 2.8.

$$C = \frac{\Delta V}{\Delta P} \tag{2.8}$$

2.1.3.5 Resistance. Resistance (R) in a hydraulic system is defined as the ratio of the pressure difference (ΔP) between two points in a pipe to the volumetric flow rate (Q) through these points (Equation 2.9).

$$R = \frac{\Delta P}{Q} \tag{2.9}$$

This pressure drop happens due to the friction between the fluid and the vessel walls. Under normal conditions blood flow in the vasculature is laminar therefore the relationship between flow and pressure follows Poiseuille's Law (Equation 2.10).

$$R = \frac{8 \cdot \mu \cdot l}{\pi \cdot r^4} \tag{2.10}$$

where μ is the dynamic viscosity of fluid, l is the length of the tube and r is the radius of the tube.

2.1.3.6 Inertance. Inertance (L) is defined as the resistance of a mass to changes in motion (i.e. acceleration). In hydraulic systems a volume of fluid in a pipe with a changing pressure difference at its ends flows with changing rate, therefore, displays this property as shown in Equation 2.11. In cardiovascular system blood shows this characteristic due to its kinetic energy by resisting to acceleration and deceleration between pulses.

$$L = \frac{l \cdot \rho}{\pi \cdot r^2} \tag{2.11}$$

where ρ is the density of fluid, l is the length of the tube and r is the radius of the tube.

2.1.4 Physiological Feedback Control of the Cardiovascular System

Cardiovascular system has important and complex interactions with other organs and systems for regulating the functions of the heart and the vasculature. These interactions may be commonly called Physiological Feedback Systems (PFS). PFS can affect the cardiovascular system mainly via nervous and humeral systems [3].

Nervous system can change cardiac response dramatically via sympathetic or parasympathetic (vagus) nerves. Signals from these nerves can manipulate HR and contractile force generated by cardiac muscle. Therefore regulating the CO and the pressures within the cardiovascular system [3].

Sympathetic neural pathway signals increase HR from the average 70 beat/min to and in some cases beyond 200 beats/min. Also these signals can double contractile force of the cardiac muscle if needed. All these effects combined can double or even triple the CO [3].

In contrast parasympathetic (vagal) neural pathways show an inhibitory effect. Signals from these neurons can reduce the HR and even stop the heart for a few seconds. Also these signals can decrease the contractile power of the cardiac muscle to one fifth of normal [3].

The nervous system regulates the cardiovascular system via baroreceptor, mechanoreceptor and chemoreceptor signals, which carry information about blood vessel pressures and tissue oxygen concentrations and, in cases of deviations from normal physiology, serve as a feedback mechanism allowing an error signal to be generated and triggering the necessary sympathetic or parasympathetic compensatory mechanisms [3].

Humoral mechanisms control blood flow and/or pressure by adjusting the vascular tone and cardiac contractility via circulating hormones such as Norepinephrine, Epinephrine, Angiotesin II etc, which act as vasodilators/constrictors and inotropic agents [3].

Ion concentrations are managed mostly by the renal system. The generation of action potential, the activation of cardiomyocytes, and the contraction of the myocardium are directly proportional to the number of ions such as Na^{+}, K^{+} , Mg^{+2} and Ca^{+2}, that are present in intra- and extra-cellular media. Therefore, alterations in the concentrations of these would result in blood pressure variations via changes in cardiac activation and vascular elasticity [3].

2.1.5 Energetics of the Heart and Myocardial Oxygen Consumption

Suga (1979) studied the relationship between cardiac oxygen consumption and the Pressure-Volume Area (PVA) in PVL. PVA is defined as the sum of Potential Energy (PE) stored during IVC and the Stroke Work (SW), in other words EW, performed by the left ventricle (Figure 2.40). If the ventricular chamber is assumed to be an elastic material with time-varying stiffness, the PE remaining at the end of systole can be equated to the triangular area between the points defined by theoretical zero-pressure volume (V_0), end systolic pressure (P_{es}) and end systolic volume (V_{es}). The work done by the heart is the SW and it is defined by the area surrounded by the PVL. Since the main energy production of the heart is through oxidative processes, the energy it consumes can directly be related to its oxygen consumption. Hence Suga suggested that the total energy input of the heart may be found by adding PE and SW. For this purpose, the time-varying elastance model of the heart was utilized. Therefore the total oxygen consumed by the heart should be related to PVA and an additional basal metabolism content. Work done on canine heart models showed a linear relationship between oxygen demand (D_{O2}) of the heart and the PVA as given in Equation 2.12 [25].

$$D_{O2}\left[\frac{mlO_2}{beat}\right] = 1.37 \cdot 10^{-5}\left[\frac{mlO_2}{mmHg \cdot ml}\right] \cdot PVA\left[\frac{mmHg \cdot ml}{beat}\right] + 0.027\left[\frac{mlO_2}{beat}\right] \quad (2.12)$$

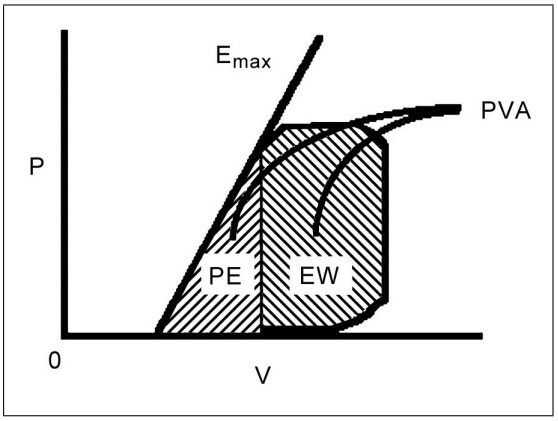

Figure 2.40 A representative PVL showing PE, EW (i.e. SW) and PVA [26]

Suga (1990) wrote a review of his extensive studies about the cardiac oxygen consumption and its relation to PVA. He studied both on mathematical models and in-vivo (on canine and leporine hearts) to accumulate sufficient data sets to relate PVA and cardiac oxygen consumption reliably. Additionally he studied the effects of various physiological and anatomical conditions (i.e. loading conditions, heart rate, heart size, inotropic states etc.) on this relationship. An important point of this study is the normalization of the cardiac oxygen consumption and PVA relationship to the mass, M, of the LV, therefore acquiring an augmented linear relationship as [27]:

$$\begin{aligned} D_{O2}\left[\frac{mlO_2}{beat \cdot 100g}\right] =& 1.5 \cdot 10^{-5}\left[\frac{mlO_2}{mmHg \cdot ml \cdot 100g}\right] \cdot M[g] \cdot PVA\left[\frac{mmHg \cdot ml}{beat}\right] \\ &+ 0.024\left[\frac{mlO_2}{beat \cdot 100g}\right] \end{aligned} \quad (2.13)$$

2.2 Models of the Cardiovascular System

Both physical and mathematical models of the cardiovascular system have been created by prior researchers.

Physical Models: Physical models, also known as CVMCs, are hydro-mechanical set-ups that can mimic the physiology of the human cardiovascular system in an accurate manner. CVMCs are used for in-vitro tests of the performance of medical devices such as artificial heart valves, ventricular assist devices, artificial hearts etc. CVMCs can be as basic as a preload chamber connected to an afterload via a hydraulic resistance and pipes that deliver constant flow; or made into complex set-ups that mimic physiological phenomena such as flow pulsatility, hydraulic resistance, vascular compliance, fluid inertance in order to simulate pulmonary and systemic circulations, cardiac valve regulation, physiological feedback control mechanisms etc.

As early as 1959, Kolff and his associates constructed a CVMC, which included systemic and pulmonary circulation systems, using compressed air to activate the ventricles. The system contained no hydraulic resistance elements but allowed manipulation of the diastolic pressure via a water column [28]. In an attempt to test artificial hearts in vitro, Donovan et al. (1974) designed a CVMC which became a basis for future designs due to its consistency with bovine physiology. Although the system did not contain ventricles, which limited its range of applications, it consisted of systemic and pulmonary atrial and venous chambers [29]. Cornhill et al. (1977) crated a CVMC using a collapsible silicone bag contained in a pressure-controlled air-tight box. This system has been used for in vitro testing of aortic heart valves, although the neglect of inertial effects and atrial contractions somewhat limited the accuracy of the system [30]. Rosenberg et al. (1981) outlined the CVMC design of the Pennsylvania State University Mock Circulatory System, initially developed in 1971. The purpose of this CVMC was to test LVAD performances. Its major features were the inclusion of both systemic and pulmonary circulations with resistance, compliance and inertance components, and LVAD connection ports. Various cardiac conditions could be reproduced in a controllable fashion using this system [31]. Koenig et al. (2004) constructed a

CVMC for in vitro testing of LVADs. This system allowed the user to test various LVAD assistance levels via implementation of the Frank-Starling Law. The left ventricle of the system was contained in an airtight box driven with external pressurized air. The system also included a latex tube in a separate enclosed chamber kept at the same external pressure as the left ventricle in order to simulate coronary flow. A limiting factor of the set-up was the lack of pulmonary circulation [32]. Pantalos et al. (2004) designed a CVMC with an atria and a ventricle connected to the systemic circulation. The system, which included the coronary but not pulmonary vasculature, could account for inertial effects and allowed simulations of normal, heart failure and recovery physiologies [33]. Litwak et al. (2005) created a CVMC to test continuous and pulsatile flow LVADs. This system, which was capable of working in normal and heart failure modes, included an atrium and a ventricle made of elastic polymer sacs placed in pressurized chambers. Coronary flow was controlled by placing the mock coronary circulation in a chamber pressurized at the same level as the ventricle [34]. Liu et al. (2005) designed a CVMC with LA, LV, systemic circulation, RV and pulmonary circulation. Both ventricles were controlled with external pressure to simulate the pulsatile flow and check valves were used to create unidirectional flow in the system. This system was used to test continuous flow LVADs under healthy rest/sleep/exercise modes, resting CHF and partially recovered CHF conditions. However the incapability of this system to comply with the Frank-Starling Law caused unreliable test results [35]. Timms et al. (2005) constructed a complete CVMC that obeyed the Frank-Starling Law and was capable of correctly mimicking normal and CHF conditions. Unfortunately, ventricular volume could not be measured in this set-up [36]. In another CVMC designed by the same investigators (2011), both the pulmonary and systemic circulations were included but lags in pressure measurement in LV and aorta prevented correct simulation of the human cardiovascular system [37]. Eken (2013) modeled a CVMC that consists of hydraulic compliance chambers for LV, aorta, systemic capillaries, systemic venous pool (systemic veins and RA), RV, pulmonary arteries, pulmonary capillaries, pulmonary venous pool (pulmonary veins and LA). However the constructed CVMC included only four chambers (LV, aorta, systemic venous pool and pulmonary venous pool) of the initial design. Mock left ventricle in the system has been driven by pressurized air and controlled with time varying elastance [38].

Mathematical Models: Mathematical modeling is a fundamental approach to understand the underlying hemodynamic mechanisms and to design methods to mimic them satisfactorily. Two main methods of modeling cardiovascular system used in the literature are distributed models and lumped models.

Distributed models are defined via partial differential equations to simulate pressures and flows. These models can vary between three-dimensional models and one-dimensional models. As three-dimensional and two-dimensional models are quite complicated mostly one dimensional are used to study wave propagation patterns and their effects on flow and pressure [39].

Lumped (zero-dimensional) models are defined via ordinary differential equations. This models are usually developed using hydraulic and electrical system analogy given in Table 2.1, according to which electrical circuit elements (resistance, capacitance and inductance) simulate vascular hydraulic resistances, vascular and ventricular compliances and blood inertance, respectively; while diodes are used to achieve unidirectional flow as in the case of heart valves. Even though electrical elements fall short of providing an exact replica of cardiovascular hemodynamics, hemodynamic properties of the cardiovascular system can be approximated at discrete points of interest [39].

Table 2.1
Analogy between Hydraulic and Electrical Systems

	Hydraulic System	Electrical System
Independent Variable	Volume	Charge
Effort Variable	Pressure	Voltage
Motion Variable	Flow	Current
Energy Dissipating Element	Hydraulic Resistance	Electrical Resistance
Potential Energy Storage	Compliance	Capacitance
Kinetic Energy Storage	Inertance	Inductance

Westerhof et al. (1969), making use of electro-hydraulic analogy, crated a systemic circulation model via cascade formation, which was able to reproduce physiological pressure and flow values quite closely [40]. Ding et al. (1994) designed the mathematical model of the circulatory system connected to an artificial heart. Vascular compliances were simulated with nonlinear capacitances, a baroreceptor feedback control mechanism was included, and control of the model was realized with pulse frequency modulation [41]. To test a LVAD in parallel with in vivo tests, Mitsui et al. (1998) also developed a mathematical model of the cardiovascular system, where ventricular function was simulated using variable capacitors [42]. Vollkron et al. (2002) crated a lumped-parameter mathematical model of cardiovascular system in MATLAB/Simulink. The model consisted of LV, systemic circulation, RA, RV, pulmonary circulation and LA. Contractile properties of ventricles and atria were simulated via variable capacitances and diodes were used to operate as heart valves. The model could be augmented with an LVAD model to test its performance in the computer environment [43]. Wu et al. (2003) developed a mathematical model of the human cardiovascular system using a variable resistor and variable nonlinear capacitors to simulate total peripheral resistance and ventricular ejection and filling phases. This system was used to evaluate the performance of a physiological controller [44]. Ottesen et al. (2004) created a mathematical model of the cardiovascular system using lumped parameters. Their model consisted of LV, systemic circulation, RA, RV, pulmonary circulation and LA. Atria were modeled using constant compliances and the functions of LV and LA were simulated via variable compliance elements. For better representation of the hemodynamics in different parts of the cardiovascular system, both systemic and pulmonary circulations were partitioned into five three-element Windkessel models in cascade formation and augmented by inertances in certain sections. Both ventricles were driven via time varying elastance. The shape of pressure and flow tracings as well as that of PVL graphs obtained for LV and RV was consistent with the literature. Additionally, the inertances successfully modeled the backflow from aorta to the LV during the closure of AV [39]. Vrettos et al. (2005) designed a mathematical model of the cardiovascular system using a three-element (two resistances and one compliance) Windkessel approach in order to study the effect of arterial compliance on cardiac power. Although they were able to show an inverse relationship between the two vari-

ables, their experimental design was limited by the absence of an inertial element and by their assumption of stationary flows and pressures within the system [45]. Hassani et al. (2007) created a mathematical model for human cardiovascular system. Ventricular function was simulated using variable voltage sources. All passive electrical elements representing heart chambers and unidirectional valves as well as systemic and pulmonary circulations were lumped into 42 Windkessel groups in cascade configuration. The hemodynamic results of the model were consistent with the literature [46]. Gregory (2009) developed a mathematical model for the cardiovascular system as a first step to acquire a test platform for LVADs. The cardiovascular tract included LV, aorta, systemic circulation, RA, RV, pulmonary arteries, pulmonary circulation and LA. All vessels and chambers were modeled with lumped electrical resistance, capacitance and inductances. However results did not accurately represent physiological measurements form the literature since a time-varying elastance was not used as a load-independent ventricular driver [47]. Eken (2013) designed a mathematical model of the human cardiovascular system that was later used to construct a hydro-mechanical CVMC, which assumed lumped hydraulic resistances and compliances. The physical system, controlled via time varying elastance, consisted of LV, aorta, systemic capillaries, systemic venous pool (systemic veins and RA), RV, pulmonary arteries, pulmonary capillaries, pulmonary venous pool (pulmonary veins and LA) [38].

One may argue that distributed models are more accurate than lumped models for simulating cardiovascular hemodynamics. However distributed models are heavier on the computational side especially if the whole circulation system is concerned. On the other hand, lumped models are more suitable for coupling with control systems which can mimic the physiological feedback mechanisms of the organism [39].

2.2.1 Windkessel and Lumped Modeling

Windkessel modeling, essentially lumped modeling, is the most basic way of representing cardiovascular system in terms of well-known parameters. Two-element Windkessel model was first formulated by Otto Frank in 1899 (Figure 2.41) [48].

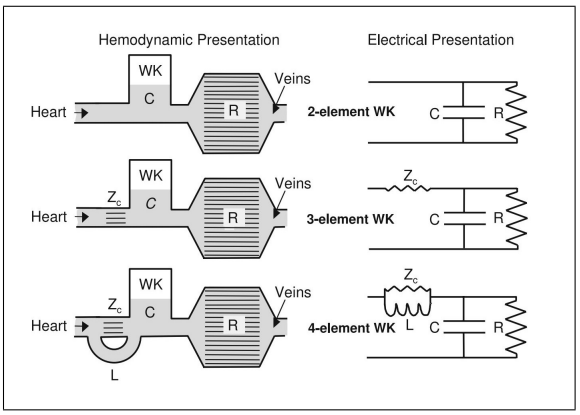

Figure 2.41 Windkessel groups with their hemodynamic (hydraulic) and electric analogous circuits [48]

Modeling the cardiovascular system with a capacitor that serves as the compliance of the arterial system and a resistor to represent the total peripheral resistance is a simple and convenient way to simulate diastolic properties of the cardiovascular system as a first-order exponential decay of the pressure in the arterial tree. However this approach cannot model systolic hemodynamics because of the decrease of the input impedance modules towards zero for increased frequency and phase angle approaching -90° (Figure 2.42). To overcome this limitation an input impedance (usually just a resistance) has been implemented to the two element Windkessel model so as to acquire the three-element Windkessel model (Figure 2.41) [48].

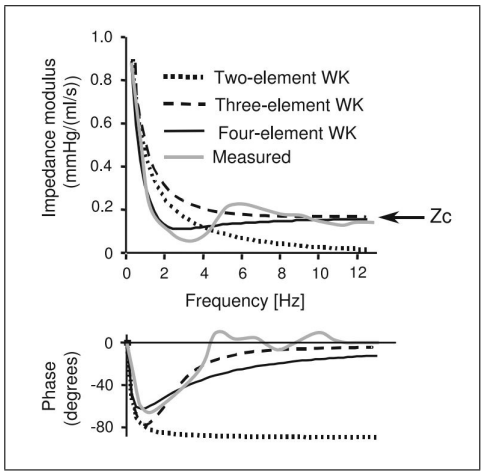

Figure 2.42 Output impedance of the Windkessel groups and experimental measurements, top: impedance modulus, bottom: phase angle [48]

With the three-element Windkessel model, it becomes possible to set high frequency input impedance modulus to a steady-state and, therefore, to more accurately model systolic properties. Although the three-element Windkessel model can simulate the whole cardiac cycle accurately. a small error still remains in the lower frequency range of the input impedance modulus (Figure 2.42). Therefore an additional inertance has been inserted by Burattini and Gnudi in 1982 to represent total arterial inertance, thus creating the four-element Windkessel model (Figure 2.41). However, due to the difficulty of estimating the physiologic value of this new component, three-element Windkessel models are widely favored over the four-element ones [48].

To improve the modeling of the cardiovascular system, multiple three-element Windkessel configurations can be linked to each other in cascade formation (Figure 2.43). This approach enables the modeling of different parts of the cardiovascular system separately, as opposed to modeling everything with two resistances and a compliance, and allows more quantifiable simulations of the real system.

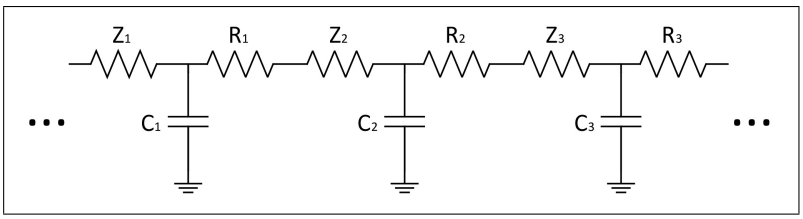

Figure 2.43 Cardiovascular system modeling with Windkessel groups in cascade

As lumped models are discrete and are just estimations of the real continuous system they have limitations. Wave transmission, blood flow distribution, local vascular effects, pressure distribution cannot be studied. However these models can estimate the flows and pressures at discrete points of the cardiovascular system [39, 48].

2.2.2 Models of Coronary Circulation

The coronary circulation serves the fundamental function of nurturing the heart. Modeling and inspecting its function therefore holds great importance to understand the supply and demand cycle of the myocardium. As coronary vessels encircle the heart and penetrate into the myocardium, their hemodynamics is affected by the biomechanics and hemodynamics within the heart chambers, especially in the left ventricle. The pressure developed by the contracting ventricle compresses the vessels within the myocardium and blocks blood flow during systole. Also to supply excess oxygen and nutrients in case of necessity (e.g. during exercise) coronary vessels can change their diameters accordingly. Mimicking these phenomena increases the accuracy of coronary circulation modeling.

Bruinsma et al. (1988), created a distributed coronary circulation model, composed of a network of resistances and capacitances, which incorporated the compression effects of intra-ventricular pressure on the coronary vessels during systole, both in terms of decreased capacitance and increased resistance. Their model was able to mimic the phasic blood flow in the coronary circulation in parallel with the previous literature. However Bruinsma et al. only modeled the coronary vessels in their fully dilated form. Therefore their model lacked the constraint arising from supply-demand equality [49].

In order to study the effects of aortic stenosis on the coronary circulation and the coronary flow reserve, Garcia et al. (2009) modeled the left ventricle using a time-varying elastance, the ascending aorta and systemic circulation using a three-element Windkessel model, and the coronary circulation using a lumped parameter model consisting of resistive and capacitive elements. The model also incorporated the volume-reducing effects of intra-myocardial pressure on the vessels within the myocardium as well as the dilation and constriction of coronary arteries due to oxygen supply-demand equilibrium. Their model was successful at mimicking the coronary flow wave patterns both for normal physiology and for aortic stenosis, and showed that a coronary flow reserve exists both for healthy and diseased examples [50].

To generate a model capable of estimating CBF, Arthurs et al. used a mathematical model that only required the heart rate and peak aortic pressure as input. Using several resistive and capacitive elements controlled by feedback and feedforward mechanisms, they were able to incorporate the effects of both the intra-myocardial pressure and the myocardial oxygen supply-demand equilibrium. The coronary circulation was coupled to a time-varying elastance-controlled left ventricle in series with a three-element Windkessel systemic circulation. The model was capable of mimicking coronary phasic flow patterns as well as coronary dilation and constriction in response to keeping the oxygen supply-demand equilibrium during resting and exercise modes [51].

2.3 Control of Cardiovascular Mock Circuitry

Much as the output of cardiovascular simulation circuits is desired to mimic actual physiologic variables such as pressures, flows and volumes generated inside the cardiovascular system, the input into these systems is also required to mimic the activation and control signals that naturally occur and are observed in mammalian physiology.

2.3.1 Elastance-Based Control

Elastance is defined as the relationship between the volumetric changes and the resulting pressure changes inside a deformable capacitive element. As such, it is an ideal time-varying input variable, with which cardiac dynamics can be driven. During the cardiac cycle, elastance reaches its maximum value, E_{max}, at end-systole and, as shown by Suga et al. (1973), this end systolic elastance, or E_{max}, can be represented via a linear relationship due to its independence from cardiac preload and afterload. Elastance-based control is indeed used as a fundamental control system in cardiovascular simulation and mock circuits. This approach allows researcher to mimic not only the load-dependent Frank-Starling mechanism of the heart, but also the intrinsic cardiac contractility, which can only be altered through inotropic intervention. Using the

ventricular volume, $V_V(t)$, zero-pressure volume, V_0, and the time-varying elastance function, $E(t)$, it is possible to acquire the ventricular pressure, $P_V(t)$ (Equation 2.14) [52].

$$P_V(t) = E(t) \cdot [V_V(t) - V_0] \tag{2.14}$$

Elastance is dependent not on the cardiac preload and afterload; but only on the inotropic state of the heart. Therefore it is possible for a system to be controlled with elastance to respond changes in the preload and the afterload accurately and predictably. This approach enables the researchers to define an elastance signal as an arbitrary function of time to mimic the inotropic state and the pathology of the heart [52].

Baloa et al. (2001) defined a novel approach to time-varying elastance-based control, where the cardiovascular model (the plant) generated the instantaneous LV volume, which was fed into the elastance block to generate the instantaneous LV pressure. Their setup enabled them to adjust the compliances and the resistances of the test systems to recreate changing preload and afterload effects. They validated this approach both in mathematical simulations and in CVMC tests, and reported that it was successful as a new LVAD testing platform [52].

Loh et al. (2004) designed an elastance-based feedback controller and tried it on a CVMC. They, too, used the control mechanism to define the volume of the ventricle via a time-varying elastance signal to produce the ventricular pressure. Although their system produced acceptable pressure wave forms, resulting PVL graphs lacked the IVC and IVR regions, which was an important shortcoming [53].

Colacino et al. (2008) proposed a modified elastance-based control model, which aimed to reduce the sensitivity of the system to pressure disturbances. After testing the performance of this model against more conventional systems on mathematical and physical simulation platforms, they concluded that the mathematical elastance

model was capable of eliminating pressure oscillations specifically during ventricular filling. Although the approach was marginally better than conventional elastance-based control, they advised the use of conventional methods in cases where simplicity were a factor. Their CVMC test results did not reflect the in vivo situation, though, and that was conceded by the authors as a limitation of their research [54].

Yu et al. (2009) augmented a time-varying elastance controlled cardiovascular simulation system with a mathematical LVAD model. As in the previous two studies, elastance input and pressure values gathered from the model used for generating the volume of the ventricle in this study. Time-varying elastance was dependent on the given value of the E_{max} therefore changes in E_{max} allowed the authors control on the contractile state of the heart. By reducing the value of E_{max} the model could be run in heart failure mode and the effectiveness of the LVAD could be tested. Their results were similar both when simulation system was operated in heart failure mode and the LVAD was activated, and when LVAD was turned off and the system was run in normal mode. Like in the previous study, this system was unavailable to reproduce the IVC and the IVR conditions of the ventricle [55].

2.4 Summary Considerations for Determining the Objectives of the Present Research

In the light of the forgoing discussion, it is clear that a new and improved algorithm is needed for a more natural simulation of the cardiovascular driving mechanism. More specifically, said mechanism should reflect the underlying myocardial biomechanics and generate the elastance as an output. Furthermore, it has been argued that all systems in a living organism must be adapted to work in the optimal state so as to withstand the external conditions. The cardiovascular system is no exception to the rule; and mock systems should be designed with this principle in mind if acceptable physiological accuracy is desired. This last condition holds true since the ultimate motivation to design a virtual (mathematical) model is usually, as in the case of the present

work, to duplicate its physical (hydro-mechanical) version as a CVMC. With this last consideration in mind, the mathematical model should be optimally controllable in real-time and, therefore, require minimal computational time even when physiological delays in information transfer between the control and feedback variables, regardless of how these variables may be chosen, are accounted for.

As far as myocardial biomechanics are concerned, a cardiac muscle fiber can be in one of two possible states: passive and active. In the passive state, the myocardium is not activated via an action potential and responds to external loading conditions only through its elastic properties. This relationship is reflected in the passive tension curve of the myocardial length-tension graph obtained in isometric experiments (Figure 2.25). By contrast, the active state occurs when the myocardium is activated via an action potential. Theoretically, in the active state, cardiac muscle should contract in one of two ways: isometrically (constant length) or isotonically (constant load). Indeed, during the IVC or the IVR phase of myocardial activation, since ventricular volume is not changing, the contraction of individual myocardial fibers may be approximated to an isometric contraction. However, during the ejection phase of the ventricles, the contraction of myocardial fibers is not purely isotonic. The fibers do shorten (hence intra-ventricular volume decreases) but the load (aortic pressure) against which the fibers shorten increases in proportion to the volume of the ejected blood (the constant of proportionality being aortic capacitance). This type of contraction, where the muscle shortens and the afterload increases, which is peculiar to the myocardium only, is called auxotonic contraction. Thus, the active state of the myocardium during ejection should be modeled as an auxotonic relationship, preferably with a single equation, which combines the isometric and isotonic contractile dynamics. Hence it becomes possible to model the myocardium using both auxotonic and passive relations, simultaneously within the same cardiac cycle.

Based on this dichotomous division of the myocardial states into an active and a passive state, systole and diastole can also be defined as states of active muscular contraction and passive muscular relaxation, respectively. Therefore, systole is to be considered as the sum of IVC and ejection phases, whereas diastole is the sum of IVR

and filling phases. This state change from activation to deactivation can be defined with a single binary (on-off) activation signal "u". Alternatively, it may also be conceived that active state begins as the MV closes and lasts until peak ejection pressure is reached, and that relaxation begins immediately as ejection pressure starts to decline until the closure of the MV. This approach also allows the design of control signal "a" as a fuzzy control variable, which combines the active and passive states in a certain proportion, according to which a certain volumetric ratio of myocardial fibers are in active state while the remaining volume is not yet activated; or, even when 100% of fibers are activated, a given proportion is contracting auxotonically while the remaining percentage is contracting isometrically.

An additional point, related to the concept of contraction above, concerns the intrinsic power (contractility) of the myocardium. Most physical and mathematical methods drive the CVMC using time-varying elastance, which is defined as the instantaneous pressure-volume ratio and, therefore, is a secondary, empirically generated variable. As such, it only indirectly reflects the ultrastructural mechanisms (sliding filaments) and the biomechanics (isometric/isotonic/auxotonic modes of contraction) of myocardial activation. Accounting for the length-tension-velocity relationship at the micro-anatomic (sarcomeric) level first and then translating it unto the ventricular dimension would arguably provide a more direct approach to determining the pressure-volume-elastance relationship at the macro-anatomic level.

Oxygen demand of the contracting muscle, on the other hand, must be met via the oxygen supply carried by the CBF, imposing an energy balance constraint on the system, therefore making the control of CBF acquire a crucial role in cardiac function. The most fundamental physiological phenomenon that controls CBF is the vasodilation of coronary arteries; therefore, the flow can be increased or decreased via vessel radius in accordance with Poiseuille's Law. This supply and demand equilibrium can be exploited in future research as a constraint for optimal control.

Keeping the foregoing considerations in mind, the design requirements of the circuit are grouped under three categories:

1. **Anatomical requirements:**

   - The model should simulate static physical properties (inertances, resistances, capacitances) of cardiovascular system compartments as realistically as possible.
   - The model should be modular so that sub-systems (right heart, pulmonary circulation, arterioles, etc.) can be added/subtracted to increase/decrease the complexity of the system when necessary.
   - Total blood volume should remain constant (except when bleeding or fluid infusion is simulated).

2. **Physiological requirements:**

   - Dynamic state variables such as systolic and diastolic pressures, and blood volumes and flow rates should remain within their respective nominal physiological range.
   - The response of the model to parameter variations (e.g. myocardial contractility) and external disturbances (e.g. loading) should be similar to human physiologic performance under rest/exercise or health/disease conditions.
   - The model should accurately reproduce load-dependent (Frank-Starling Law) and load-independent (end-systolic pressure volume relationship and power over EDV squared) performance indexes.
   - Coronary flow should be controlled via oxygen supply-demand balance.

3. **Control requirements:**

   - The system should be controllable with as few inputs (ideally a single input) as possible to enable future optimal control implementations.
   - The system should be compatible with future formulation as an Optimal Control Problem.

3. MATERIALS AND METHODS

In this chapter, methods followed to model the cardiovascular system will be given. A novel approach on generating the intra-ventricular pressure, based on biomechanical properties of myocardium, will be discussed and control of the system will be explained.

Real circulatory systems are continuous systems that can be mathematically approached as infinite number of resistance, inertance and compliance groups connected to each other in tandem. This distributed modeling approach is realistic; however, as explained in previous sections, they are quite heavy on the calculation side and, therefore, not easily applicable, particularly to physical systems. One way to avoid this problem of practicality, the infinite number of elements can be lumped into a discrete number of Windkessel groups, each representing a section of the circulatory system. Although lumped models are not as realistic as distributed models, they are accurate and fast enough to work with. Similarly, atria and ventricles of the heart can be approached as constant-compliance or time-varying elastance chambers depending on the complexity of the model.

In this thesis, cardiovascular system was modeled in five segments consisting of the systemic, pulmonary and coronary circulations and the left and right hearts, using three element Windkessel models linked in cascade. For the mathematical model of the hydraulic circuit, its electrical analogue, given in Figure 3.1, was used. Related equations that describe the dynamics of respective segments are given in the following sections.

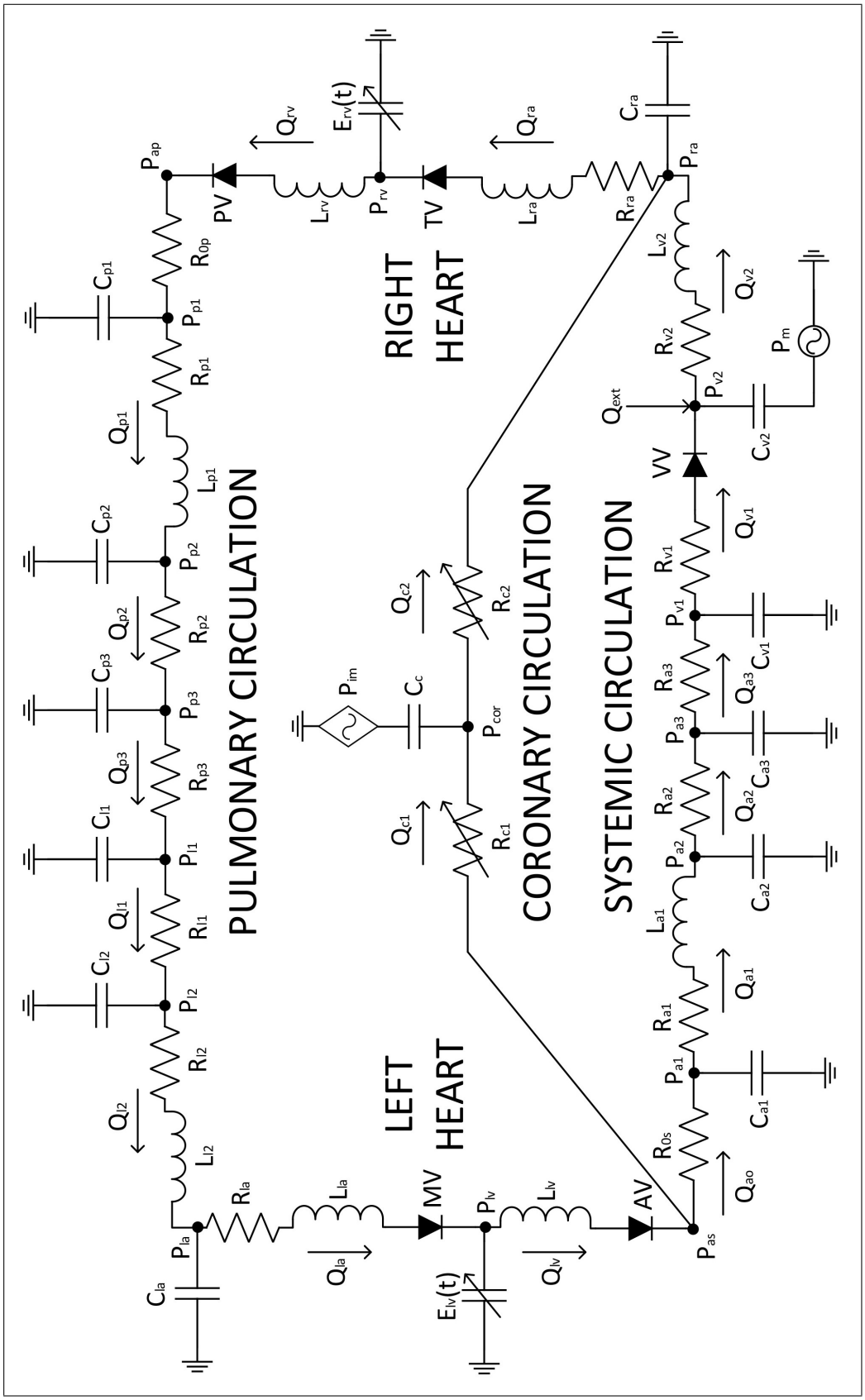

Figure 3.1 Cardiovascular system model

Inputs to the plant (cardiovascular system) in Figure 3.1 was sent from an actuator (pressure generator) with data flow as shown in the following block diagram (Figure 3.2).

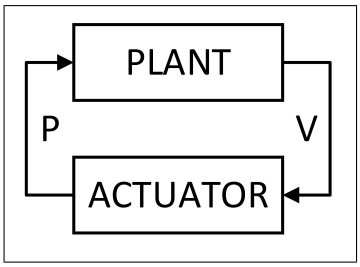

Figure 3.2 Basic Block Diagram of the System

3.1 Modeling the Circulatory System

In this section modeling of the systemic, pulmonary and coronary circulations will be explained. In the equations, P is defined as the pressure of the relevant node, V is defined as the volume in the relevant chamber of compliance, C; and Q is defined as the flow of fluid with inertance, L, between relevant nodes connected through the resistance, R. Parameters used in these equations are given in Appendix A and Simulink block diagrams are given in Appendix B.

3.1.1 Modeling Systemic Circulation

The electrical analogy of the hydraulic circulatory system (Table 2.1) was constructed by means of ordinary differential equations, which originate from Kirchhoff's Voltage and Current Laws (KVL and KCL, respectively). The model of the systemic circulation has been divided into three arterial (subscripts $a1$ through $a3$) and two venous (subscripts $v1$ and $v2$) groups as follows:

Systemic arterial groups:

1. First group: From C_{a1} to C_{a2}

$$\dot{Q}_{a1} = \frac{1}{L_{a1}} \cdot (P_{a1} - P_{a2}) - \frac{R_{a1}}{L_{a1}} \cdot Q_{a1} \tag{3.1}$$

$$\dot{V}_{a1} = Q_{ao} - Q_{a1} \tag{3.2}$$

$$P_{a1} = \frac{1}{C_{a1}} \cdot (V_{a1} - V_{un,a1}) \tag{3.3}$$

2. Second group: From C_{a2} to C_{a3}

$$Q_{a2} = \frac{1}{R_{a2}} \cdot (P_{a2} - P_{a3}) \tag{3.4}$$

$$\dot{V}_{a2} = Q_{a1} - Q_{a2} \tag{3.5}$$

$$P_{a2} = \frac{1}{C_{a2}} \cdot (V_{a2} - V_{un,a2}) \tag{3.6}$$

3. Third group: From C_{a3} to C_{v1}

$$Q_{a3} = \frac{1}{R_{a3}} \cdot (P_{a3} - P_{v1}) \tag{3.7}$$

$$\dot{V}_{a3} = Q_{a2} - Q_{a3} \tag{3.8}$$

$$P_{a3} = \frac{1}{C_{a3}} \cdot (V_{a3} - V_{un,a3}) \tag{3.9}$$

Systemic venous groups:

1. First group: From C_{v1} to C_{v2}

$$Q_{v1} = \max\left[\frac{1}{R_{v1}} \cdot (P_{v1} - P_{v2}), 0\right] \tag{3.10}$$

$$\dot{V}_{v1} = Q_{a3} - Q_{v1} \tag{3.11}$$

$$P_{v1} = \frac{1}{C_{v1}} \cdot (V_{v1} - V_{un,v1}) \tag{3.12}$$

2. Second group: From C_{v2} to C_{ra}

$$\dot{Q}_{v2} = \frac{1}{L_{v2}} \cdot (P_{v2} - P_{ra}) - \frac{R_{v2}}{L_{v2}} \cdot Q_{v2} \tag{3.13}$$

$$\dot{V}_{v2} = Q_{v1} - Q_{v2} + Q_{ext} \tag{3.14}$$

$$P_{v2} = \frac{1}{C_{v2}} \cdot (V_{v2} - V_{un,v2}) + P_m \tag{3.15}$$

In Equation 3.2, Qao is the flow going towards the systemic circulation after the coronary circulation branches off, and is given by:

$$Q_{ao} = Q_{lv} - Q_{c1} \tag{3.16}$$

In Equation 3.10, the output of function $\max(x, y)$ is the greater of x and y, and, as such, it models the venous valves as a means of preventing reverse (negative) flow. In Equation 3.14, Q_{ext} represents external fluid intake or intravenous serum infusion into the system (negative Q_{ext} represents fluid loss, e.g. through sweating or bleeding).

In Equation 3.15, P_m is the additional pressure exerted on the veins by the exercising skeletal muscles, which effectively increase venous return to the right heart. It is given by:

$$P_m = |\gamma \cdot \sin(2 \cdot \pi \cdot f)| \tag{3.17}$$

where γ and f represent the magnitude of muscular pressure on the vasculature and the frequency of exercise (i.e. frequency of leg movement during walking or running), respectively.

Additionally, volume subscript un defines the unloaded volume of the respective compliance, should zero pressure occur.

3.1.2 Modeling Pulmonary Circulation

Pulmonary circulation, similar to the systemic circulation, has been divided into three arterial ($p1$ through $p3$) and two venous ($l1$ and $l2$) groups as follows:

Pulmonary arterial groups:

1. First group: From C_{p1} to C_{p2}

$$\dot{Q}_{p1} = \frac{1}{L_{p1}} \cdot (P_{p1} - P_{p2}) - \frac{R_{p1}}{L_{p1}} \cdot Q_{p1} \tag{3.18}$$

$$\dot{V}_{p1} = Q_{rv} - Q_{p1} \tag{3.19}$$

$$P_{p1} = \frac{1}{C_{p1}} \cdot (V_{p1} - V_{un,p1}) \tag{3.20}$$

2. Second group: From C_{p2} to C_{p3}

$$Q_{p2} = \frac{1}{R_{p2}} \cdot (P_{p2} - P_{p3}) \tag{3.21}$$

$$\dot{V}_{p2} = Q_{p1} - Q_{p2} \tag{3.22}$$

$$P_{p2} = \frac{1}{C_{p2}} \cdot (V_{p2} - V_{un,p2}) \tag{3.23}$$

3. Third group: From C_{p3} to C_{l1}

$$Q_{p3} = \frac{1}{R_{p3}} \cdot (P_{p3} - P_{l1}) \tag{3.24}$$

$$\dot{V}_{p3} = Q_{p2} - Q_{p3} \tag{3.25}$$

$$P_{p3} = \frac{1}{C_{p3}} \cdot (V_{p3} - V_{un,p3}) \tag{3.26}$$

Pulmonary venous groups:

1. First group: From C_{l1} to C_{l2}

$$Q_{l1} = \frac{1}{R_{l1}} \cdot (P_{l1} - P_{l2}) \tag{3.27}$$

$$\dot{V}_{l1} = Q_{p3} - Q_{l1} \tag{3.28}$$

$$P_{l1} = \frac{1}{C_{l1}} \cdot (V_{l1} - V_{un,l1}) \tag{3.29}$$

2. Second group: From C_{l2} to C_{la}

$$\dot{Q}_{l2} = \frac{1}{L_{l2}} \cdot (P_{l2} - P_{la}) - \frac{R_{l2}}{L_{l2}} \cdot Q_{l2} \tag{3.30}$$

$$\dot{V}_{l2} = Q_{l1} - Q_{l2} \tag{3.31}$$

$$P_{l2} = \frac{1}{C_{l2}} \cdot (V_{l2} - V_{un,l2}) \tag{3.32}$$

3.1.3 Modeling Coronary Circulation

Ordinary differential equations were used to acquire a mathematical model for the coronary circulatory system with two variable resistances and a constant capacitance.

In the body, the balance between myocardial oxygen demand and supply is mainly controlled via coronary vasodilation [3]. Accordingly, a first resistor (R_{c1}) was used to model the coronary arterial resistance, through which the amount of coronary blood flow (CBF) was controlled so as to match the coronary oxygen demand, which itself is linearly proportional to PVA (Equation 2.13). Therefore, R_{c1} can be defined as a function of PVA and the average coronary capillary blood flow per cardiac cycle ($Q_{c2,avg}$), which delivers the necessary oxygen to the left ventricular muscle:

$$R_{c1} = f(Q_{c2,avg}, PVA) \tag{3.33}$$

This relationship will be developed further in Section 3.4.

A second resistor (R_{c2}) was used to model the resistance of coronary capillary vasculature (capillary and venous, lumped together). Guyton and Hall (2006) describe the compression of the coronary capillaries caused by the left ventricular systole and diastole as "Capillary blood flow in the left ventricle muscle falls to a low value during

systole. The reason for this is strong compression of the left ventricular muscle around the intramuscular vessels during systolic contraction. During diastole, the cardiac muscle relaxes and no longer obstructs blood flow through the left ventricular muscle capillaries, so that blood flows rapidly during all of diastole." Therefore, it is possible to neglect the compression effects on the coronary arteries and relate the value of the combined coronary capillary and venous resistance (R_{c2}) as a fraction of left ventricular pressure (P_{lv}) as follows:

$$R_{c2} = K_{c2} \cdot P_{lv} \tag{3.34}$$

As the coronary vessels are compressible by intramuscular pressure (P_{im}) caused by the left ventricular pressure (P_{lv}), this relationship was modeled as:

$$P_{im} = K_{im} \cdot P_{lv} \tag{3.35}$$

Coronary circulation is represented by:

$$Q_{c1} = \frac{1}{R_{c1}} \cdot (P_{as} - P_{cor}) \tag{3.36}$$

$$Q_{c2} = \frac{1}{R_{c2}} \cdot (P_{cor} - P_{ra}) \tag{3.37}$$

$$\dot{V}_c = Q_{c1} - Q_{c2} \tag{3.38}$$

$$P_c = \frac{1}{C_c} \cdot (V_c - V_{un,c}) \tag{3.39}$$

where the constant capacitor (C_c) models the capacitance of the whole coronary vascular system, and P_c gives the pressure in the coronary vessels due to the volume of the blood within. The total pressure in the coronary vasculature (P_{cor}) is the sum of the pressures P_c and P_{im} as follows:

$$P_{cor} = P_c + P_{im} \tag{3.40}$$

3.2 Modeling Cardiac Chambers

Pumping work is performed by the ventricles, which, therefore, are modeled as variable elastance chambers. Atria, which are responsible for filling the ventricles, are also active chambers; however, atrial active state may be neglected for simplicity and the atria can be modeled as passive compliance chambers. Both the left and the right side of the heart were modeled as an electrical circuit, where capacitors represent the chambers, ideal diodes represent the valves, inertial effects and viscous properties of blood are modeled as inductances and resistances, respectively.

The equations used for modeling the left and right sides of the heart are given in the sections below. The methods used in the generation of ventricular pressures (P_{lv} and P_{rv}) are further described in Section 3.3. Parameters used in these equations are given in Appendix A and Simulink block diagrams are given in Appendix B.

3.2.1 Modeling the Left Heart

The left heart is divided into the left atrium and ventricle (subscripts la and lv, respectively). Heart valves between these chambers are modeled with piecewise functions in terms of their respective flows.

1. Left atrium:

Flow from the left atrium towards the left ventricle, Q_{la}, is controlled by the state of the MV:

$$\dot{Q}_{la} = \begin{cases} \frac{1}{L_{la}} \cdot (P_{la} - P_{lv}) - \frac{R_{la}}{L_{la}} \cdot Q_{la} & \text{if MV open} \\ 0 & \text{if MV closed} \end{cases} \tag{3.41}$$

where the generation of left ventricular pressure, P_{lv}, is defined in Section 3.3.

The equations for left atrial volume (V_{la}) and pressure (P_{la}) are:

$$\dot{V}_{la} = Q_{l2} - Q_{la} \tag{3.42}$$

$$P_{la} = \frac{1}{C_{la}} \cdot (V_{la} - V_{un,la}) \tag{3.43}$$

respectively.

2. Left ventricle:

Flow from the left ventricle towards the aorta, Q_{lv}, is controlled by the state of the AV:

$$\dot{Q}_{lv} = \begin{cases} \frac{1}{L_{lv}} \cdot (P_{lv} - P_{as}) & \text{if AV open} \\ 0 & \text{if AV closed} \end{cases} \tag{3.44}$$

where the aortic root pressure, P_{as}, is defined as:

$$P_{as} = R_{0s} \cdot Q_{ao} + P_{a1} \tag{3.45}$$

The equation for left ventricular volume, V_{lv}, is given by:

$$\dot{V}_{lv} = Q_{la} - Q_{lv} \tag{3.46}$$

3.2.2 Modeling the Right Heart

Similar to the left heart, the right heart is divided into the right atrium and ventricle (subscripts ra and rv, respectively) and the heart valves are modeled with piecewise functions in terms of their respective flows.

1. Right atrium:

Flow from the right atrium towards the right ventricle, Q_{ra}, is controlled by the state of the TV:

$$\dot{Q}_{ra} = \begin{cases} \dfrac{1}{L_{ra}} \cdot (P_{ra} - P_{rv}) - \dfrac{R_{ra}}{L_{ra}} \cdot Q_{ra} & \text{if TV open} \\ 0 & \text{if TV closed} \end{cases} \tag{3.47}$$

where the generation of right ventricular pressure, P_{rv}, is defined in Section 3.3.

Right atrial volume (V_{ra}) and pressure (P_{ra}) are given as:

$$\dot{V}_{ra} = Q_{v2} - Q_{ra} + Q_{c2} \tag{3.48}$$

$$P_{ra} = \frac{1}{C_{ra}} \cdot (V_{ra} - V_{un,ra}) \tag{3.49}$$

respectively.

2. Right ventricle:

Flow from the right ventricle towards the pulmonary arteries, Q_{rv}, is controlled by the state of the PV:

$$\dot{Q}_{rv} = \begin{cases} \frac{1}{L_{rv}} \cdot (P_{rv} - P_{ap}) & \text{if PV open} \\ 0 & \text{if PV closed} \end{cases} \tag{3.50}$$

where the pulmonary arterial root pressure, P_{ap}, is defined as:

$$P_{ap} = R_{0p} \cdot Q_{rv} + P_{p1} \tag{3.51}$$

The equation for right ventricular volume, V_{rv}, is given by:

$$\dot{V}_{rv} = Q_{ra} - Q_{rv} \tag{3.52}$$

3.3 Ventricular Pressure Generation and Control of the Cardiovascular Simulation System

After having developed the dynamic equations of the analogous electrical circuit, the methods to generate left and right ventricular pressures, and to control the cardiovascular model will be explained in the following sections. Ventricular pressures will be generated by combining active and passive properties of the heart muscle, while the model will be controlled with a simple on-off signal. The section will conclude with a description of how the two methods are interrelated; or, in other words, how the generation of left and right ventricular elastances constitutes the basis for the derivation of the control law, which drives the whole system.

3.3.1 Ventricular Pressure Generation

The myocardial mechanism that generates tension was described by Sonnenblick (1965) [22] using the instantaneous length-velocity-tension relationship obtained from afterloaded isotonic contraction experiments on isolated cat papillary muscles pre-stretched with different preloads Figure 3-3.

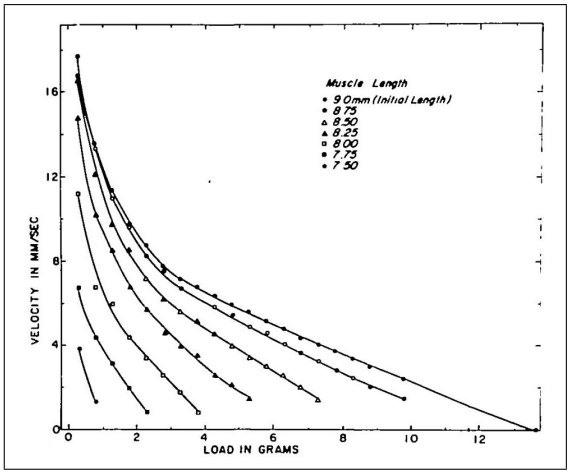

Figure 3.3 Tension-velocity relationship of cat papillary muscle [22]

In Figure 3.3, each curve represents the velocity of shortening of the muscle stretched at the same preload, PL (0.30 g > PL > not given in Sonnenblick, 1965) to the same length, l_p (9.00 mm > l_p > 7.50 mm). Different points on each curve correspond to different afterloads, AL, added at 2.00 g increments to the preload. Projecting each point to the ordinate and to the abscissa gives, respectively, the peak attained velocity (ϑ) during a contraction and the total load (PL + AL), against which that specific contraction occurs. Extrapolation to the abscissa ($\vartheta = 0$) of the curves corresponding to each PL (i.e. for each l_p) gives the isometric tension, T_{max}, for that l_p. On the other hand, extrapolation of each curve to the ordinate (PL + AL = 0) gives the maximum theoretical velocity of shortening, ϑ_{max}, for that l_p. This velocity is theoretical because it assumes that PL is also zero, which entails that the muscle is weightless. Clearly, this interpretation of Figure 3.3 relates l_p (i.e. PL), T_{max} and ϑ_{max} together, such that the abscissa and ordinate intercepts of each curve are T_{max} and ϑ_{max} for that l_p, respectively.

In this thesis, a novel approach was suggested for the calculation of myocardial wall tension utilizing a normalized version of this tension-velocity relationship as follows:

$$T_n = \frac{T_{max} - T}{T_{max}} \tag{3.53}$$

$$\vartheta_n = \frac{\vartheta_{max} - \vartheta}{\vartheta_{max}} \tag{3.54}$$

where T is the total tension of any point on any curve and T_n is the normalized tension. Similarly, ϑ is the velocity of any point on any curve and ϑ_n is the normalized velocity.

Extracting data from Figure 3.3, $\vartheta - T$ relationships corresponding to each l_p curve were expressed analytically (Appendix C):

$$\vartheta = \lambda_1 \cdot e^{-\kappa_1 \cdot T} + \lambda_2 \cdot e^{-\kappa_2 \cdot T} - \lambda_3 \tag{3.55}$$

The coefficients in Equation 3.55 are given in Table 3-1. Also shown in the same Table are the T_{max} and ϑ_{max} (abscissa and ordinate intercepts, respectively) calculated for each l_p curve.

Table 3.1
Coefficients, T_{max} and ϑ_{max} of fitted tension-velocity curves to the data of Sonnenblick, 1965 [22] for cardiac muscle for each l_p

l_p [mm]	λ_1	λ_2	λ_3	κ_1	κ_2	T_{max} [g]	ϑ_{max} [mm/s]	R^2
9.00	11.61	36.28	26.78	1.090	$22.30 \cdot 10^{-3}$	13.60	21.11	0.99
8.75	10.62	28.78	18.92	1.012	$33.42 \cdot 10^{-3}$	12.55	20.48	0.99
8.50	11.01	39.80	30.80	1.315	$29.79 \cdot 10^{-3}$	8.61	20.01	0.99
8.25	14.95	8.70	4.53	0.190	$2.42 \cdot 10^{-3}$	6.28	19.12	0.99
8.00	7.86	40.08	32.49	2.059	$48.02 \cdot 10^{-3}$	4.37	15.45	0.99

Calculated T_{max} and ϑ_{max} values were used to calculate the normalized values of tension and velocity from Equation 3.53 and Equation 3.54. These were plotted against each other (Figure 3.4) and pairs of data were fitted to a cubic parabola (R^2 = 0.98, Appendix C):

$$T_n = 1 - \vartheta_n^3 \tag{3.56}$$

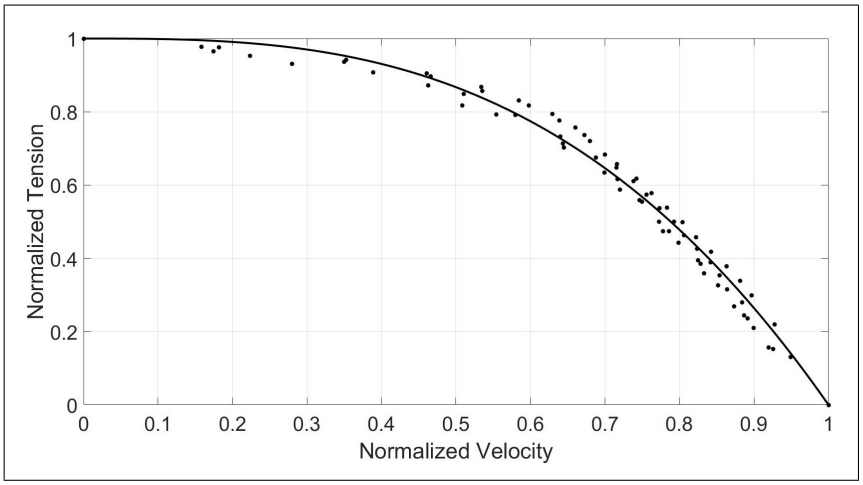

Figure 3.4 Normalized tension-velocity curve fitting

Substituting Equation 3.53 and Equation 3.54 in Equation 3.56 and rearranging, T was expressed as a function of ϑ, ϑ_{max}, and T_{max}:

$$T = T_{max} \cdot (1 - \frac{\vartheta}{\vartheta_{max}})^3 \tag{3.57}$$

It should be noted that, up to this point, the effect of time has not been taken into consideration. In order to use Equation 3.57 for calculating instantaneous tension, instantaneous length-dependent representations of ϑ_{max}, and T_{max} are needed. This task was realized by first converting length data of Figure 3.3 to strain data (ϵ). In order the calculate strain, the length (l_p = 9.00 mm) of the muscle fiber at the heaviest preload (PL = 3.00 g) was taken as the initial length, l_{ini}.

$$\epsilon = \frac{l_{ini} - l_p}{l_{ini}} \tag{3.58}$$

and T_{max} was plotted against the corresponding strain values. Assuming that the cross-section of the muscle was 1.40 mm^2 as given by Sonnenblick, 1965 [22] and tension values (T_{max} in grams) were converted to stress in mmHg (Figure 3.5) and fitted into ($R^2 = 0.97$):

$$T_{max} = -4678 \cdot \epsilon + 737.1 \tag{3.59}$$

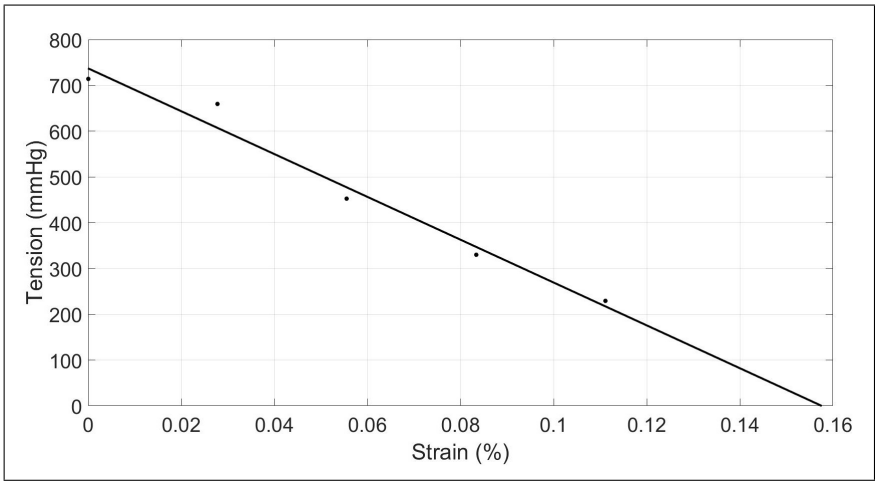

Figure 3.5 Tension (stress)-strain relationship derived for muscle using Equation 3.58

From Figure 3.5, it can be seen that abscissa intercept ($T_{max} = 0$) of the fitted line corresponds to a strain of $\epsilon_0 = 15.70\%$ on the muscle. At this point, the task was to convert data obtained for the muscle (macro-scale) into corresponding data for the sarcomere (micro-sacle). This necessitates the critical step of assuming individual myocardial sarcomeres to have an isotropic cross-sectional structure and a uniform distribution within the myocardium, exhibiting all macro-scale muscular properties in the micro-scale (Figure 3.6).

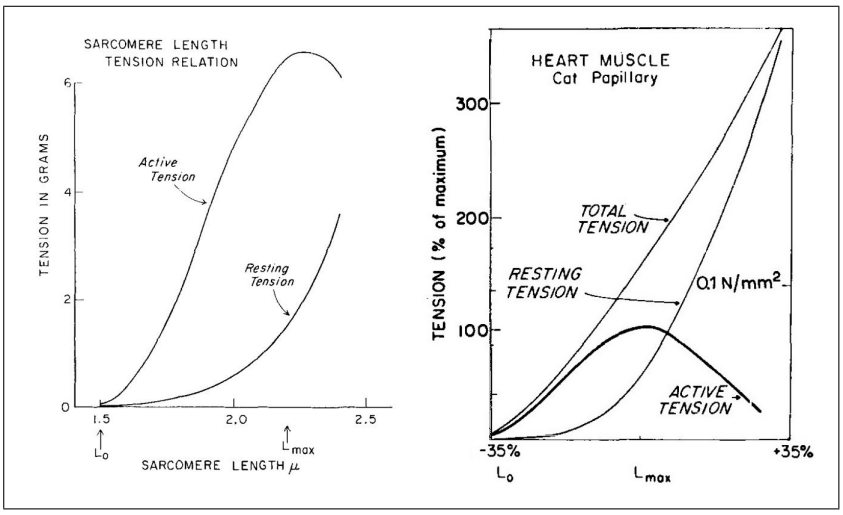

Figure 3.6 Length-tension relationships of (right) myocardial sarcomere [17] and (left) cat papillary muscle [56]

This assumption allows for substituting sarcomere lengths (in μm), l_s and l_0, for muscle lengths (in mm), l_p and l_{ini}, respectively. Rearranging Equation 3.58:

$$l_0 = \frac{l_s}{1 - \epsilon} \tag{3.60}$$

It is known that, for myocardial sarcomeres, zero-tension corresponds to a sarcomere length of $l_{s,0} = 1.65$ μm [57]. Substituting ϵ_0 from Figure 3.5 and $l_{s,0}$ into Equation 3.60, l_0 was found as 1.95 μm. Using this value of l_0 as a constant, sarcomere lengths, l_s, at the different strain levels seen in Figure 3.5 were calculated from Equation 3.60 (Figure 3.7), and fitted into a cubic polynomial relationship ($R^2 = 0.93$):

$$T_{max}(l_s) = 826 \cdot l_s^3 - 7310.1 \cdot l_s^2 + 20517.8 \cdot l_s - 17663.2 \tag{3.61}$$

where minimum and maximum zero-tension lengths of sarcomere were assumed as 1.65 μm [57] and 3.60 μm (same as skeletal muscle) [58], respectively, and the maximum tension length, where the slope is zero, taken as 2.30 μm [19]. Notice that the abscissa intercept of the fitted line corresponds to a sarcomere length of 1.65 μm, in accordance with [57].

Equation 3.61 was further modified to allow accounting for the effect of inotropic state by multiplying with a coefficient of isometric contraction, β_T:

$$T_{max}(l_s) = \beta_T \cdot (826 \cdot l_s^3 - 7310.1 \cdot l_s^2 + 20517.8 \cdot l_s - 17663.2) \tag{3.62}$$

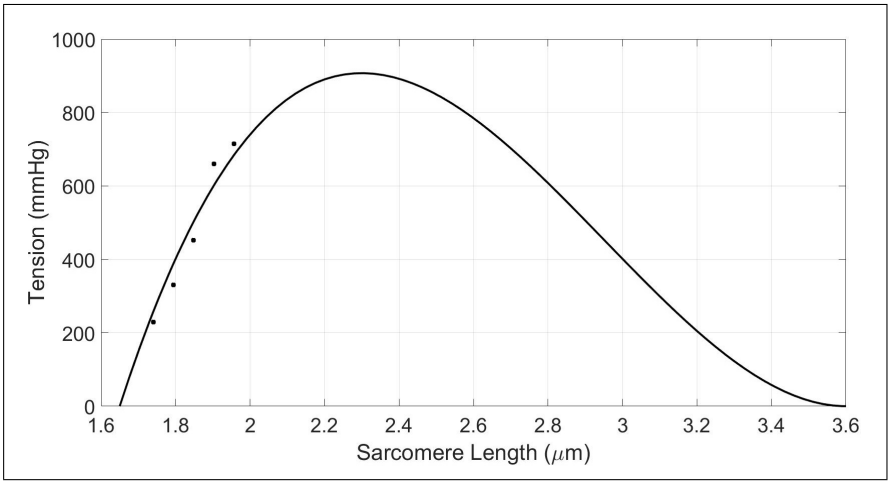

Figure 3.7 Maximum tension-sarcomere length relationship converted from maximum tension-muscle length of Figure 3.3

After obtaining the $T_{max} - l_s$ relationship as shown in Equation 3.62, the next step was to establish the $\vartheta_{max} - l_s$ relationship from the $\vartheta_{max} - l_p$ relationship given in Table 3.1. Assuming that the muscle is made up of parallel strings of sarcomeres in series, velocity of individual sarcomeres (uniformly distributed within a string) were added to calculate muscle velocity (same for each string of sarcomeres) and tension generated by each string is accepted as muscle tension. The number of sarcomeres in a string, calculated by dividing initial muscle length, l_{ini}, into initial sarcomere length, l_0, was used to determine sarcomere shortening velocity, $\vartheta_{max,sarc}$, from the $\vartheta_{max,muscle}$.

$$\vartheta_{max,sarc} = \frac{l_{ini}}{l_0} \cdot \vartheta_{max,muscle} \tag{3.63}$$

$$\vartheta_{max,sarc} = \frac{9.00[mm]}{1.95[\mu m]} \cdot \vartheta_{max,muscle} \tag{3.64}$$

Using Equation 3.64, $\vartheta_{max,muscle}$ values for each l_p from Table 3.1 were converted to $\vartheta_{max,sarc}$ values for each l_s. Next, using $l_0 = 1.95$ μm in Equation 3.60 as before, l_s values corresponding to each strain level of Figure 3.7 was calculated. Finally, $\vartheta_{max,sarc} - ls$ pairs were fitted into ($R^2 = 0.99$):

$$\vartheta_{max}(l_s) = 15.5 \cdot \left[1 - e^{-18.4 \cdot (l_s - 1.6)}\right] - 11 \tag{3.65}$$

Similar to the modification of $T_{max}(l_s)$ (Equation 3.62), Equation 3.65 was modified to allow the accounting of the effect of the inotropic state by multiplying with a coefficient of isotonic contraction, β_ϑ.

$$\vartheta_{max}(l_s) = \beta_\vartheta (15.5 \cdot \left[1 - e^{-18.4 \cdot (l_s - 1.6)}\right] - 11) \tag{3.66}$$

Substituting Equation 3.62 and Equation 3.66 into Equation 3.57, the active sarcomere/muscle tension, T_{act}, was expressed as a function of sarcomere length (l_s) and velocity (ϑ_s):

$$\begin{aligned} T_{act}(l_s, \vartheta_s) =& \beta_T \cdot (826 \cdot l_s^3 - 7310.1 \cdot l_s^2 + 20517.8 \cdot l_s - 17663.2) \\ & \cdot \left(1 - \frac{\vartheta_s}{\beta_\vartheta \cdot \left\{15.5 \cdot \left[1 - e^{-18.4 \cdot (l_s - 1.6)}\right] - 11\right\}}\right)^3 \end{aligned} \tag{3.67}$$

As mentioned above, the use of β_ϑ and β_T allowed for modifying the slope of the $T_{max}(l_s)$ and $\vartheta_{max}(l_s)$ functions, therefore, accounting for changes in inotropic state for isometric and isotonic contractions, simultaneously. On the other hand, expressing the tension as a function of l_s and ϑ_s allowed modeling the ejection phase in terms of the auxotonic contraction of the sarcomere. At this point, a final task remained: That of expressing the $T - l_s - \vartheta_s$ relationship as a dynamic process, i.e. the task of introducing time into Equation 3.67. This was accomplished simply by substituting $\dot{l}_s$ for ϑ_s, instantaneous shortening velocity of the sarcomere.

Here, it should be noted that total myocardial wall tension is a combination of active and passive tensions (T_{act} and T_{pass}, respectively). Therefore, in addition to the T_{act}, T_{pass} must be accounted for.

Passive (resting) tension was determined from the elastic (diastolic) myocardial data of Siegel, 1963 [16], shown in Figure 3.8, which were fitted into a curve ($R^2 = 0.90$):

$$T_{pass}(l_s) = 1.50 \cdot \left[e^{0.13 \cdot (l_s - 1.80)} - 1\right] \cdot e^{3.30 \cdot l_s} \tag{3.68}$$

where the zero-tension (initial) length, 14.0 mm, and the peak active tension length, 19.6 mm, of the muscle data were linearly mapped to 1.65 μm and 2.30 μm, respectively; and tension values in grams were converted into mmHg assuming cross-section of muscle to be 0.3848 mm^2 [16].

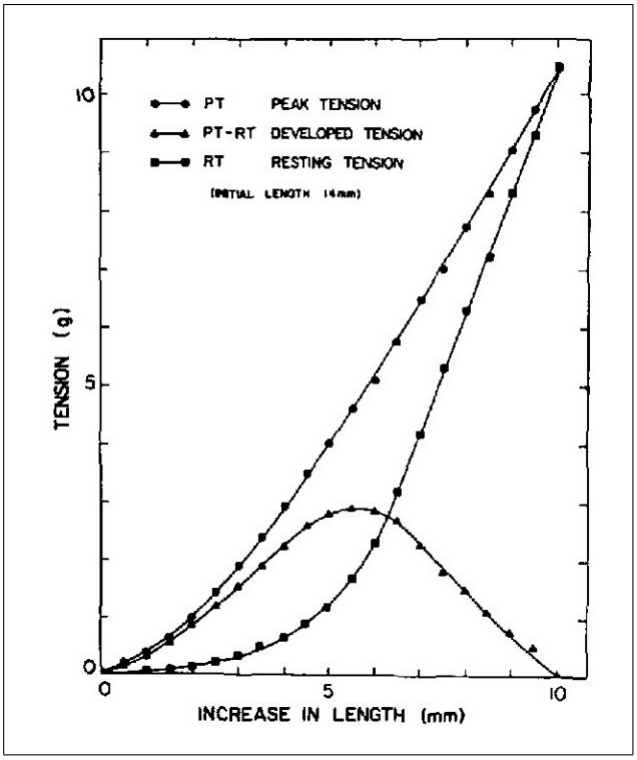

Figure 3.8 Total (peak), active (developed) and passive (resting) length-tension relationships of a cat papillary muscle [16]

In order to allow manipulation of the passive ventricular (both LV and RV) stiffnesses and determine myocardial diastolic behavior, Equation 3.68 was modified by scaling with a passive biomechanical coefficient, ξ_P:

$$T_{pass}(l_s) = \xi_P \cdot 1.50 \cdot \left[e^{0.13\cdot(l_s-1.80)} - 1\right] \cdot e^{3.30\cdot l_s} \tag{3.69}$$

As previously mentioned, the input and output of the plant are instantaneous ventricular pressure and volume, respectively (Figure 3.2). Since the next natural step in the methodology was to apply Equation 3.67 and Equation 3.69, derived specifically for the sarcomere, to generate ventricular pressure-volume relationship, instantaneous sarcomere length had to be obtained from instantaneous ventricular volume on the plant's output side, while instantaneous ventricular pressure had to be generated from instantaneous sarcomere tension on the plant's input side (Figure 3.9).

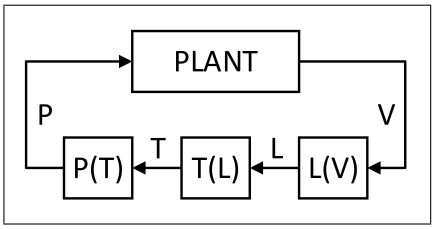

Figure 3.9 Block Diagram of the System with Semi-Expanded Actuator Block

To relate sarcomere length, l_s [μm], to ventricular volume, V [ml], data in Figure 3.10 were used, assuming that EDV at 10 mmHg is 140 ml [59]; and the relationship was obtained as ($R^2 = 0.97$):

$$l_s = 0.95 \cdot (V + 18)^{0.165} \tag{3.70}$$

Here, the real (volume axis intercept of the P_{max} curve) zero-pressure volume of the ventricle was shifted from 10 ml, estimated for the canine ventricle in Figure 3.10 [18], to 27 ml for the human ventricle [60] resulting with:

$$l_s = 0.95 \cdot (V + 1)^{0.165} \tag{3.71}$$

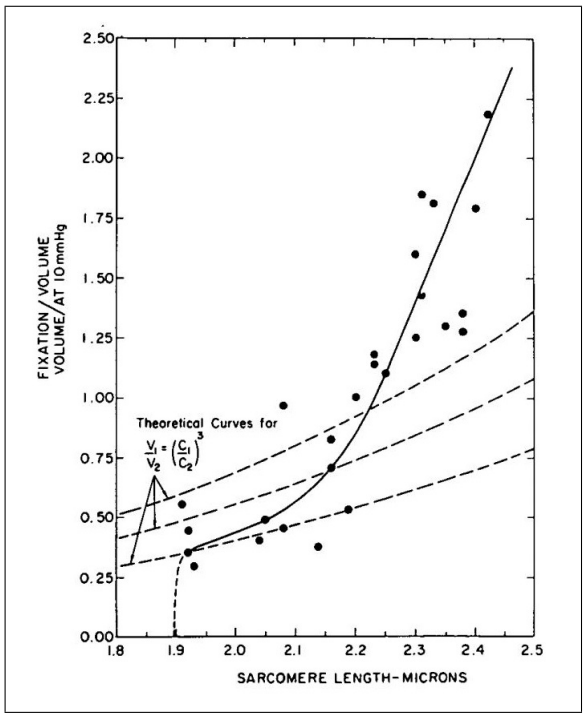

Figure 3.10 Relationship between myocardial sarcomere length and normalized ventricular fixation volume w.r.t. the volume at 10 mmHg for canine left ventricle [18]

The final piece of the puzzle was put into place by converting active and passive tensions, T_{act} and T_{pass} [mmHg], respectively, of the sarcomeres into active and passive pressures, P_{act} and P_{pass} [mmHg], respectively, of the ventricle. The relation between ventricular active/passive pressure, P, and myocardial active/passive wall tension, T, was defined as:

$$P = \alpha \cdot T \tag{3.72}$$

where, α is the tension-pressure conversion coefficient, which was chosen, by trial and error, as 1 for left ventricle and 1/3 for right ventricle; assuming the ratio between right and left ventricular peak systolic pressures is 1/3 (40 mmHg / 120 mmHg) [61, 3].

Plugging the chosen values of α in Equation 3.72, both active and passive LV/RV pressures could be determined for use as input to the plant.

3.3.2 Control of the Cardiovascular Simulation System

Control of the plant was accomplished primarily by the binary activation signal "u", which was imposed on the active (auxotonic and isometric) and passive biomechanical properties of the myocardium. All parameters used in the equations below are given in the Appendix D. Simulink block diagrams of this section are given in Appendix B.

All time dependence in the following equations was defined as the modulus of simulation clock, t, and 60/HR:

$$t_{mod}(t) = \mod\left(t, \frac{60}{HR}\right) \tag{3.73}$$

The switch between myocardial activation and deactivation states was modeled with the binary activation signal "u" as follows (Figure 3.11):

$$u(t_{mod}) = \begin{cases} 1 & \text{if } 0 \leq t_{mod} \leq t_{rb} \\ 0 & \text{otherwise} \end{cases} \tag{3.74}$$

where t_{rb} marks the time when ventricular relaxation begins. Clearly, t_{rb} determines the width of the square wave "u" and, as such, serves as the main control input to the system. The reasons for using t_{rb} as a control signal are both its availability through in-vivo ECG data and the above-explained biomechanical definition of activation.

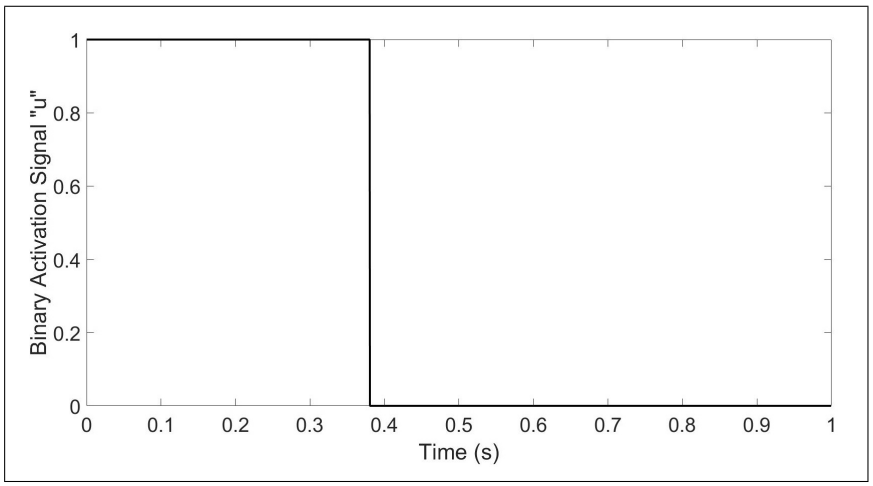

Figure 3.11 Binary Activation Signal "u"

Changes between active and passive states cannot be modeled as logical case switches due to the conduction delays in action potential propagation across myocardial syncytium, as well as to the inertial effects opposing the contraction of activated myocardium. Therefore, an intermediate control signal "a" was used to define the volumetric percentage of the contracting myocardium. This control signal, "a" was represented by dual Gaussian Functions with a fast rise during activation and a slow fall during deactivation, with respective time constants τ_c and τ_r, such that $\tau_c < \tau_r$ (Figure 3.12):

$$a(t_{mod}, u) = u \cdot \left(1 - e^{-\frac{t_{mod}^2}{\tau_c}}\right) + (1 - u) \cdot e^{-\frac{(t_{mod} - t_{rb})^2}{\tau_r}} \tag{3.75}$$

where the values for τ_c and τ_r were calibrated using IVC $\approx$ 30 ms and IVR $\approx$ 60 ms durations, respectively [3].

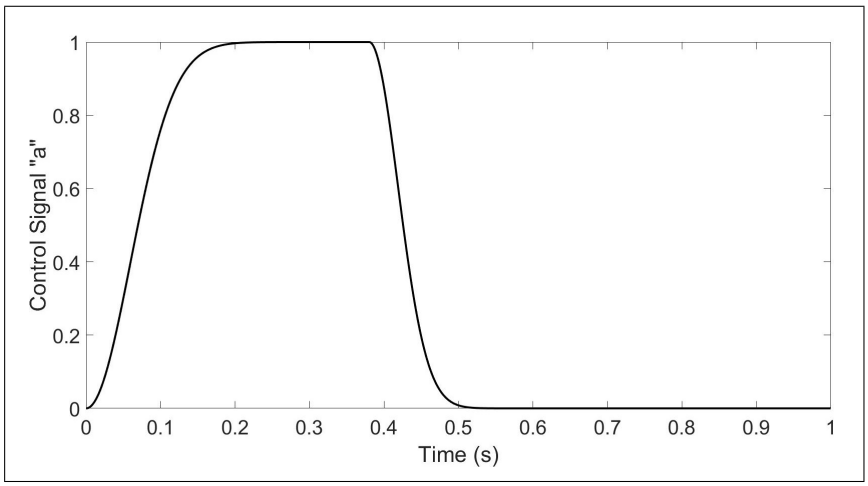

Figure 3.12 Control Signal "a"

The use of "a" allowed not only the resolution of the different states of myocardial activation into isometric and auxotonic modes, but also led to a definition of the ventricular pressure as:

$$P = a \cdot P_{act} + (1 - a) \cdot P_{pass} \tag{3.76}$$

The Actuator block in Figure 3.2 can, therefore, be expanded to show the processing of the data in more detail as given in Figure 3.13.

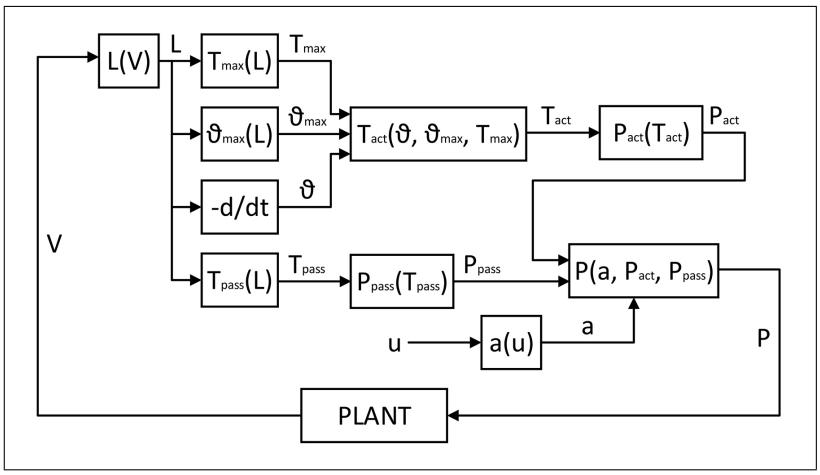

Figure 3.13 Block Diagram of the System with Fully-Expanded Actuator Block

3.4 Energy Balance of the Heart and Coronary Blood Flow Control

In this thesis only the left ventricular oxygen supply and demand relationship was studied because LV has a significantly larger share of the oxygen consumption in the heart [62]. The oxygen demand (D_{O2}) equation for human LV was obtained from Equation 2.13 assuming a normal human left ventricle mass of M = 200 g [60]:

$$D_{O2}\left[\frac{mlO_2}{beat}\right] = 3 \cdot 10^{-5}\left[\frac{mlO_2}{mmHg \cdot ml}\right] \cdot PVA\left[\frac{mmHg \cdot ml}{beat}\right] + 0.048\left[\frac{mlO_2}{beat}\right] \quad (3.77)$$

To find the oxygen supply (S_{O2}) to the left ventricle, average coronary capillary flow per cardiac cycle ($Q_{c2,avg}$) and HR were used:

$$\begin{aligned} S_{O2}\left[\frac{mlO_2}{beat}\right] =& Q_{c2,avg}\left[\frac{mlBlood}{sec}\right] \cdot \left[\frac{dlBlood}{100mlBlood}\right] \cdot HR^{-1}\left[\frac{beat}{min}\right]^{-1} \cdot \left[\frac{60sec}{min}\right] \\ & \cdot CAV_{O2}\left[\frac{mlO_2}{dlBlood}\right] \end{aligned} \quad (3.78)$$

where the assumed normal human coronary arteriovenous oxygen difference, CAV_{O2} = 13 [mlO_2/dlBlood] [63]. As seen from Equation 3.77 and Equation 3.78, PVA and $Q_{c2,avg}$, directly determine D_{O2} and S_{O2}, respectively, when HR and CAV_{O2} are constant. The per-beat oxygen deficit, ε, was defined as:

$$\varepsilon = D_{O2} - S_{O2} + bias \quad (3.79)$$

Here, the bias term, which was added to account for a positive coronary flow reserve, was accepted as 0.1 (approximately 30% S_{O2}, per [3]).

The variable coronary arterial resistance, R_{c1}, was previously defined as a function of PVA and $Q_{c2,avg}$ in Section 3.1.3.

A discrete proportional controller was designed to adjust the value of coronary arterial resistance, $R_{c1}[n]$, on a beat-per-beat basis. The controller first amplifies the current error, $\varepsilon[n]$, by a proportionality coefficient, K_P, and calculates the currently needed correction in coronary arterial resistance, $\Delta R_{c1}[n]$. At the same time, all calculated ΔR_{c1} values, from cycle $m = 1$ through cycle $m = n$, are accumulated as $\sum \Delta R_{c1} = \sum_{m=1}^{n} K_P \cdot \varepsilon[m]$. Here, m is used as a dummy variable varying between 1 and n. Finally, the initial value of the coronary arterial resistance, $R_{c1}[0]$ is added to $\sum \Delta R_{c1}$, such that:

$$R_{c1}[n+1] = R_{c1}[0] + \sum_{m=1}^{n} K_P \cdot \varepsilon[m] \tag{3.80}$$

In order to overcome abrupt peaks/falls in $\sum \Delta R_{c1}$ and to limit the total change in R_{c1}, a saturation function, sat, was used, which is defined as follows:

$$\mathrm{sat}_x^y(z) = \begin{cases} x & \text{if } z \leq x \\ y & \text{if } z \geq y \\ z & \text{otherwise} \end{cases} \tag{3.81}$$

such that Equation 3.80 could now be expressed as:

$$R_{c1}[n+1] = R_{c1}[0] + \mathrm{sat}_{-20}^{20}\Big\{ \sum_{m=1}^{n} \mathrm{sat}_{-10}^{10}\big(K_P \cdot \varepsilon[m]\big) \Big\} \tag{3.82}$$

It was necessary to saturate R_{c1} in order to satisfy the anatomical limitations of coronary vessels having a maximum dilation and a minimum constriction radii, respectively. The values of K_P, and the upper and lower limits of sat functions were determined by trial and error to achieve fastest settling time and minimum overshoot in the error function. Parameters used in the equations above are given in Appendix D and Simulink block diagrams are given in Appendix B.

3.5 Model Performance Estimation

State variables were defined as pressures, volumes and flows in the various compartments of the model. Using these, beat-to-beat load-dependent performance parameters were calculated as:

1. Stroke Volume (SV) [ml]:

$$SV = EDV - ESV \tag{3.83}$$

2. Cardiac Output (CO) [ml/s]:

$$CO = SV \cdot HR \tag{3.84}$$

3. Ejection Fraction (EF) [%]:

$$EF = \frac{SV}{EDV} \tag{3.85}$$

4. Stroke Work (SW) [mmHg · ml]:

$$SW = -\int_{EDV}^{ESV} P \cdot dV \tag{3.86}$$

5. Potential Energy (PE) [mmHg · ml]:

$$PE = \frac{1}{2} \cdot P_{es} \cdot (V_{es} - V_0) \tag{3.87}$$

6. Pressure-Volume Area (PVA) [mmHg · ml]:

$$PVA = SW + PE \tag{3.88}$$

7. Efficiency (η) [%]:

$$\eta = \frac{SW}{PVA} \tag{3.89}$$

Continuous load-dependent performance parameters were calculated as:

1. Mean Arterial Pressure (MAP) [mmHg]:

$$MAP = \frac{1}{3} \cdot (2 \cdot P_{lv,bs} + P_{lv,max}) \tag{3.90}$$

2. Power [mmHg · ml/s]:

$$Power = MAP \cdot CO \tag{3.91}$$

The load-independent performance parameters, time-varying ventricular elastance and power over EDV squared, were calculated for left ventricle only as:

1. Left Ventricular Time-Varying Elastance (E_{lv}) [mmHg/ml]:

$$E_{lv}(t) = \frac{P_{lv}(t)}{V_{lv}(t) - V_0} \tag{3.92}$$

2. Power Index (PI) [mmHg/ml · s]:

$$PI = \frac{Power}{EDV^2} \tag{3.93}$$

Performance of the model was evaluated in terms of the above parameters in continuous time on the Pressure-Volume (PV) plane; and, separately, as a function of EDV and systolic time (t_{rb}) for normal rest, normal exercise and failure rest conditions.

4. RESULTS

4.1 Length-Tension (Sarcomere) and Volume-Pressure (Ventricle) Relationships

Figure 4.1 presents the fitted active and passive length-tension relationships of myocardial sarcomere. Here, the coefficients β_T (Equation 3.62) and ξ_P (Equation 3.69) are set to 0.4 and 0.5, respectively; and the zero-active and -passive tension lengths are chosen as 1.65 μm and 1.80 μm, respectively. The maximum active tension length of 7 grams corresponds to a sarcomere length of 2.30 μm. The shape of the curves and the critical variable values are similar to those given in Figure 4.2 [17].

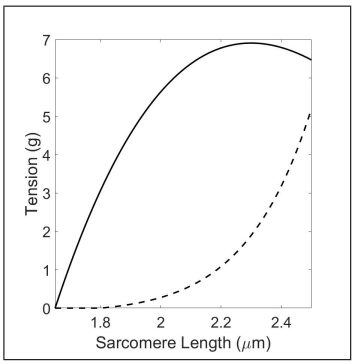

Figure 4.1 Active (solid line) and passive (dashed line) length-tension relationships of the myocardial sarcomere, as fitted in this thesis from data of Sonnenblick (1965) [22], and Siegel and Sonnenblick (1963) [16], respectively

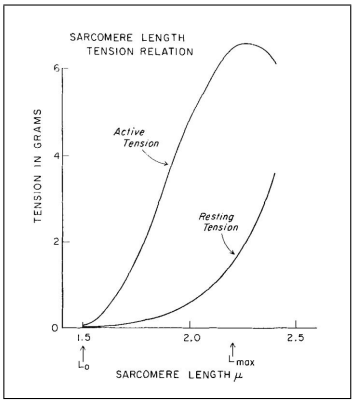

Figure 4.2 Length-tension relationships of the myocardial sarcomere [17]

The calculated maximum active (isometric) pressure, $P_{act,max}$, and passive (diastolic) pressure, P_{pass}, are shown in Figure 4.3, where β_T, ξ_P and α, in Equation 3.62, Equation 3.69 and Equation 3.72, are set to 0.6, 0.085 and 1, respectively. As indicated above, the zero-active pressure volume is set at 27 ml and the zero-passive pressure volume is set at 40 ml. At these settings, the maximum pressure of 544 mmHg is observed to occur at 200 ml, and the passive pressure is around 5-8 mmHg for 140-160 ml EDV. In Figure 4.4, a PV Loop simulated for a 10 kg dog is given for comparison, also showing the maximum active pressure and passive pressure curves, denoted with P_s and P_d, respectively [64]. The shapes of both graphs are similar with the maximum active pressure curve rising, reaching a peak and falling, and the passive pressure curve continuously increasing as the filling volume increases.

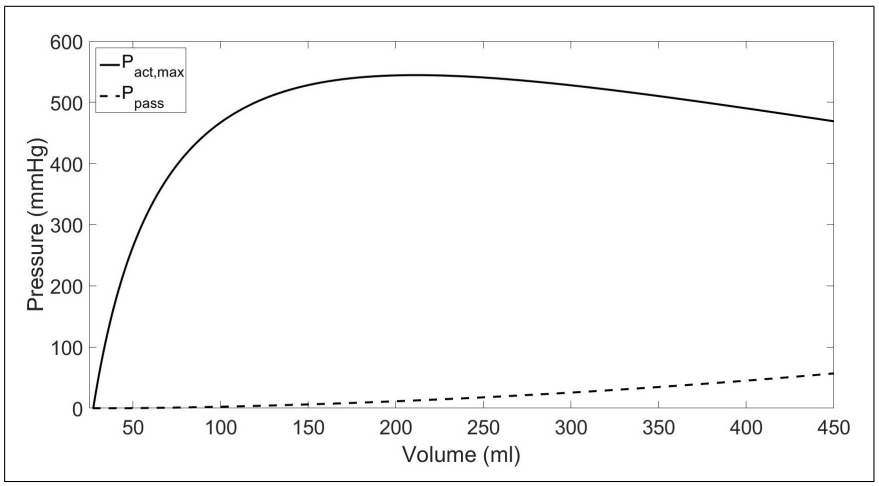

Figure 4.3 Calculated passive and maximum active (isometric) LV pressure curves as a function LV volume

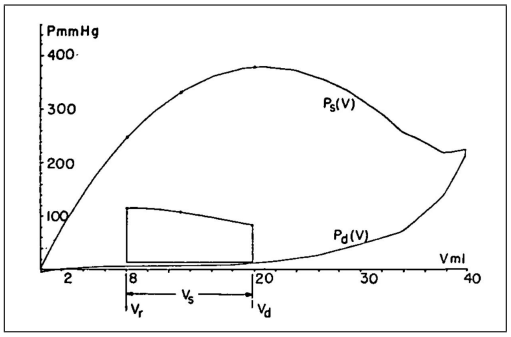

Figure 4.4 Passive, P_d, and maximum active (isometric), P_s, LV pressure curves as a function LV volume for a 10 kg dog model [64]

4.2 Time Domain Analysis of the State Variables

The time course of continuous physiological variables, which are simulated, are shown in Figure 4.5, Figure 4.8 and Figure 4.11. The tracings were obtained for normal physiological conditions at HR of 60 beat/min and t_{rb} at 0.38 seconds, for a constant total blood volume of 5158 ml, using the values for circulatory system constants (resistances, capacitances, etc.) as given in Appendix A and for control system parameters (β, τ, etc.) as given in Appendix D.

The simulated left ventricular pressure varied between systolic maximum and diastolic minimum of 120 mmHg and 77 mmHg, respectively, as shown in Figure 4.5. Peak systolic pressure occurred at 0.20 seconds after MV closure and 0.18 seconds before t_{rb}. EDV and ESV were recorded as 138 ml and 40 ml, respectively, corresponding to a SV of 90 ml and a CO of 90 ml/s (5.4 liters/min). End-diastolic pressure was found to be around 5 mmHg. A representative Wiggers diagram for normal human physiology, is given for comparison in Figure 4.6, showing similar curve shape and variable values [3].

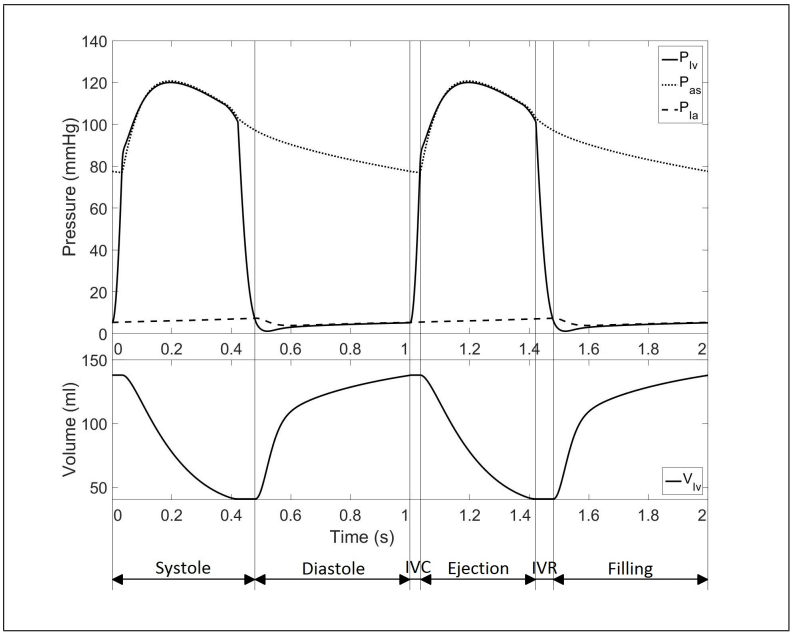

Figure 4.5 Simulation results for left ventricular pressure (P_{lv}) and volume (V_{lv}), and for aortic (P_{as}) and left atrial (P_{la}) pressures, as a function of time

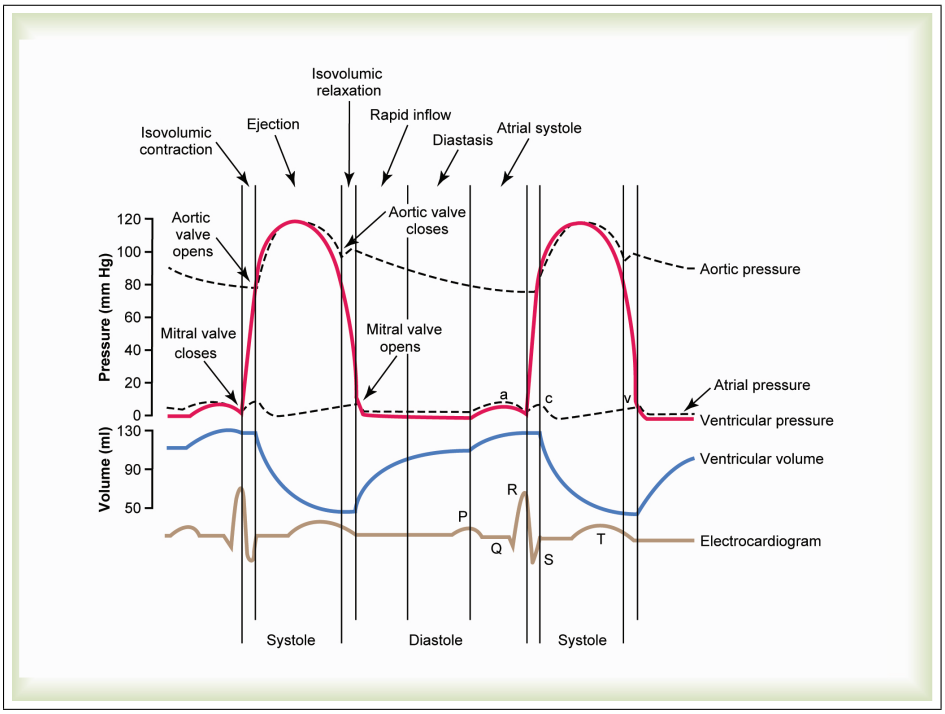

Figure 4.6 Wiggers diagram for normal human physiology [3]

Time course of volumes within the capacitances of the cardiovascular model, which are collected under four main sectional volumes of left heart ($V_{lh} = V_{la} + V_{lv}$), systemic vasculature ($V_{sv} = V_{a1}+V_{a2}+V_{a3}+V_{v1}+V_{v2}+V_c$), right heart ($V_{rh} = V_{ra}+V_{rv}$) and pulmonary vasculature ($V_{pv} = V_{p1} + V_{p2} + V_{p3} + V_{l1} + V_{l2}$), are given in Figure 4.7, beginning from their respective initial conditions (210 ml, 4308 ml, 200 ml and 440 ml, respectively) until they reach their respective steady-state values in approximately 7 seconds. The sum, V_T, of main sectional volumes at each time step remains constant at the initially set value of 5158 ml.

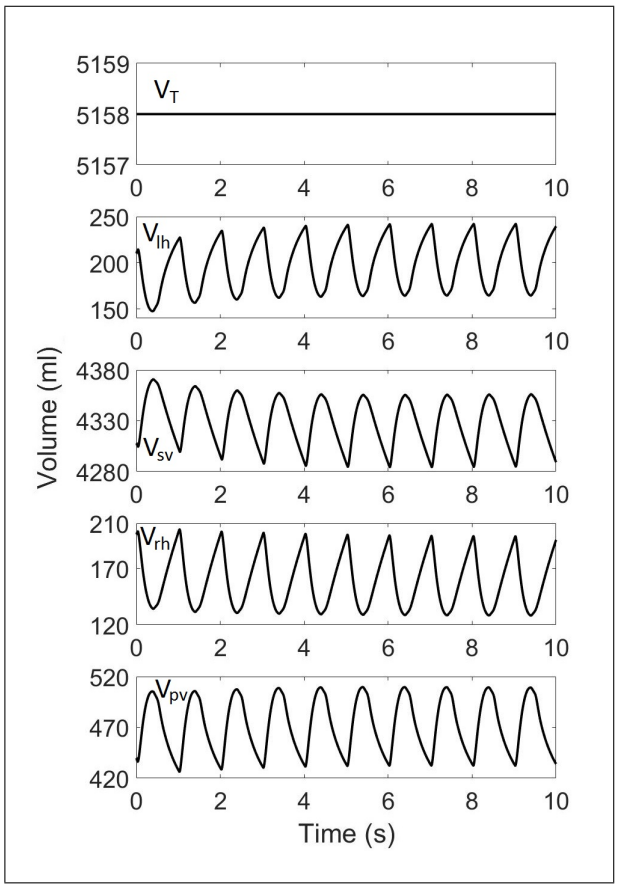

Figure 4.7 Time course of total volume (V_T), and calculated volumes within the cardiovascular sections of left heart (V_{lh}), systemic vasculature (V_{sv}), right heart (V_{rh}) and pulmonary vasculature (V_{pv})

Time-varying elastance of the simulated left ventricle (E_{lv}), under normal physiological conditions, was calculated assuming that the theoretical zero-pressure volume, V_0 = -1.5 [ml]. Absolute (Figure 4.8), and normalized to E_{max} = 2.47 [mmHg/ml] (ordinate axis) and to time to E_{max}, t_{max} = 0.4 [s] (abscissa axis) (Figure 4.9) are shown. In Figure 4.10, a normalized elastance graph plotted against normalized time for canine left ventricle is given for comparison [5]. Both normalized curves present similar trends, i.e. rising, reaching a peak, abruptly falling and settling in a plateau near zero.

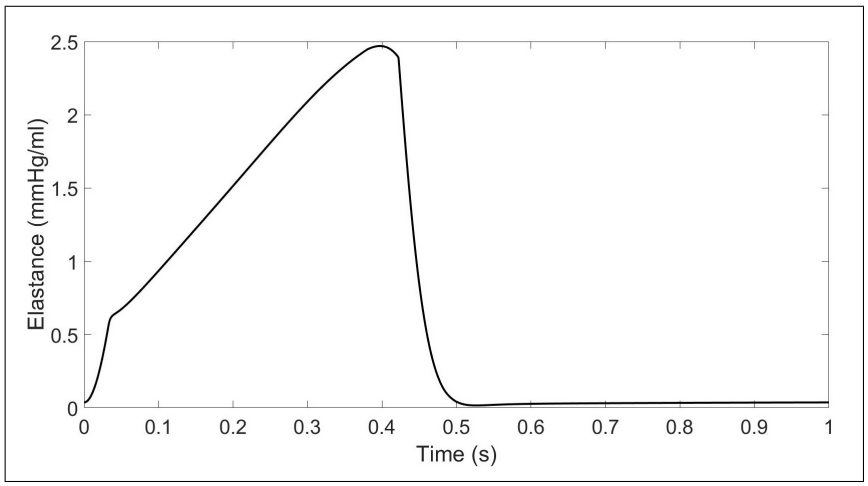

Figure 4.8 Calculated time-varying left ventricular elastance under normal physiological conditions

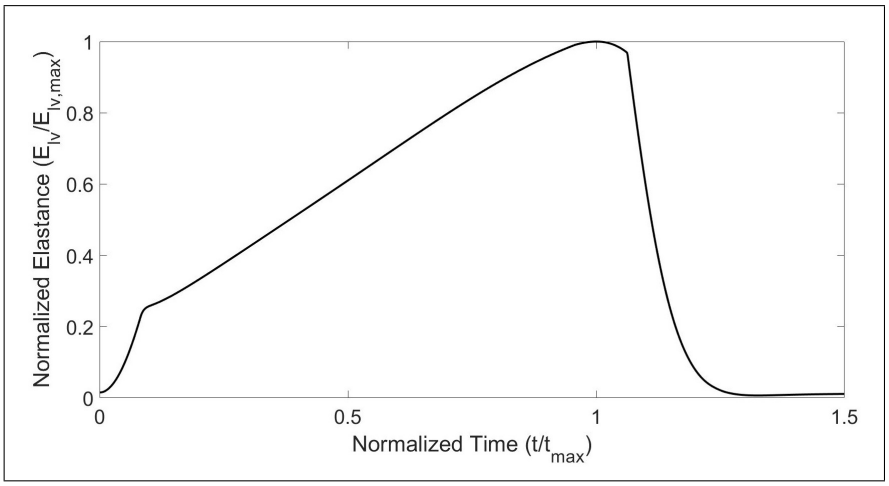

Figure 4.9 Normalized time-varying left ventricular elastance data of Figure 4.8

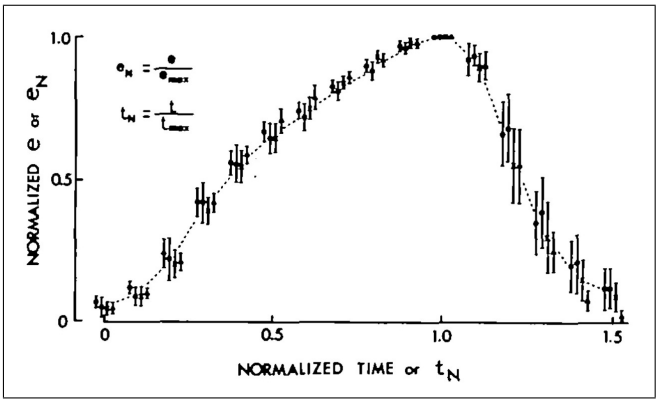

Figure 4.10 Normalized time-varying elastance graph of canine left ventricle [5]

Coronary capillary vascular flow (Q_{c2}) was calculated and data for one cardiac cycle are presented in Figure 4.11. The maximum flow of 7.20 ml/s occurs 0.13 sec after t_{rb} or 0.09 sec after the closure of AV; and the minimum flow of 1.40 ml/s occurs 0.34 sec before t_{rb} or 0.04 sec after the closure of MV. The average flow was calculated as 4 ml/s. For comparison, coronary capillary flow data (in ml/min), obtained in dogs and extrapolated to humans for size-matching, are given in Figure 4.12 [3]. Both graphs show phasic flow patterns with an abrupt drop during IVC and a plateau at minimum level during ventricular ejection, and a fast rise to the maximum level during IVR followed by a slow decline during ventricular filling.

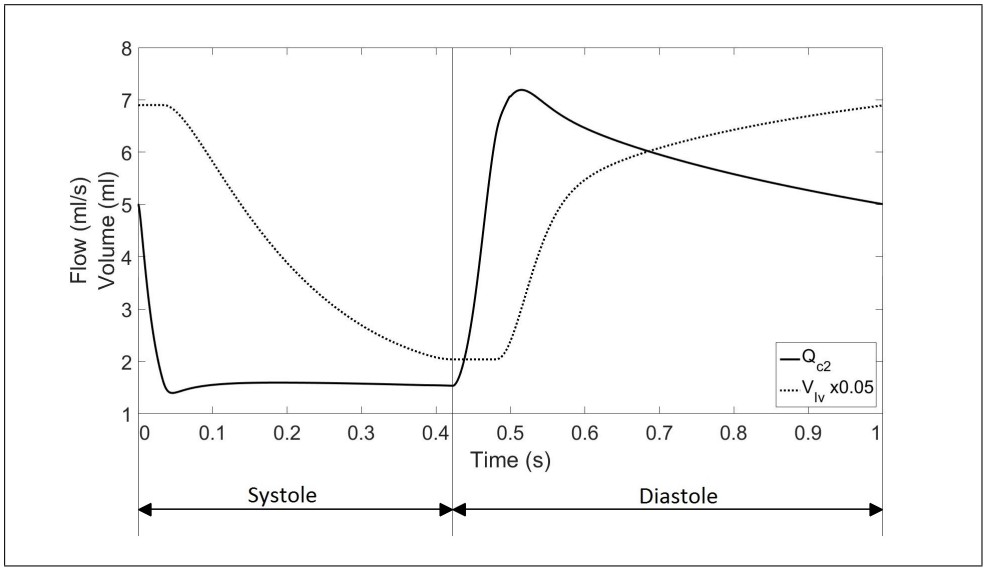

Figure 4.11 Simulated coronary capillary vascular flow (Q_{c2}) and left ventricular volume (V_{lv} x0.05) as a function of time

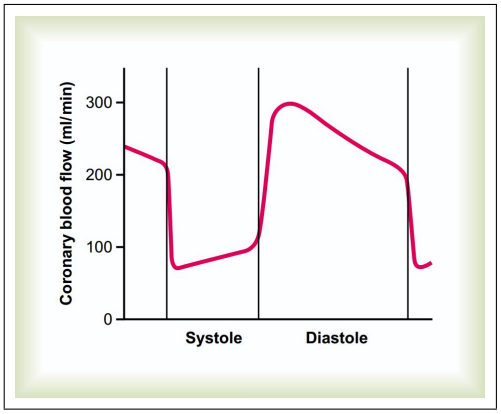

Figure 4.12 Coronary capillary flow, obtained in dogs and extrapolated to humans [3]

4.3 Volume Domain Analysis of the State Variables

Eliminating the time variable from Figure 4.5, it was possible to relate pressure and volume directly to each other and show the resulting relationship as a PVL (Figure 4.13). In this figure, $V_{lv,0}$ corresponds to the theoretical zero-pressure volume of the LV (set at -1.5 ml for this run); $V_{lv,ed}$ and $V_{lv,es}$ represent LV end-diastolic and end-systolic volumes, respectively; and $P_{lv,be}$, $P_{lv,max}$ and $P_{lv,es}$ are LV pressures at beginning of ejection, peak ejection and end of systole, respectively. Since, the values of the model constants and control parameters are identical in Figure 4.5 and Figure 4.13, physiologic variables are unchanged. The advantage of using the PV plane is that end-systolic elastance, E_{max}, of the LV can be directly estimated from the angle between the abscissa and the dashed line. As mentioned earlier, E_{max} is an indicator of the intrinsic power of the LV also referred to as LV contractility or LV contractile state. In Figure 4.13, E_{max} was calculated as 2.47 mmHg/ml.

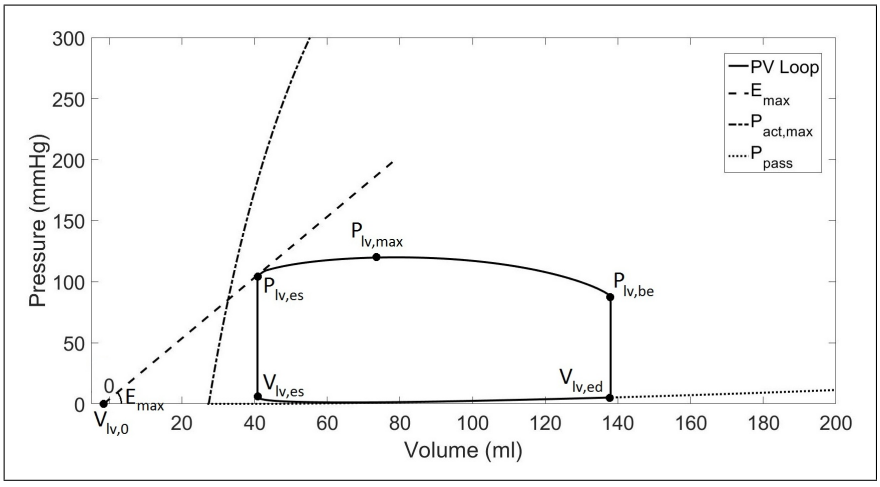

Figure 4.13 Simulated left ventricular pressure-volume loop

As the total blood volume was increased by infusing external fluid at a rate of $Q_{ext} = 0.5$ [ml/s], EDV was observed to increase in accordance with the Frank-Starling Mechanism (Figure 4.14). In response to Q_{ext}, PV Loops were observed to shift to the right as $V_{lv,ed}$ and $V_{lv,es}$ increased; as well as $P_{lv,be}$, $P_{lv,max}$ and $P_{lv,es}$. The end-systolic points of each loop defined a straight line (End-Systolic Pressure Volume Relationship, ESPVR) with slope E_{max} and volume axis intercept $V_{lv,0}$.

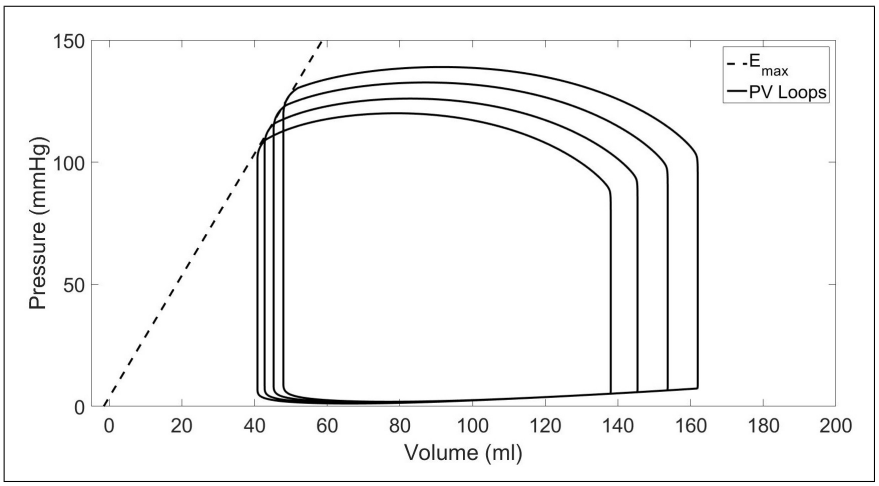

Figure 4.14 Pressure-Volume Loops corresponding to varying amounts of EDV

The changes in the shape of the PV Loops in response to simulated changes in the inotropic state of the myocardium are shown in Figure 4.15. Positive inotropic changes were simulated by increasing the β_T and β_ϑ to 0.9 and 1.275, and negative inotropic change was simulated by decreasing the β_T and β_ϑ to 0.48 and 0.68; from their normal values of 0.6 and 0.85, respectively. In response to an increase in the inotropic state, the values of E_{max} and $V_{lv,0}$ both increased from their initial values under normal inotropic state shown in Figure 4.14, to 13.22 mmHg/ml and 24.5 ml, respectively; while they both decreased to 1.14 mmHg/ml and -31.1 ml in response to a decrease in the inotropic state, respectively. Also, both $V_{lv,ed}$ and $V_{lv,es}$ decreased; while $P_{lv,be}$, $P_{lv,max}$ and $P_{lv,es}$ increased, continuously, as the myocardial contractility was changed from negative to normal to positive inotropic state. For comparison, PV Loops from Suga et. al. (1973) [5] and ESPVR lines from Burkhoff et. al. (2005) [65] under normal and increased inotropic states are shown in Figure 4.16 and Figure 4.17, respectively. It was noted that the increase in E_{max} observed in the simulated data of Figure 4.15 was consistent with respective changes shown in Figure 4.16 and Figure 4.17; but that the increase in $V_{lv,0}$ shown in the simulations was consistent with data of Figure 4.17 only, as $V_{lv,0}$ in Figure 4.16 remains constant as the inotropic state changes.

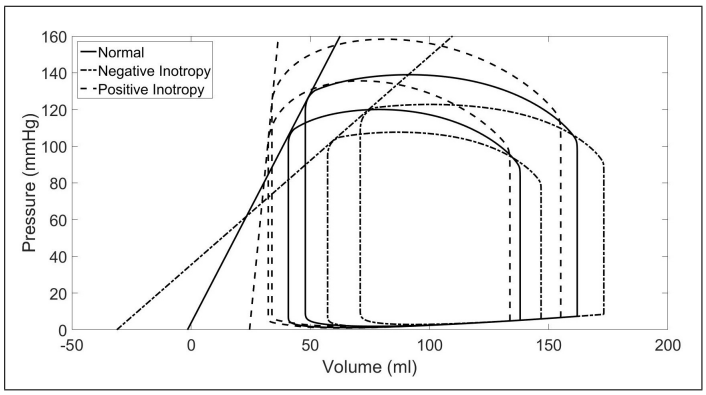

Figure 4.15 Pressure-volume loops and ESPVR lines for normal, positive inotropic and negative inotropic simulation conditions

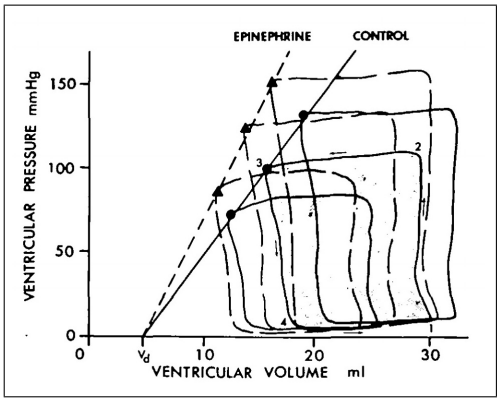

Figure 4.16 Pressure-volume loops and ESPVR lines obtained in the canine left ventricle under normal (control) and positive (epinephrine) inotropic states [5]

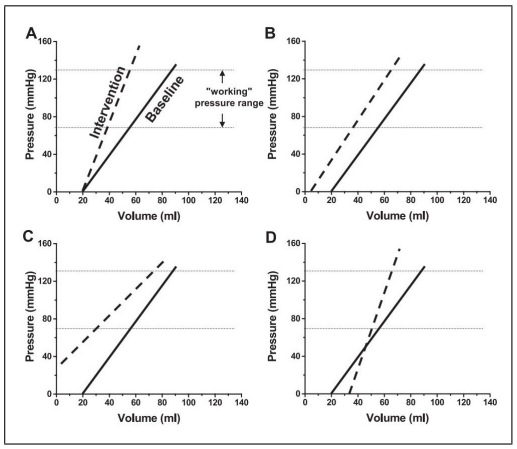

Figure 4.17 Variations in the ESPVR line in response to positive inotropic effect. A: Unchanged $V_{lv,0}$ with increased E_{max}. B: Decreased $V_{lv,0}$ with unchanged E_{max}. C: Decreased $V_{lv,0}$ and E_{max}. D: Increased $V_{lv,0}$ and E_{max} [65]

A load-independent performance index, which utilizes the normalized ratio between left ventricular power and square of left ventricular EDV, suggested by Kass and Beyar (1991) [66]. This method was used to calculate the values for solid line given in Figure 4.18, which are then plotted against left ventricular EDV. Additionally, normalized ratio between LV power and EDV, and normalized LV power were added for comparison. The relationship between LV power and square of EDV w.r.t. left ventricular EDV results with an almost flat line, which is in accordance with Figure 4.19 [66].

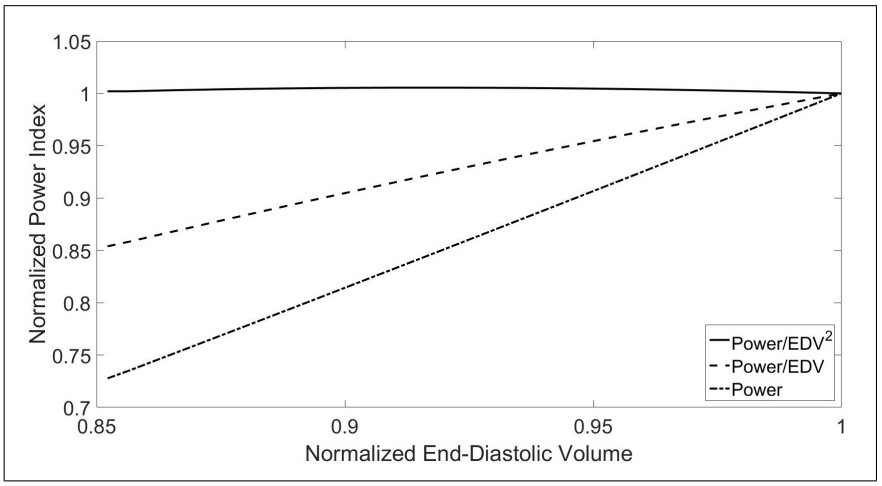

Figure 4.18 Load-independent performance index Power/EDV^2 w.r.t. left ventricular EDV in comparison to Power/EDV and Power

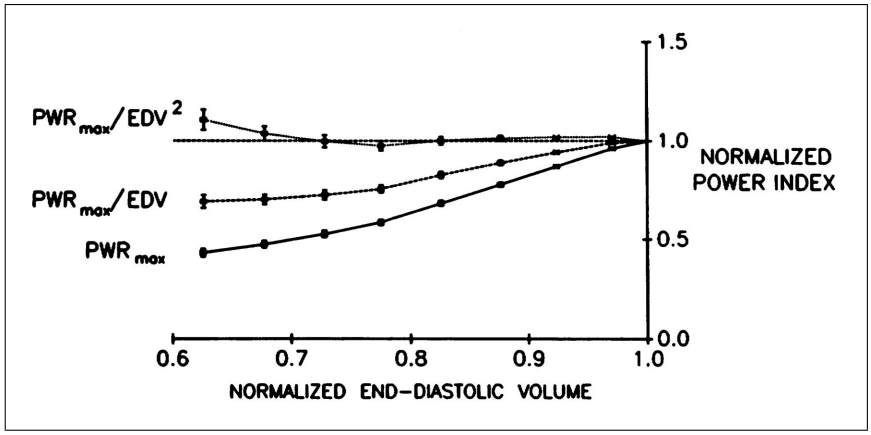

Figure 4.19 Power/EDV^2 w.r.t. left ventricular EDV in comparison to Power/EDV and Power [66]

In Figure 4.20, Figure 4.22 and Figure 4.24 load-dependent performance parameter (i.e. CO, SW, EF) results from simulations for normal physiological conditions were plotted against increasing left ventricular EDV. For comparison, relationship between CO and left ventricular EDV [4] and relationship between SW and left ventricular EDV for canine left ventricle [67] were given in Figure 4.21 and Figure 4.22, respectively. CO in Figure 4.20 and SW in Figure 4.22 show a linearly increasing relationship w.r.t. EDV, in parallel with the Frank-Starling Mechanism. On the other hand, in Figure 4.24, EF present a concave relationship w.r.t. EDV, where it's maximum is 70.6% at 149 ml, with an average of 70.5%.

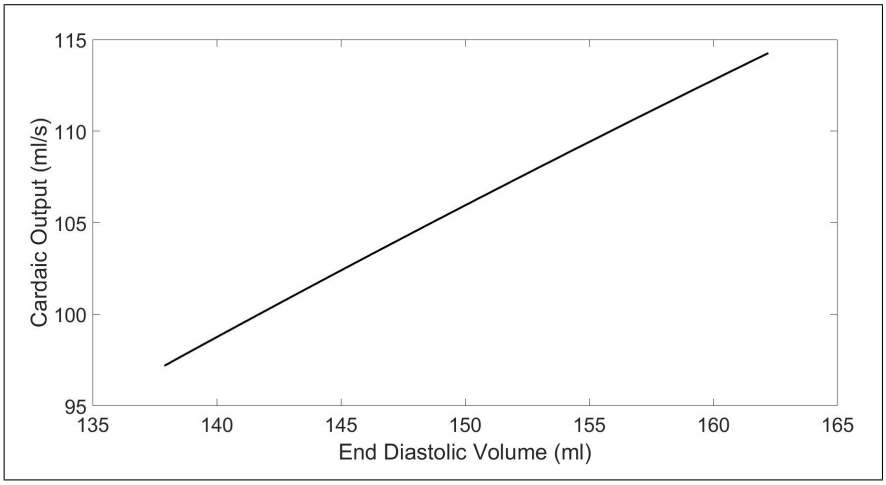

Figure 4.20 Calculated CO w.r.t. increasing left ventricular EDV

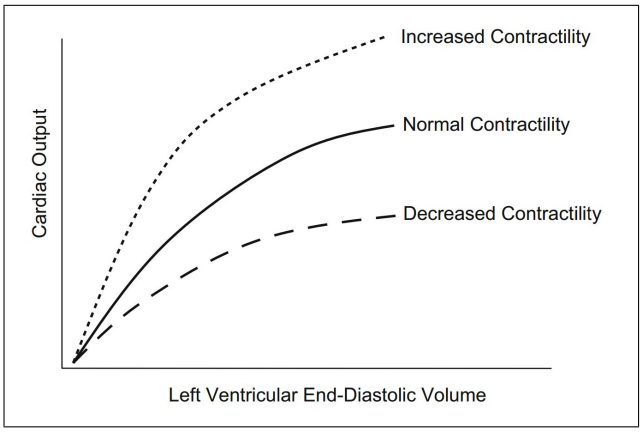

Figure 4.21 Relationship between CO and increasing left ventricular EDV for different contractile states [4]

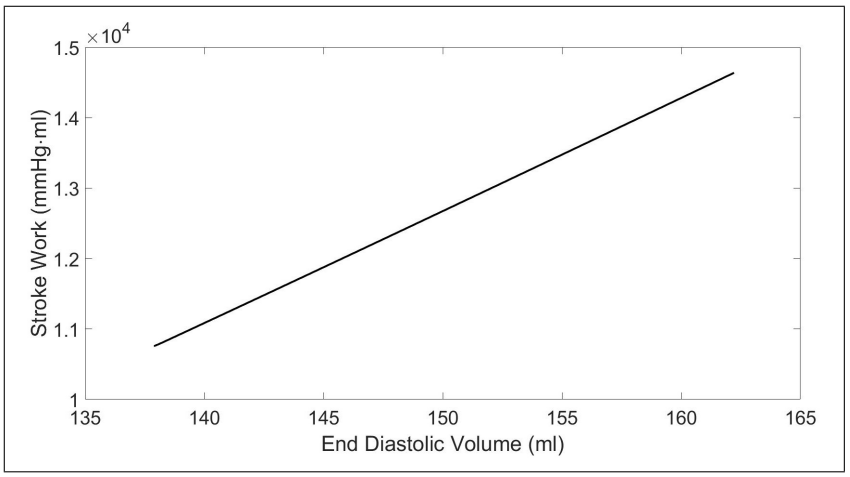

Figure 4.22 Calculated SW w.r.t. increasing left ventricular EDV

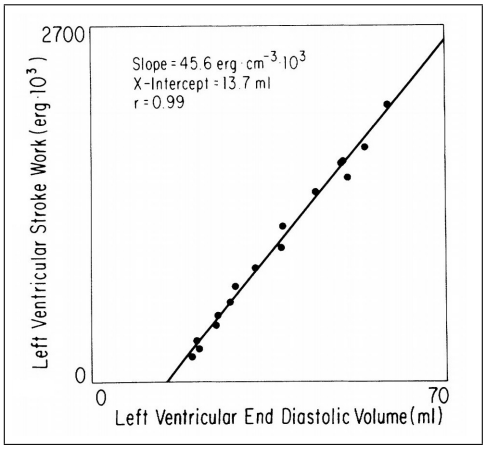

Figure 4.23 Relationship between SW and increasing left ventricular EDV in canine LV [67]

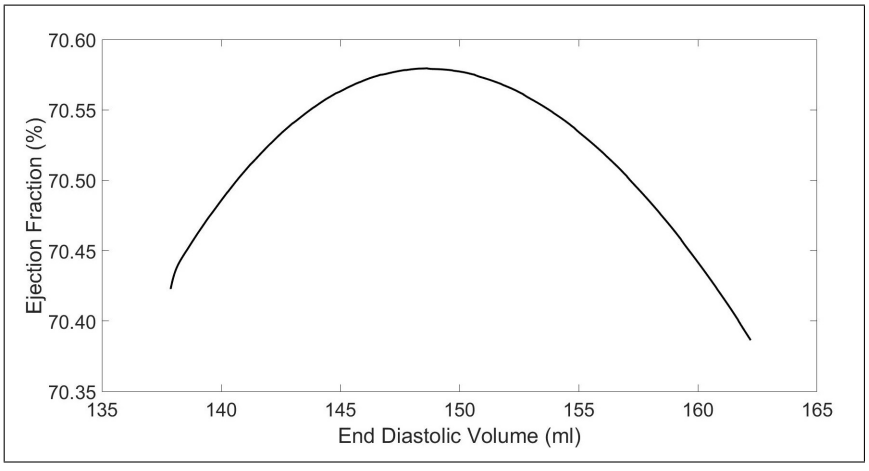

Figure 4.24 Calculated EF w.r.t. increasing left ventricular EDV

4.4 Relationship between State Variables and Systolic Duration

Under normal physiological conditions, the isolated effect of systolic duration (0.2 sec $< t_{rb} <$ 0.7 sec) on the state variables was studied (Figure 4.25 through Figure 4.27). Changes in critical left ventricular volumes and pressures w.r.t. increasing t_{rb} are presented in Figure 4.25. Both $V_{lv,ed}$ and $V_{lv,es}$ showed a decay w.r.t. increasing values of t_{rb}. Initially, a relatively small increase is observed in $P_{lv,max}$ followed by a peak and a slow decline. Similarly, $P_{lv,es}$ presented an increase, followed by a peak and a decrease w.r.t. increasing t_{rb}. On the other hand, $P_{lv,be}$ demonstrated an initial rise, followed by a marginally flat plateau for rising values of t_{rb}. Finally, $P_{lv,ed}$ showed a steady decline.

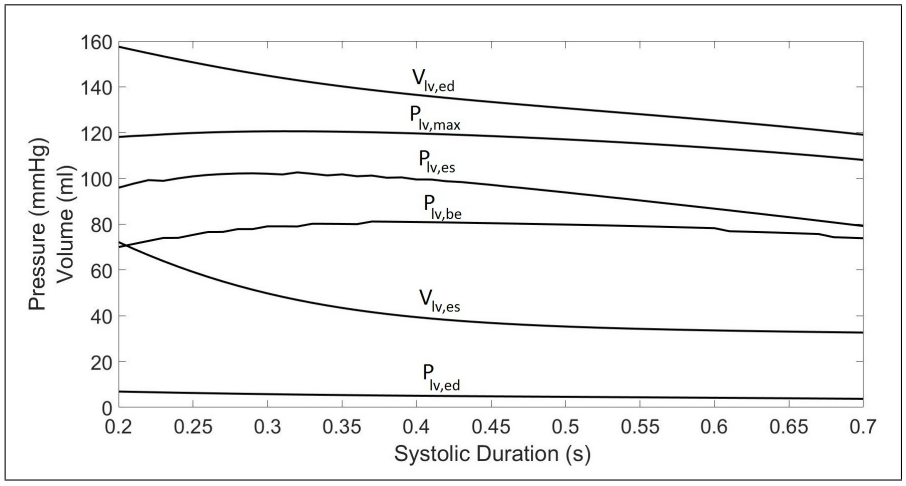

Figure 4.25 Left ventricular pressures and volumes w.r.t. systolic duration (t_{rb})

In Figure 4.26 energetics of the left ventricle was evaluated in terms of PVA, PE, SW and efficiency. A fast increase followed by a peak at $t_{rb} = 0.37$ [s], then a steady decline was observed in SW. While, PVA showed a similar pattern with its peak at $t_{rb} = 0.29$ [s]. On the other hand, PE displayed a decay for increasing t_{rb}. Efficiency was observed to have a positive trend with decreasing slope.

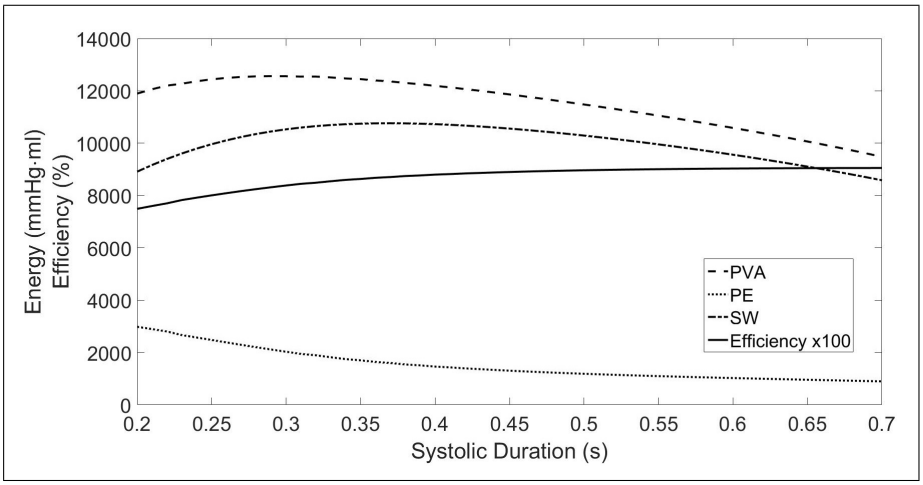

Figure 4.26 Left ventricular PVA, SW, PE and efficiency w.r.t. systolic duration (t_{rb})

In Figure 4.27 Mean Arterial Pressure (MAP), CO and left ventricular power showed a concave relationship w.r.t. t_{rb} with their maximum values at 0.39 sec.

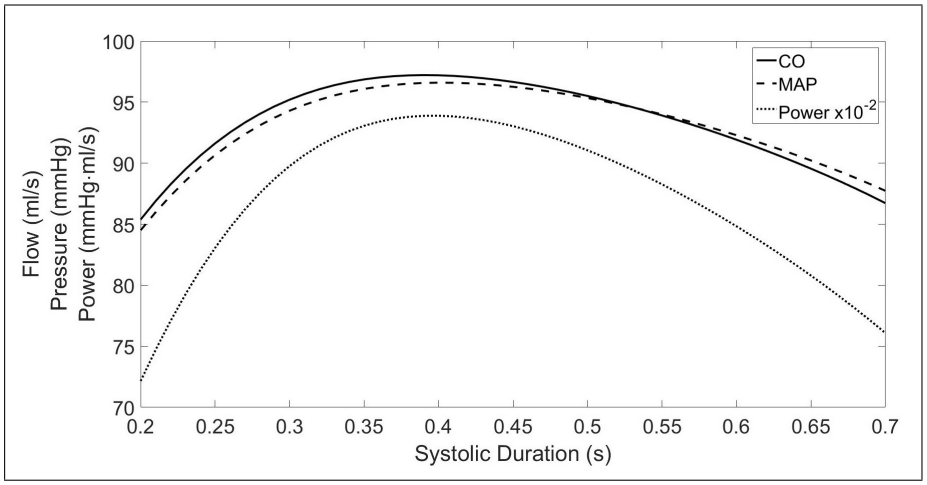

Figure 4.27 MAP, CO and left ventricular power w.r.t. systolic duration (t_{rb})

4.5 Oxygen Supply-Demand Balance of the Left Ventricle

Oxygen demand by left ventricle, oxygen supply by the coronary circulation and their difference oxygen deficit (error) plots were given in Figure 4.28 w.r.t. simulation time, as the EDV of the left ventricle was increased via $Q_{ext} = 0.5$ [ml/s]. Oxygen demand starts around 0.4 mlO_2/beat with small fluctuations and steadily increases with time due to increase in EDV. On the other hand, oxygen supply jumps from its beginning value of 0.26 mlO_2/beat to 0.52 mlO_2/beat in 7 seconds reaching a steady state and increasing with the same slope as oxygen demand. In the beginning, a positive error (oxygen deficit) of 0.25 mlO_2/beat occurs, which is compensated in 7 seconds (Figure 4.29) and stayed at zero with negligible fluctuations (less than 0.2% of the oxygen supply).

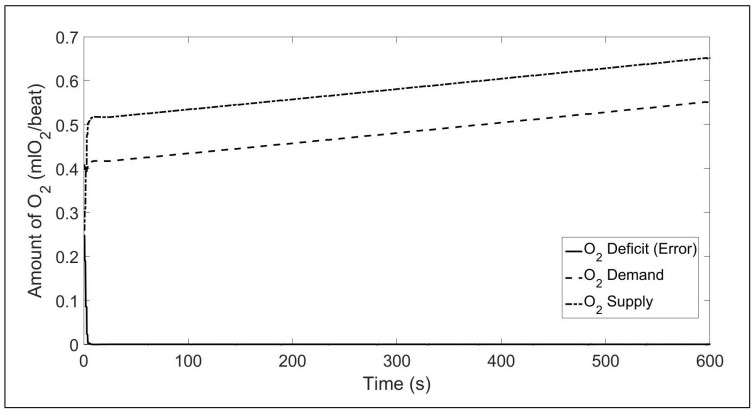

Figure 4.28 Time domain graph of oxygen demand, supply and deficit (error) as the left ventricular EDV increased via $Q_{ext} = 0.5$ ml/s

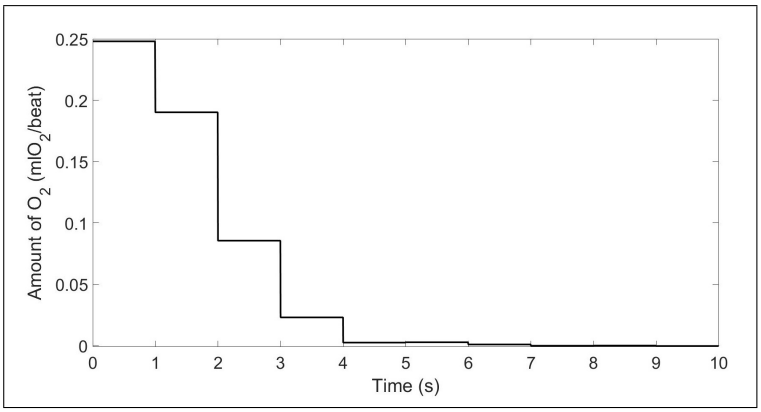

Figure 4.29 Transient response of the oxygen deficit (error) w.r.t. simulation time

In Figure 4.30 average coronary capillary blood flow ($Q_{c2,avg}$) graph was given w.r.t. simulation time as the EDV of the left ventricle was increased via $Q_{ext} = 0.5$ [ml/s]. Average flow starts with an initial value of 2.4 ml/s, which, then increases to 4 ml/s steady state in 7 seconds, followed by a climb with a constant slope.

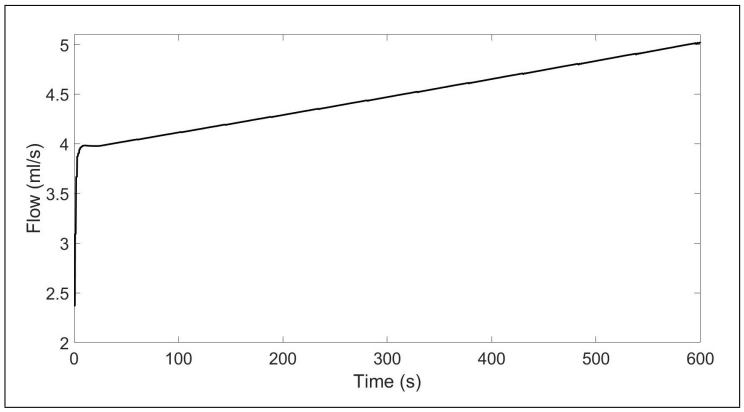

Figure 4.30 Time domain graph of average coronary capillary flow ($Q_{c2,avg}$) as the EDV increased via $Q_{ext} = 0.5$ ml/s

5. CONCLUSIONS

Based on the aims, given in Section 2.4, and the simulation results, the following conclusions have been drawn about the performance of the system.

When β_T and ξ_P are chosen appropriately, the model was able to mimic the isometric contraction and passive extension characteristics of the cardiac muscle, in terms of both length-tension (Figure 4.1) and volume-pressure relationships (Figure 4.3). As shown in Figure 4.3, $P_{act,max}$ increased within the physiological volume range and reached a peak value at left ventricular volume of 200 ml (corresponding to sarcomere length of 2.30 μm) which is over the physiological limit of human heart [59]. Therefore, it is safe to say that the modeling approach taken is sound.

When operated under normal physiological conditions, the state variables (Figure 4.5) remained within physiological ranges [3, 59], and produced steady-state values close to their respective initial conditions (Figure 4.7). Constant blood volume constraint was obeyed. All confirming that governing equations of the system were constructed properly, and parameters and coefficients were chosen correctly.

The response of the plant to external disturbance (Q_{ext}) on the PV Loop was observed in Figure 4.14, and found to be in parallel with [5]. Effects of both parameter variations (β_T and β_ϑ), which simulates healthy rest by normal, healthy exercise by positive and disease rest by negative inotropic sates, and external disturbance (Figure 4.15) were found to be consistent with the literature [5, 65].

One of the load-dependent performance indexes, CO, demonstrated almost linear relationship w.r.t $V_{lv,ed}$ (Figure 4.20), which is in accordance with the literature under normal physiological loading conditions [4]. In normal physiological limits, another load-dependent performance index, SW, in Figure 4.22, showed a linear relationship w.r.t. $V_{lv,ed}$ when compared to the data of Glower et. al. (1985) [67]. Additionally, in

Figure 4.24, final load-dependent performance index, EF, was shown to be at the high end of the nominal limits [68].

First load-independent performance index, ESPVR, (Figure 4.15) maintained its constant slope, for a given inotropic state, despite increasing preload ($V_{lv,ed}$) and afterload ($P_{lv,be}$), showing that ESPVR is a load-independent performance parameter of the ventricle. In case of inotropic state changes, ESPVR demonstrated variations in E_{max} and V_0 that are consistent with the literature [5, 65]. Another load-independent performance index, Power over EDV squared, (Figure 4.18) remained constant over a wide range of left ventricular end-diastolic volume in parallel with earlier experimental studies [66]. The results gathered from load-dependent and -independent performance indexes confirmed that the model could accurately recreate the real cardiac physiological dynamics.

Coronary capillary vascular flow (Q_{c2}) in Figure 4.11 mimicked the real phasic flow characteristic of the coronary circulation [3], proving that the coronary circulation model parameters were chosen accurately. Coronary flow control, which kept the oxygen supply over demand ($D_{O2} = 0.70 \cdot S_{O2}$) with zero oxygen deficit (error) in steady-state (Figure 4.28), was achieved utilizing left ventricular oxygen supply and demand balance. Consequently, a raise in $Q_{c2,avg}$ (Figure 4.30) was observed as the oxygen demand increased, suggesting that the controller worked as intended. A relatively fast transient phase of 7 seconds (Figure 4.29) proved that the calibration of the controller was made appropriately.

When the effect of the binary activation signal "u" on the system, via changing the systolic duration (t_{rb}), was evaluated, LV volume paths in Figure 4.25 were found to be realistic considering subsequent changes in the diastolic (filling) duration and the Frank-Starling Mechanism. The end-diastolic and end-systolic volumes decreased for increasing systolic duration, due to reduced filling time, showing that the model responds similar to its real world counterpart. The increase in efficiency (Figure 4.26) for increased systolic duration was related with the fast decrease in PVA compared to SW, therefore it could not be used to determine the optimal working point of the LV.

However, maximum SW point (Figure 4.26) and maximum power point (Figure 4.27) were found to be at 0.37 sec and 0.39 sec, respectively. Hence, the optimum systolic time, where the model does the most useful work with greatest power, was chosen as 0.38 sec.

The model was constructed with subsystems, signal line connection modules (From/Go To blocks), and labels in MATLAB/Simulink to enable modularity for modifications. A single activation signal, "u", was used as input, and left ventricular oxygen demand and coronary oxygen supply balance were established; both of which were utilized to make the system compatible with future formulations of optimal control.

6. FINAL DISCUSSION AND FUTURE WORK

In this thesis a novel time-varying ventricular pressure and elastance generation method, which based on active and passive characteristics of myocardial sarcomere, was designed; and coupled with a conventional cardiovascular lumped model. To the best of our knowledge, this is the first time that the myocardial active state was formulated with a single unified equation (Equation 3.67) that satisfies isometric, isotonic and auxotonic relationships.

Conventional cardiovascular lumped models are, generally, linear time-invariant systems that adopt finite number of Windkessel groups on discrete interest points to mimic the real world counterpart. Therefore, this approximation of a real-world continuous system as a zero-dimensional model, which does not incorporate fluid dynamics, is a limitation. Although there are other methods (i.e. one and three dimensional distributed models) more accurate at mimicking cardiovascular system, they are quite slow for simulation purposes compared to lumped models. Additionally, errors caused by lumped modeling approach were shown to be insignificant, in mock circuit design [39]. Hence, selection of the lumped modeling approach, in this thesis, originates from its convenience and simplicity.

Several assumptions regarding myocardial sarcomeres were made, to simplify the model and to make the system applicable:

1. Myocardium is made up from uniformly distributed parallel strings of sarcomeres in series.
2. Both the muscle and the sarcomere are isotropic in cross-section.
3. Sarcomeres exhibit all macro-scale properties of myocardium in the micro-scale.
4. Sarcomeres within the whole myocardium change length simultaneously with the same velocity.

5. Sarcomeres always contract with the available peak velocity for any given length-load pair.

6. Myocardial volumetric activation percentage has a one-to-one correspondence with activation percentage of any individual sarcomere.

Assumptions 1 through 3 were made to simplify the curve fitting procedure of passive and maximum active tensions (Equation 3.68 and Equation 3.61, respectively). Normally, myocardial tissue is connected like a mesh network called Syncytium, therefore it is neither uniformly distributed nor isotropic in cross-section. Sarcomeres demonstrate different properties in micro-scale compared to muscle in macro scale, due to orders of magnitude size and mass differences. Errors due to these assumptions were compensated with coefficients β_T and ξ_P.

Assumptions 1, 3 and 4 enabled the curve fitting of individual tension-velocity curves (Equation 3.55) and the development of length-maximum velocity relationship (Equation 3.65). Due to activation delays, inertial effects and complex mechanical interaction between individual sarcomeres, each sarcomere responds differently. Therefore all sarcomeres cannot change length simultaneously with the same velocity in normal circumstances. Errors caused by these assumptions were compensated to a certain extend with coefficient β_ϑ.

Assumptions 1 through 5 were important for the derivation of instantaneous tension-length-velocity relationship. Especially assumption 5 is the back-bone of this model as the surface defined by the Equation 3.67 is always on the peak velocity for any give length-load pair. Realistically, this is not possible due to mechanical inertial effects and delays in activation. Errors introduced by these assumptions were dealt with using coefficients β_ϑ, β_T and ξ_P, and the control signal "a".

Assumption 6 was made to incorporate the control signal "a" into the system such that micro-scale properties could be magnified to the macro-scale. However, individual sarcomeres get activated in a binary fashion, while myocardium get activated

regionally. Errors accumulated here has negligible effects on the system, due to the setup of the model incorporating assumptions 1 through 3.

Data used in curve fitting procedures were gathered from the literature. Despite the great care given while incorporating these information, errors occurred from known and unknown sources. To increase the modeling accuracy, dedicated in-vivo test are recommended in future research to verify the taken approaches.

Pressure production from tension via a constant coefficient of α is a simplistic approach, which is not accurate in a methodological sense. Therefore, it is the biggest limitation in this thesis. The correct approach of conversion should have been the utilization of Laplace Law or other analytical methods from the literature. Initially, four conversion methods, Laplace Law for ellipsoid and cylinder, an augmented Laplace Law suggested by Falsetti et. al. (1970) [69] for sphere, and a tension-pressure conversion method suggested by Arts et. al. (1991) [70] for ellipsoid, were tried to be utilized. When their respective volume-varying tension-pressure conversion coefficients of $\theta_{le}(V)$, $\theta_{lc}(V)$, $\theta_{fs}(V)$ and $\theta_{ae}(V)$ (Appendix E) were plotted against ventricular volume (Figure 6.1), the results were found to be consistent within themselves. Also, the results of $T_{act,max}$ and T_{pass}, which were gathered prior to the pressure conversion, were found to be consistent with the literature. When the volume-varying tension-pressure coefficients, $\theta(V)$, were multiplied with $T_{act,max}$ and T_{pass}, graphs of $P_{act,max}$ (Figure 6.2) and P_{pass} (Figure 6.3) were acquired, respectively. In Figure 6.2, all $P_{act,max}$ curves made a premature peak around 80 ml, instead of at 200 ml; and in Figure 6.3, all P_{pass} curves followed a linear trajectory, instead of an exponential one. Therefore, resulting graphs, though consistent within themselves, did not reflect the results from the literature (Figure 4.4). Replacing the volume-varying coefficient $\theta(V)$ with the constant coefficient α solved the mismatch between the obtained results and the literature, while sacrificing the methodological consistency. The origin of this problem is unknown and finding a solution should be a priority in the future development.

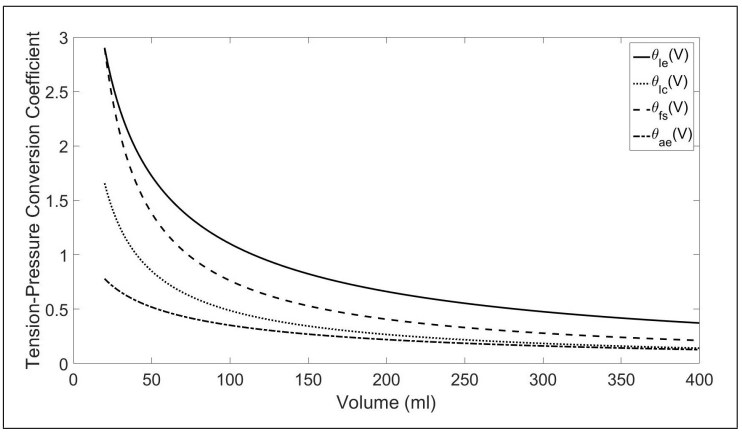

Figure 6.1 Volume-varying tension-pressure conversion coefficients

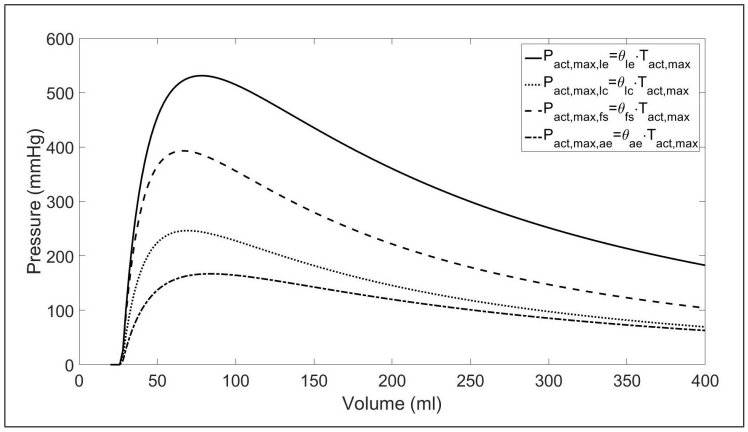

Figure 6.2 Maximum active pressure curves as a function of ventricular volume, calculated via volume-varying tension-pressure conversion coefficients

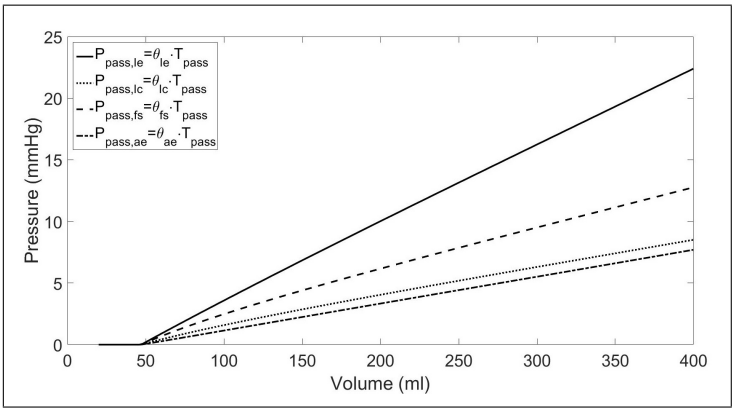

Figure 6.3 Passive pressure curves as a function of ventricular volume, calculated via volume-varying tension-pressure conversion coefficients

The binary activation signal "u" and the control signal "a" are arbitrarily defined signals, whose equations and coefficients are selected purely based on trial and error, to drive the system. Methods, which will connect "u" and "a" to real biopotentials or cardiac events, such as ECG, could be subjects of future research.

Shapes of calculated normalized time-varying left ventricular elastance graph, given in Figure 4.9, and normalized time-varying elastance graph of canine left ventricle from Suga et. al. (1973), given in Figure 4.10 [5], presented significant differences. First of all, in Figure 4.9, a drastic slope change, which marked the end of IVC, was observed around 0.25 point of normalized time; however, in Fig. 4-10, a relatively small slope change was seen around 0.4 point of normalized time. Secondly, Figure 4.9 showed a bilinear-like pattern of ascent, while Figure 4.10 acted more like a concave curve. Lastly, after the maximum normalized elastance point was reached, Figure 4.9 displayed a faster descent compered to Figure 4.10. Most notable disagreements between the curves are the initial fast rise and abrupt fall in Figure 4.9, which correspond to the IVC and most of the IVR. These are mainly related with ascent and descent portions of the control signal "a". Hence, a possible solution may be achieved via the manipulation of "a".

Calculated ESPVR relationships for normal, positive and negative inotropic states were given in Figure 4.15, in comparison with the experimental ESPVR relationships obtained in canine left ventricle for normal and positive inotropic states from Suga et. al. (1973) as shown in Figure 4.16 [5]. As expected both graphs show an increase in the slope of ESPVR for positive inotropic intervention, with a critical difference of the misalignment of $V_{lv,0}$ values. In Figure 4.16 $V_{lv,0}$ points of both ESPVR lines are coincident, on the other hand in Figure 4.15 the $V_{lv,0}$ points shift towards right as the slope of ESPVR increases. This discrepancy was explained by Burkhoff et. al. (2005), where the slope of ESPVR and value of $V_{lv,0}$ are allowed to change as shown in Figure 4.17 for positive or negative inotropic interventions [65].

As a future work, the model should be augmented with a controller, which would determine the optimal systolic duration, t_{rb}, and run the system at the maximum power point with the optimum ejection pattern for varying external disturbances and system parameters. Pontryagin Maximum Principle may be a candidate approach as studied by [71] - [73].

Performance of the heart is dependent on the time-varying elastance, which is directly related to pressure and inversely related with volume. Therefore, conventional time-varying elastance based control was used in zero-dimensional lumped models or mock circuits to generate ventricular pressure from volume (or the other way around). Usage of ventricular volume as a feedback for pressure generation is an important factor that satisfies Frank-Starling Law. This conventional method of predefined time-varying elastance input has not been used in this thesis. Instead a novel time-varying elastance generation method, which originates from the active (isometric and auxotonic) and passive myocardial biomechanics, was created; enabling the acquisition of generated time-varying elastance as an output to verify the efficacy of the method. Even though the calculated normalized time-varying elastance showed minor differences, as explained above, the principal shape was consistent with the literature. Additionally, efficacy evaluations based on time course of state variables, load-dependent (CO, SW and EF) and -independent (ESPVR and power over EDV squared) indexes proved that the model mimicked the performance characteristics of the real LV. Therefore, it is safe to say that, the novel time-varying elastance generation method presented in this thesis shows a great promise to form the basis for future work to evaluate LVADs both in silico and in vitro.

APPENDIX A. PARAMETERS OF THE CIRCULATORY SYSTEM MODEL

A.1 Parameters of the Systemic Circulation

Parameters of the systemic circulation section of the plant were given in Table A.1 [39]. Parameters denoted with * were slightly altered to improve dynamic response of the system.

Table A.1
Parameters of the systemic circulation [39]

Parameter	Value	Units	Parameter	Value	Units
R_{0s}	0.0334	mmHg·s/ml	–	–	–
R_{a1}	0.0824	mmHg·s/ml	C_{a1}	0.7770	ml/mmHg
R_{a2}	0.1780	mmHg·s/ml	C_{a2}	1.6400	ml/mmHg
R_{a3}	0.6670	mmHg·s/ml	C_{a3}	1.8100	ml/mmHg
R_{v1}	0.0223	mmHg·s/ml	C_{v1}	13.240	ml/mmHg
R_{v2}	0.0267	mmHg·s/ml	C_{v2}	73.880	ml/mmHg
L_{a1}	0.00005	mmHg·s^2/ml	L_{v2}	0.00005	mmHg·s^2/ml
$V_{un,a1}$	205	ml	$V_{a1,ic}$*	280	ml
$V_{un,a2}$	370	ml	$V_{a2,ic}$*	500	ml
$V_{un,a3}$	401	ml	$V_{a3,ic}$*	500	ml
$V_{un,v1}$	596	ml	$V_{v1,ic}$*	700	ml
$V_{un,v2}$	1938	ml	$V_{v2,ic}$*	2300	ml

A.2 Parameters of the Pulmonary Circulation

Parameters of the pulmonary circulation section of the plant were given in Table A.2 [39]. Parameters denoted with * were slightly altered to improve dynamic response of the system.

Table A.2
Parameters of the pulmonary circulation [39]

Parameter	Value	Units	Parameter	Value	Units
R_{0p}	0.0251	mmHg·s/ml	–	–	–
R_{p1}	0.0227	mmHg·s/ml	C_{p1}	2.2220	ml/mmHg
R_{p2}	0.0530	mmHg·s/ml	C_{p2}	1.4810	ml/mmHg
R_{p3}	0.0379	mmHg·s/ml	C_{p3}	1.7780	ml/mmHg
R_{l1}	0.0252	mmHg·s/ml	C_{l1}	6.6660	ml/mmHg
R_{l2}	0.0126	mmHg·s/ml	C_{l2}	5.0000	ml/mmHg
L_{p1}	0.00005	mmHg·s^2/ml	L_{l2}	0.00005	mmHg·s^2/ml
$V_{un,p1}$	50	ml	$V_{p1,ic}$*	90	ml
$V_{un,p2}$	30	ml	$V_{p2,ic}$*	60	ml
$V_{un,p3}$	53	ml	$V_{p3,ic}$*	80	ml
$V_{un,l1}$	75	ml	$V_{l1,ic}$*	105	ml
$V_{un,l2}$	75	ml	$V_{l2,ic}$	105	ml

A.3 Parameters of the Coronary Circulation

Parameters of the coronary circulation section of the plant were given in Table A.3.

Table A.3
Parameters of the coronary circulation

Parameter	Value	Units	Reference
C_c	0.0006	ml/mmHg	[51]
$V_{un,c}$	28	ml	–
$V_{c,ic}$	28	ml	[74]
K_{c2}	0.5	ml/s	–
K_{im}	0.8	–	–

A.4 Parameters of the Left Heart

Parameters of the left heart section of the plant were given in Table A.4 [39]. Parameters denoted with * were slightly altered to improve dynamic response of the system.

Table A.4
Parameters of the left heart [39]

Parameter	Value	Units
R_{la}*	0.0050	mmHg·s/ml
C_{la}	13.333	ml/mmHg
L_{la}	0.000050	mmHg·s^2/ml
L_{lv}	0.000416	mmHg·s^2/ml
$V_{un,la}$	30	ml
$V_{la,ic}$*	80	ml
$V_{lv,ic}$*	130	ml

A.5 Parameters of the Right Heart

Parameters of the right heart section of the plant were given in Table A.5 [39]. Parameters denoted with * were slightly altered to improve dynamic response of the system.

Table A.5
Parameters of the right heart [39]

Parameter	Value	Units
R_{ra}*	0.0040	mmHg·s/ml
C_{ra}	16.667	ml/mmHg
L_{ra}	0.000050	mmHg·s^2/ml
L_{rv}	0.000206	mmHg·s^2/ml
$V_{un,ra}$	30	ml
$V_{ra,ic}$*	70	ml
$V_{rv,ic}$*	130	ml

APPENDIX B. SIMULINK BLOCK DIAGRAMS

B.1 Block Diagrams of the Plant

B.1.1 Block Diagrams of Systemic Circulation

Simulink block diagrams of the systemic circulatory sections are given in Figure B.1 through Figure B.5.

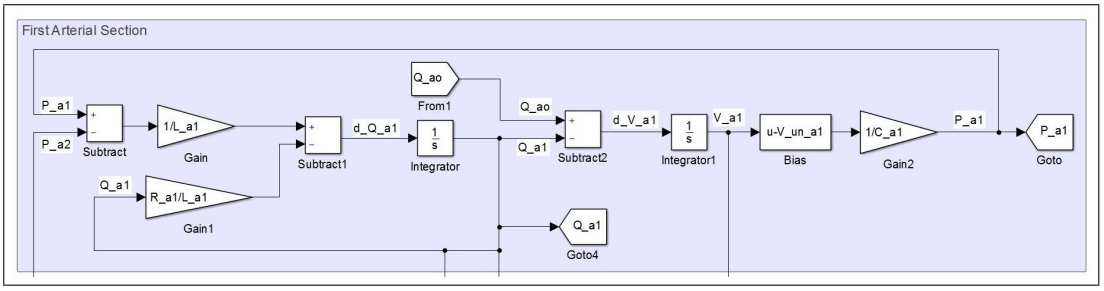

Figure B.1 Block diagram of the first systemic arterial section

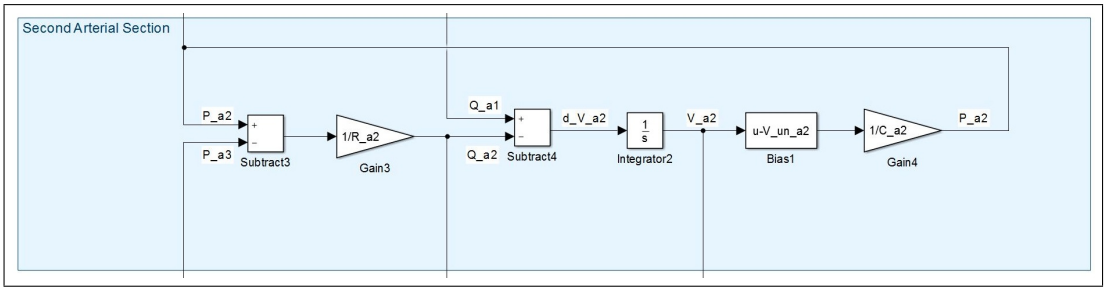

Figure B.2 Block diagram of the second systemic arterial section

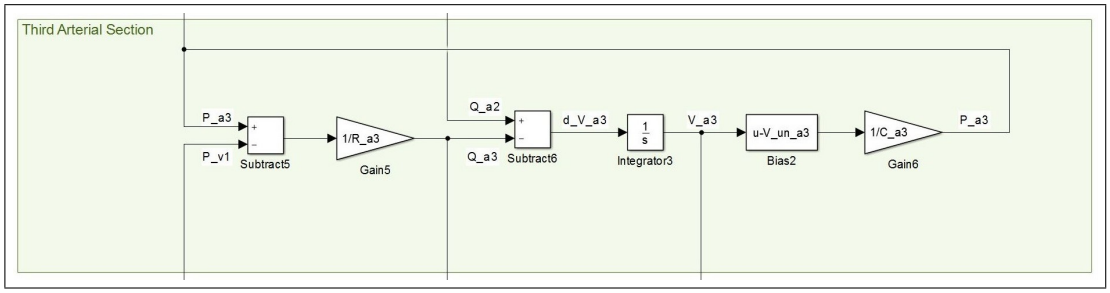

Figure B.3 Block diagram of the third systemic arterial section

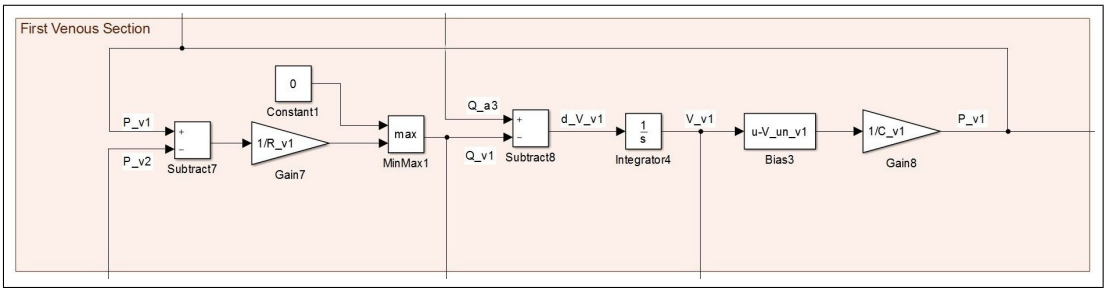

Figure B.4 Block diagram of the first systemic venous section

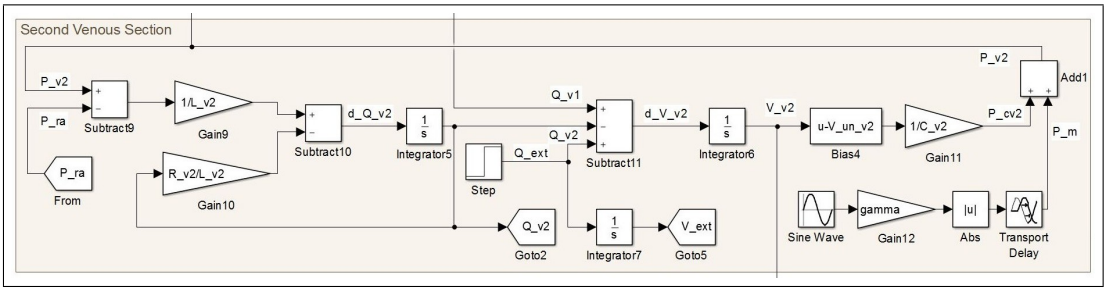

Figure B.5 Block diagram of the second systemic venous section

B.1.2 Block Diagrams of Pulmonary Circulation

Simulink block diagrams of the pulmonary circulatory sections are given in Figure B.6 through Figure B.10.

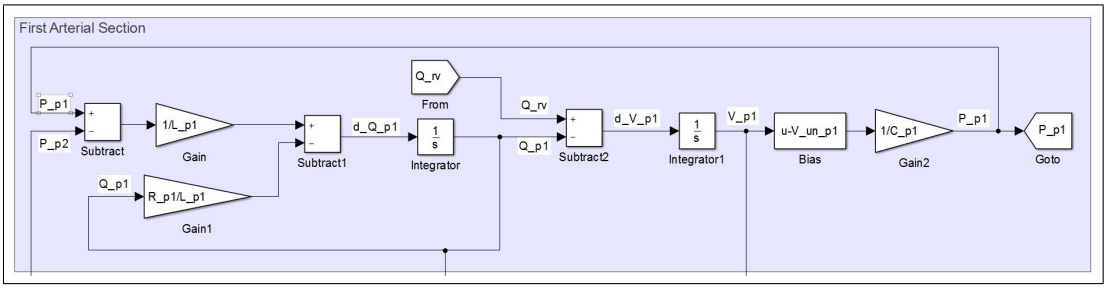

Figure B.6 Block diagram of the first pulmonary arterial section

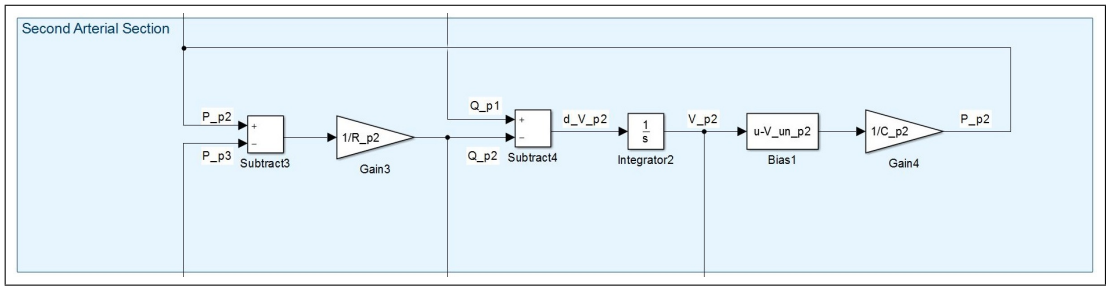

Figure B.7 Block diagram of the second pulmonary arterial section

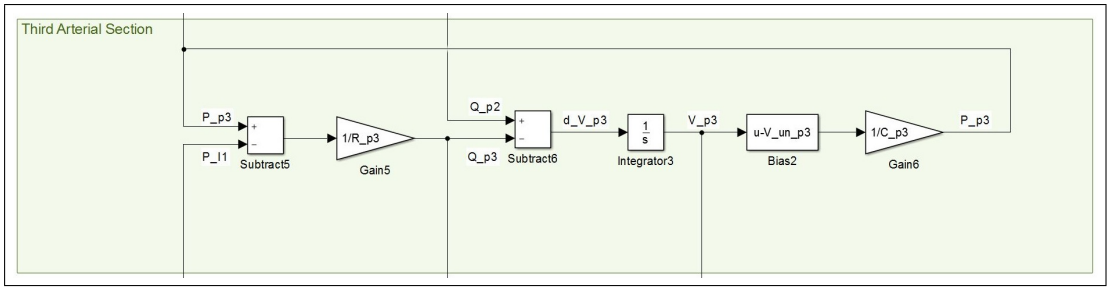

Figure B.8 Block diagram of the third pulmonary arterial section

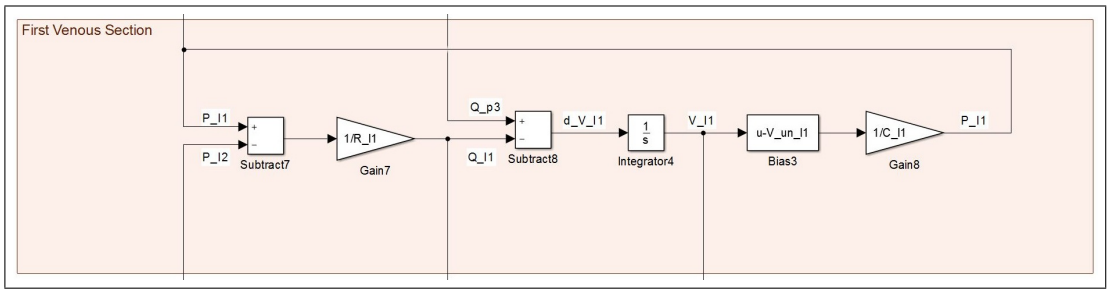

Figure B.9 Block diagram of the first pulmonary venous section

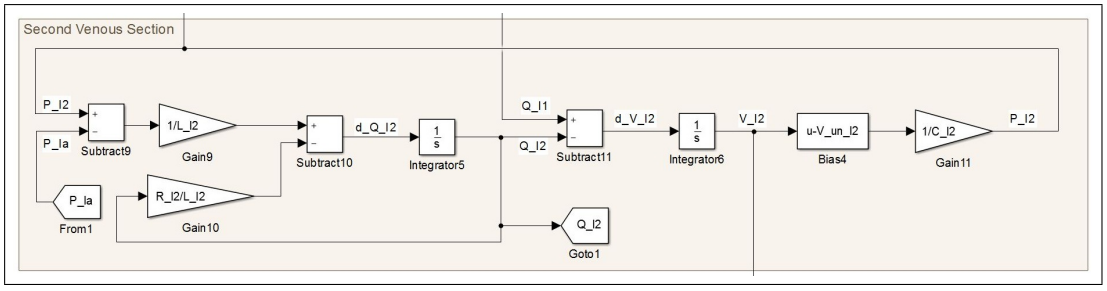

Figure B.10 Block diagram of the second pulmonary venous section

B.1.3 Block Diagram of Coronary Circulation

Simulink block diagram of the coronary circulatory section is given in Figure B.11.

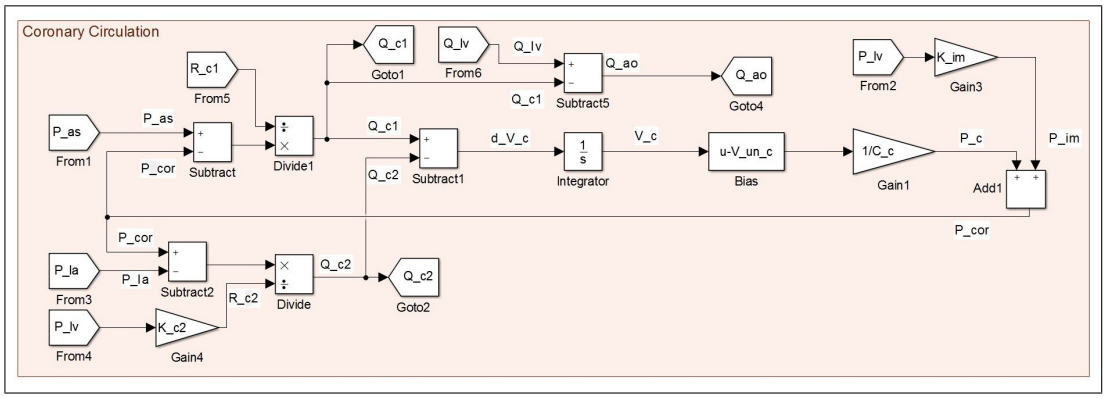

Figure B.11 Block diagram of the coronary circulatory section

B.2 Block Diagrams of Cardiac Chambers

B.2.1 Block Diagrams of the Left Heart

Simulink block diagrams of the left atrial and ventricular sections are given in Figure B.12 and Figure B.13, respectively.

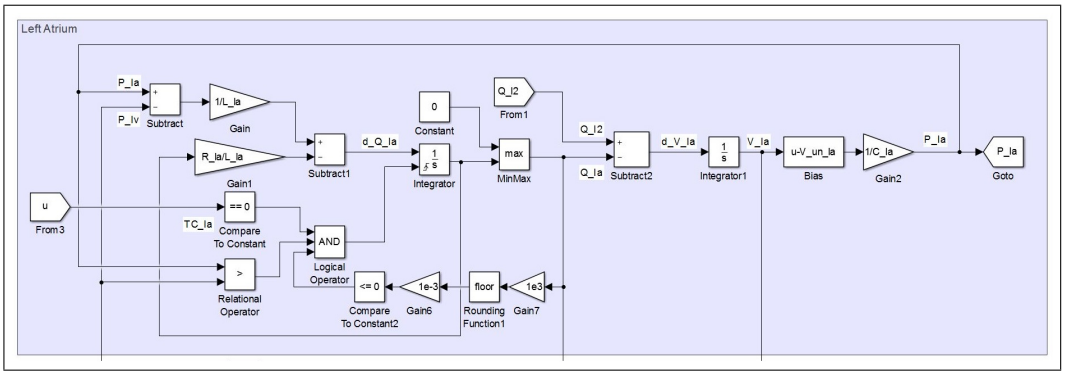

Figure B.12 Block diagram of the left atrial section

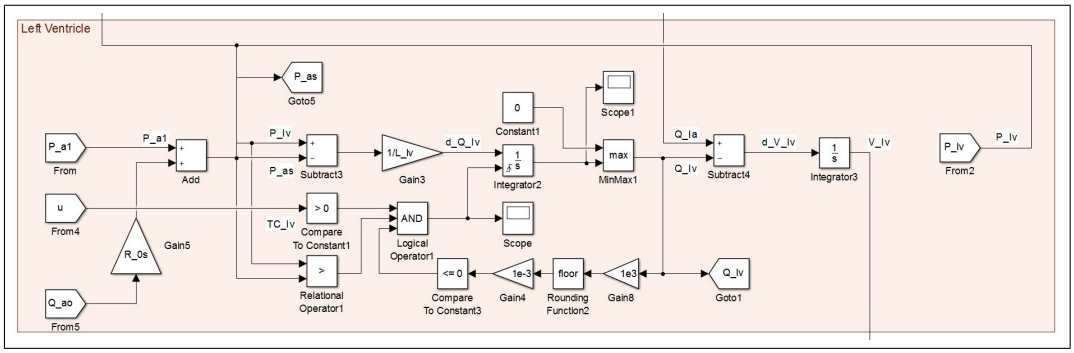

Figure B.13 Block diagram of the left ventricular section

B.2.2 Block Diagrams of the Right Heart

Simulink block diagrams of the right atrial and ventricular sections are given in Figure B.14 and Figure B.15, respectively.

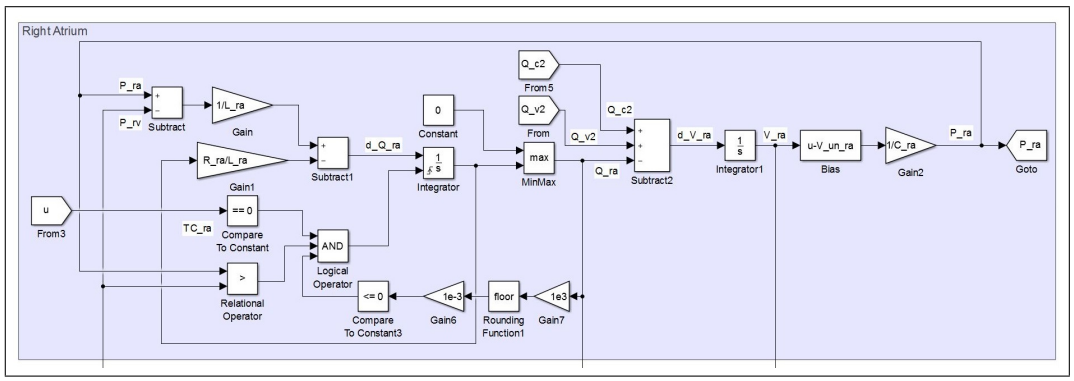

Figure B.14 Block diagram of the right atrial section

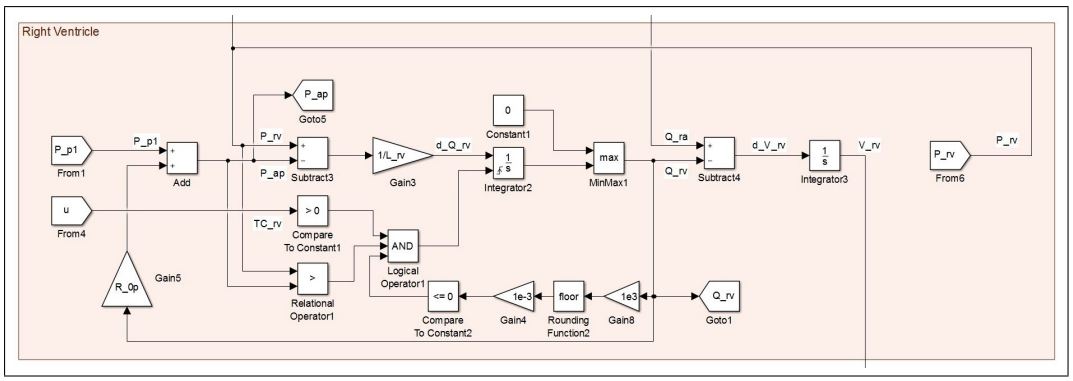

Figure B.15 Block diagram of the right ventricular section

B.3 Block Diagrams of Ventricular Pressure Generation and Control Systems

B.3.1 Block Diagram of Left Ventricular Pressure Generation and Control System

Simulink block diagram of the left ventricular pressure generation and control system is given in Figure B.16.

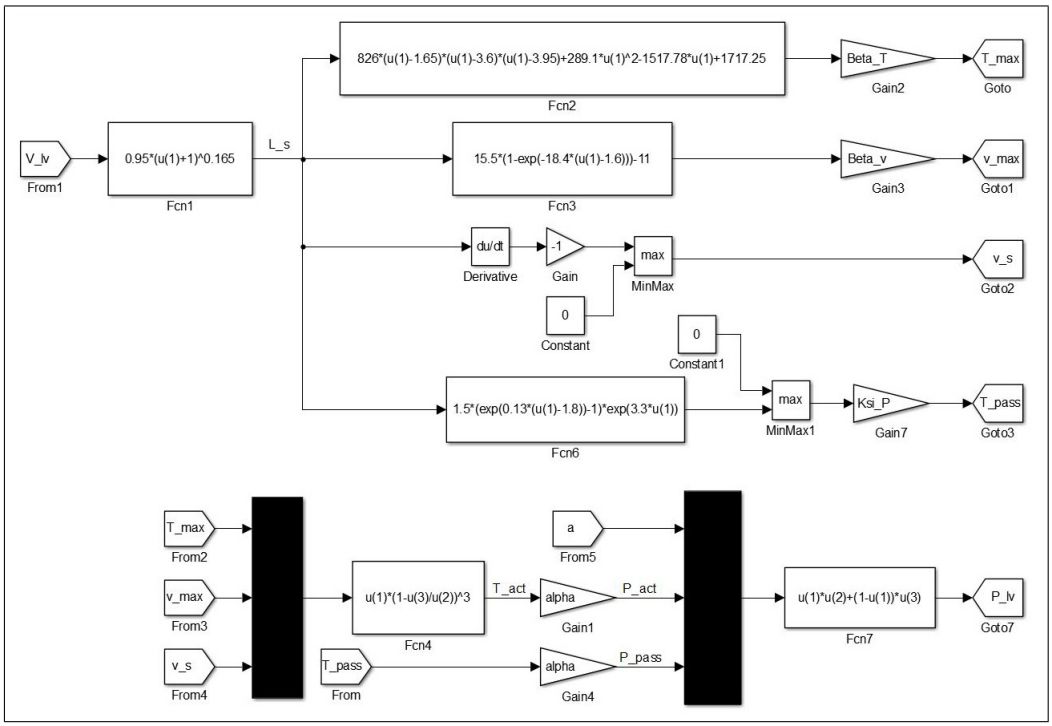

Figure B.16 Block diagram of the left ventricular pressure generation and control system

B.3.2 Block Diagram of Right Ventricular Pressure Generation and Control System

Simulink block diagram of the right ventricular pressure generation and control system is given in Figure B.17.

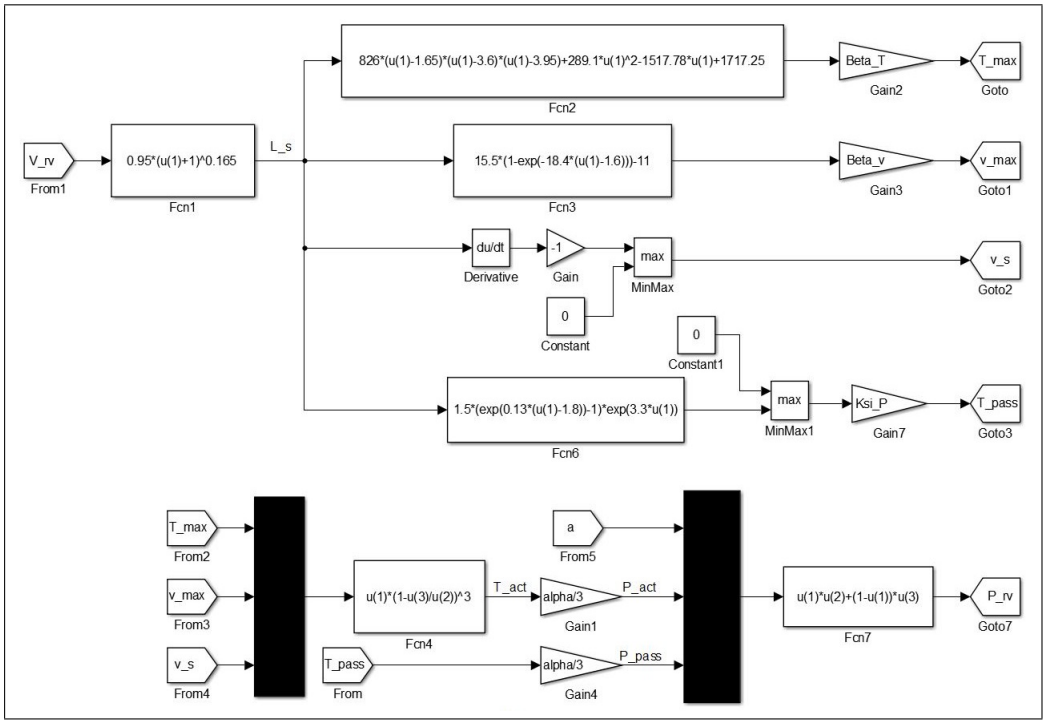

Figure B.17 Block diagram of the right ventricular pressure generation and control system

B.4 Block Diagram of Coronary Blood Flow Control System

Simulink block diagram of the coronary blood flow and control system is given in Figure B.18.

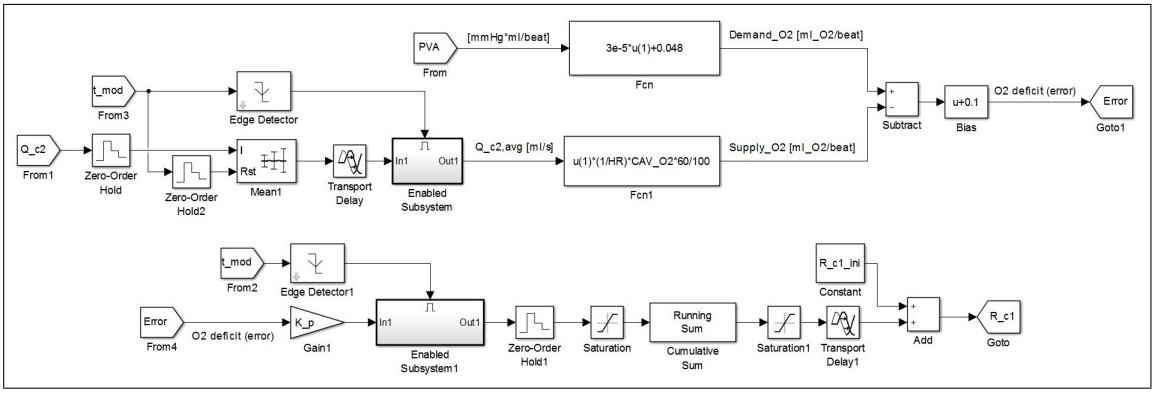

Figure B.18 Block diagram of the coronary blood flow control system

APPENDIX C. NORMALIZATION OF TENSION-VELOCITY CURVE

Total tension (T) and peak velocity of shortening (ϑ) values for $l_p = 9.00$ mm from Figure 3.3 were individually identified in Table C.1.

Table C.1
Data points taken from Figure 5 in Sonnenblick (1965) for $l_p = 9.00$ mm [22]

Total Tension (g)	Peak Velocity of Shortening (mm/s)
0.3	17.67
0.8	13.60
1.3	11.32
1.8	9.79
2.3	8.73
2.8	7.78
3.3	7.14
3.8	6.72
4.3	6.30
4.8	5.98
5.3	5.50
5.8	5.93
6.3	4.76
6.8	4.39
7.3	4.07
7.8	3.70
8.3	3.33
8.8	3.07
9.8	2.43
13.6	0

A curve was fitted to the data using MATLAB/Curve Fitting Toolbox (R^2 = 0.99):

$$\vartheta = 11.61 \cdot e^{-1.09 \cdot T} + 36.28 \cdot e^{-22.3 \cdot 10^{-3} \cdot T} - 26.78 \tag{C.1}$$

As a result T_{max} and ϑ_{max} were calculated as 13.6 g and 21.11 mm/s, respectively.

Applying the same method to all other l_p curves, each curve was associated with an equation. The values in Equations C.2 through C.5 were calculated from data presented in Tables C.2 through C.5, respectively.

Table C.2
Data points taken from Figure 5 in Sonnenblick (1965) for l_p = 8.75 mm [22]

Total Tension (g)	Peak Velocity of Shortening (mm/s)
0.3	16.78
0.8	13.33
1.3	10.95
1.8	9.52
2.3	8.25
2.8	7.41
3.3	6.72
4.3	5.82
4.8	5.29
5.3	4.87
5.8	4.44
6.3	4.02
6.8	3.65
7.3	3.23
7.8	2.80
8.3	2.43
8.8	2.12
9.8	1.48

For $l_p = 8.75$ mm ($R^2 = 0.99$):

$$\vartheta = 10.62 \cdot e^{-1.012 \cdot T} + 28.78 \cdot e^{-33.42 \cdot 10^{-3} \cdot T} - 18.92 \tag{C.2}$$

As a result T_{max} and ϑ_{max} were calculated as 12.55 g and 20.48 mm/s, respectively.

Table C.3
Data points taken from Figure 5 in Sonnenblick (1965) for $l_p = 8.50$ mm [22]

Total Tension (g)	Peak Velocity of Shortening (mm/s)
0.3	16.51
0.8	12.22
1.3	9.79
1.8	8.41
2.3	7.20
2.8	6.24
3.3	5.66
3.8	5.08
4.3	4.55
4.8	4.02
5.3	3.44
5.8	2.96
6.3	2.54
6.8	2.01
7.3	1.48

For $l_p = 8.50$ mm ($R^2 = 0.99$):

$$\vartheta = 11.01 \cdot e^{-1.315 \cdot T} + 39.80 \cdot e^{-29.79 \cdot 10^{-3} \cdot T} - 30.80 \tag{C.3}$$

As a result T_{max} and ϑ_{max} were calculated as 8.61 g and 20.01 mm/s, respectively.

Table C.4
Data points taken from Figure 5 in Sonnenblick (1965) for l_p = 8.25 mm [22]

Total Tension (g)	Peak Velocity of Shortening (mm/s)
0.3	14.76
0.8	10.21
1.3	8.47
1.8	6.77
2.3	5.71
2.8	4.76
3.3	4.07
3.8	3.33
4.3	2.59
4.8	2.06
5.3	1.53

For l_p = 8.25 mm (R^2 = 0.99):

$$\vartheta = 14.95 \cdot e^{-0.19 \cdot T} + 8.70 \cdot e^{-2.417 \cdot T} - 4.53 \tag{C.4}$$

As a result T_{max} and ϑ_{max} were calculated as 6.28 g and 19.12 mm/s, respectively.

Table C.5
Data points taken from Figure 5 in Sonnenblick (1965) for l_p = 8.00 mm [22]

Total Tension (g)	Peak Velocity of Shortening (mm/s)
0.3	11.16
0.8	7.62
1.3	5.50
1.8	4.34
2.3	3.44
2.8	2.59
3.3	1.75
3.8	0.79

For l_p = 8.00 mm (R^2 = 0.99):

$$\vartheta = 7.855 \cdot e^{-2.059 \cdot T} + 40.08 \cdot e^{-48.02 \cdot 10^{-3} \cdot T} - 32.49 \tag{C.5}$$

As a result T_{max} and ϑ_{max} were calculated as 4.37 g and 15.45 mm/s, respectively.

For Equation C.1 through Equation C.5, normalized tension, T_n, and normalized velocity, ϑ_n, were calculated using Equation C.6 (Equation 3.53) and Equation C.7 (Equation 3.54), respectively.

$$T_n = \frac{T_{max} - T}{T_{max}} \tag{C.6}$$

$$\vartheta_n = \frac{\vartheta_{max} - \vartheta}{\vartheta_{max}} \tag{C.7}$$

These T_n and ϑ_n values were plotted against each other (Figure 3.4) and a curve was fitted through the points Equation C.8 (Equation 3.56) (R^2 = 0.98).

$$T_n = 1 - \vartheta_n^3 \tag{C.8}$$

APPENDIX D. PARAMETERS OF THE CARDIOVASCULAR CONTROL SYSTEMS

Parameters regarding the control systems were given in Table D.1.

Table D.1
Parameters of the control systems

Parameter	Value	Units	Reference
HR	60	beat/min	–
t_{rb}	0.38	sec	–
τ_c	0.007	sec^2	[3]
τ_r	0.003	sec^2	[3]
$R_{c1}[0]$	24	mmHg·s/ml	[51]
M	200	g	[60]
CAV_{O2}	13	mlO_2/dlBlood	[63]
bias	0.1	mlO_2/dlBlood	[3]
K_P	-40	mmHg·s·beat/mlO_2·mlBlood	–
α_{lv}	1	–	–
α_{rv}	1/3	–	–

APPENDIX E. TENSION-PRESSURE CONVERSION METHODS

Four tension-pressure conversion methods, Laplace Law for ellipsoid and cylinder, an augmented Laplace Law suggested by Falsetti et. al. (1970) [69], and a tension-pressure conversion method suggested by Arts et. al. (1991) [70], were explained in this chapter.

1. Utilization of Laplace Law assuming the left ventricle as a half ellipsoid with a circular cross-section in the equator:

General relationship between tension and pressure was given as:

$$P = \theta(V) \cdot T \tag{E.1}$$

where $\theta(V)$ is the volume-varying tension-pressure conversion coefficient.

For Laplace Law, $\theta(V)$ is directly and inversely proportional to inner radius (r_i) and myocardial wall thickness (w) of the ventricle, respectively. Therefore $\theta(V)$ can be calculated using basic geometric relationships, and assumed or calculated constraints.

Volume-varying tension-pressure conversion coefficient for half ellipsoid, $\theta_{le}(V)$, was defined as:

$$\theta_{le}(V) = \left(1 + \frac{r_{i,le}}{h_{le}}\right) \cdot \frac{w_{le}}{r_{i,le}} \tag{E.2}$$

where $r_{i,le}$ is the inner cavity radius at the equator, h_{le} is the cavity height orthogonal to the equatorial cross-section, w_{le} is the myocardial wall thickness and the term $\left(1 + \frac{r_{i,le}}{h_{le}}\right)$ defines the prolate shape of the ellipsoid.

Basic geometrical relationships for ellipsoid were given as:

$$V_{lv} = \frac{4}{3} \cdot \pi \cdot r_{i,le}^2 \cdot h_{le} \tag{E.3}$$

$$r_{o,le} = r_{i,le} + w_{le} \tag{E.4}$$

$$V_{w,le} = \frac{4}{3} \cdot \pi \cdot r_{o,le}^2 \cdot (h_{le} + w_{le}) - V_{lv} \tag{E.5}$$

where $r_{o,le}$ is the outer radius at the equator and $V_{w,le}$ is the myocardial wall volume, both of which were assumed to be constant.

The average values of $V_{w,le}$ and $r_{o,le}$ were calculated as 187.5 ml and 3.54 cm, respectively; using the geometrical relationships given above, constraints for inner radii and wall thicknesses at end-systole and -diastole given in Table E.1, and assuming end-systolic and -diastolic left ventricular volumes 50 ml and 140 ml, respectively.

Equations for w_{le}, h_{le} and $r_{i,le}$ were derived as:

$$w_{le} = r_{o,le} - r_{i,le} \tag{E.6}$$

$$h_{le} = \frac{3 \cdot V_{lv}}{4 \cdot \pi \cdot r_{i,le}^2} \tag{E.7}$$

$$\frac{4}{3} \cdot \pi r_{i,le}^3 + \frac{r_{i,le}^2}{r_{o,le}^2} \cdot (V_{w,le} + V_{lv}) - r_{o,le} \cdot r_{i,le}^2 - V_{lv} = 0 \tag{E.8}$$

respectively. Where the biggest real positive root of Equation E.8 was taken as the calculated value of $r_{i,le}$.

Table E.1
Left ventricular end-systolic and -diastolic inner cavity radii and myocardial wall thicknesses [75]

	Inner cavity radius (r_i) [cm]	Myocardial wall thickness (w) [cm]
End-systole	1.90	1.53
End-diastole	2.63	1.02

2. Utilization of Laplace Law assuming the left ventricle as a cylinder:

Volume-varying tension-pressure conversion coefficient for cylinder, $\theta_{lc}(V)$, was defined as:

$$\theta_{lc}(V) = \frac{w_{lc}}{r_{i,lc}} \tag{E.9}$$

where $r_{i,lc}$ is the inner cavity radius and w_{lc} is the myocardial wall thickness.

Basic geometrical relationships for cylinder were given as:

$$V_{lv} = \pi \cdot r_{i,lc}^2 \cdot h_{lc} \tag{E.10}$$

$$r_{o,lc} = r_{i,lc} + w_{lc} \tag{E.11}$$

$$V_{w,lc} = \pi \cdot r_{o,lc}^2 \cdot h_{lc} - V_{lv} \tag{E.12}$$

where h_{lc} is the height, $r_{o,lc}$ is the outer radius and $V_{w,lc}$ is the myocardial wall volume. Values of $r_{o,lc}$ and $V_{w,lc}$ were assumed to be constant.

The average values of $V_{w,lc}$ and $r_{o,lc}$ were calculated as 121.3 ml and 3.54 cm, respectively; using the geometrical relationships given above, constraints for inner radii and wall thicknesses at end-systole and -diastole given in Table E.1, and assuming end-systolic and -diastolic left ventricular volumes 50 ml and 140 ml, respectively.

Equations for w_{lc}, h_{lc} and $r_{i,lc}$ were derived as:

$$w_{lc} = r_{o,lc} - r_{i,lc} \tag{E.13}$$

$$h_{lc} = \frac{V_{w,lc} + V_{lv}}{\pi \cdot r_{o,lc}^2} \tag{E.14}$$

$$r_{i,lc} = \frac{V_{lv}}{\pi \cdot h_{lc}} \tag{E.15}$$

respectively.

3. Utilization of the augmented Laplace Law suggested by Falsetti et. al. (1970) assuming the left ventricle as a half sphere:

Relationship between tension and pressure was given by [69] as:

$$P = \left(\frac{2 \cdot w_{fs}}{r_{i,fs}} + \frac{w_{fs}^2}{r_{i,fs}^2} \right) \cdot T \tag{E.16}$$

where $r_{i,fs}$ is the inner cavity radius and w_{fs} is the myocardial wall thickness.

Therefore, volume-varying tension-pressure conversion coefficient, $\theta_{fs}(V)$, was defined as:

$$\theta_{fs}(V) = \frac{2 \cdot w_{fs}}{r_{i,fs}} + \frac{w_{fs}^2}{r_{i,fs}^2} \tag{E.17}$$

Basic geometrical relationships for sphere were given as:

$$V_{lv} = \frac{4}{3} \cdot \pi \cdot r_{i,fs}^3 \tag{E.18}$$

$$r_{o,fs} = r_{i,fs} + w_{fs} \tag{E.19}$$

$$V_{w,fs} = \frac{4}{3} \cdot \pi \cdot r_{o,fs}^3 - V_{lv} \tag{E.20}$$

where $r_{o,fs}$ is the outer radius and $V_{w,fs}$ is the myocardial wall volume. Value of $V_{w,fs}$ was assumed to be constant.

The average values of $V_{w,fs}$ was calculated as 134 ml; using the geometrical relationships given above, constraints for inner radii and wall thicknesses at end-systole and -diastole given in Table E.1.

Equations for w_{fs}, $r_{o,fs}$ and $r_{i,fs}$ were derived as:

$$w_{fs} = r_{o,fs} - r_{i,fs} \tag{E.21}$$

$$r_{o,fs} = \sqrt[3]{\frac{3 \cdot (V_{lv} + V_{w,fs})}{4 \cdot \pi}} \tag{E.22}$$

$$r_{i,fs} = \sqrt[3]{\frac{3 \cdot V_{lv}}{4 \cdot \pi}} \tag{E.23}$$

respectively.

4. Utilization of the tension-pressure relationship suggested by Arts et. al. (1991) assuming the left ventricle as a half ellipsoid with a circular cross-section in the equator:

Relationship between tension and pressure was given by [70] as:

$$P = \frac{1}{3} \cdot \ln\left(1 + \frac{V_{w,ae}}{V_{lv}}\right) \cdot T \tag{E.24}$$

where $V_{w,ae}$ is the myocardial wall volume, which was assumed to be constant.

Therefore, volume-varying tension-pressure conversion coefficient, $\theta_{ae}(V)$, was defined as:

$$\theta_{ae}(V) = \frac{1}{3} \cdot \ln\left(1 + \frac{V_{w,ae}}{V_{lv}}\right) \tag{E.25}$$

The average value of $V_{w,ae}$ was calculated as 187.5 ml, utilizing the same equations, constraints and assumptions as $V_{w,le}$.

REFERENCES

1. Bayezid, Ö., ed., *Kalp Yetmezliğinde Mekanik Dolaşım Destek Sistemleri*, Akdeniz Üniversitesi Yayınları, 2015.

2. "WHO methods and data sources for country–level causes of death 2000–2015," tech. rep., Department of Information, Evidence and Research WHO, Geneva, 2017.

3. Guyton, A., and J. Hall, *Textbook of Medical Physiology*, Guyton Physiology Series, Elsevier Saunders, 2006.

4. Iaizzo, P., *Handbook of Cardiac Anatomy, Physiology, and Devices, 2nd Edition*, Current Clinical Oncology, Humana Press, 2009.

5. Suga, H., K. Sagawa, and A. A. Shoukas, "Load independence of the instantaneous pressure–volume ratio of the canine left ventricle and effects of epinephrine and heart rate on the ratio," *Circulation Research*, Vol. 32, no. 3, pp. 314–322, 1973.

6. Shishido, T., K. Hayashi, K. Shigemi, T. Sato, M. Sugimachi, and K. Sunagawa, "Single-beat estimation of end–systolic elastance using bilinearly approximated time-varying elastance curve," *Circulation*, Vol. 102, no. 16, pp. 1983–1989, 2000.

7. Huxley, A. F., and R. Niedergerke, "Structural changes in muscle during contraction; interference microscopy of living muscle fibres," *Nature*, Vol. 173, no. 4412, pp. 971–973, 1954.

8. Huxley, H. E., and J. Hanson, "Changes in the cross–striations of muscle during contraction and stretch and their structural interpretation," *Nature*, Vol. 173, no. 4412, pp. 973–976, 1954.

9. Hill, A., "The heat of shortening and the dynamic constants of muscle," *Proceedings of the Royal Society of London B: Biological Sciences*, Vol. 126, no. 843, pp. 136–195, 1938.

10. Fung, Y. C., "Comparison of different models of the heart muscle," *Journal of Biomechanics*, Vol. 4, no. 4, pp. 289–295, 1971.

11. Pollack, G. H., "Maximum velocity as an index of contractility in cardiac muscle," *Circulation Research*, Vol. 26, no. 1, pp. 111–127, 1970.

12. Rhoades, R., and D. Bell, *Medical Phisiology: Principles for Clinical Medicine 4th Edition*, Lippincott LWW Health Library: Integrated Basic Sciences Collection, Wolters Kluwer Health, 2013.

13. Sonnenblick, E. H., "Force–velocity relations in mammalian heart muscle," *American Journal of Physiology*, Vol. 202, no. 5, pp. 931–939, 1962.

14. McMahon, T., *Muscles, Reflexes, and Locomotion*, Princeton Paperbacks, Princeton University Press, 1984.

15. Inbar, G., and D. Adam, "Estimation of muscle active state," *Biological Cybernetics*, Vol. 23, no. 2, pp. 61–72, 1976.

16. Siegel, J. H., and E. H. Sonnenblick, "Isometric time–tension relationships as an index of myocardial contractility," *Circulation Research*, Vol. 12, no. 6, pp. 597–610, 1963.

17. Sonnenblick, E. H., D. Spiro, and H. M. Spotnitz, "The ultrastructural basis of starling's law of the heart. the role of the sarcomere in determining ventricular size and stroke volume," *American Heart Journal*, Vol. 68, no. 3, pp. 336–346, 1964.

18. Spotnitz, H. M., E. H. Sonnenblick, and D. Spiro, "Relation of ultrastructure to function in the intact heart: sarcomere structure relative to pressure volume curves of intact left ventricles of dog and cat," *Circulation Research*, Vol. 18, no. 1, pp. 49–66, 1966.

19. Page, S. G., "Measurements of structural parameters in cardiac muscle," in *The Physiological Basis of Starling's Law of the Heart*, pp. 13–25, Associated Scientific Publishers, 1974.

20. Winegrad, S., "Functional implications of the resting sarcomere length–tension curve in living heart muscle," in *The Physiological Basis of Starling's Law of the Heart*, pp. 43–52, Associated Scientific Publishers, 1974.

21. Julian, F. J., and M. R. Sollins, "Sarcomere length–tension relations in living rat papillary muscle.," *Circulation Research*, Vol. 37, no. 3, pp. 299–308, 1975.

22. Sonnenblick, E. H., "Instantaneous force–velocity–length determinants in the contraction of heart muscle," *Circulation Research*, Vol. 16, no. 5, pp. 441–451, 1965.

23. Brutsaert, D. L., and E. H. Sonnenblick, "Force–velocity–length–time relations of the contractile elements in heart muscle of the cat," *Circulation Research*, Vol. 24, no. 2, pp. 137–149, 1969.

24. Parmley, W. W., L. Chuck, and E. H. Sonnenblick, "Relation of vmax to different models of cardiac muscle," *Circulation Research*, Vol. 30, no. 1, pp. 34–43, 1972.

25. Suga, H., "Total mechanical energy of a ventricle model and cardiac oxygen consumption," *American Journal of Physiology–Heart and Circulatory Physiology*, Vol. 236, no. 3, pp. H498–H505, 1979.

26. Suga, H., "Cardiac energetics: from Emax to pressure–volume area," *Clinical and Experimental Pharmacology and Physiology*, Vol. 30, no. 8, pp. 580–585, 2003.

27. Suga, H., "Ventricular energetics," *Physiological Reviews*, Vol. 70, no. 2, pp. 247–277, 1990.

28. Kolff, W. J., "Mock circulation to test pumps designed for permanent replacement of damaged hearts," *Cleveland Clinic Quarterly*, Vol. 26, pp. 223–229, 1959.

29. Donovan, F., "Design of a hydraulic analog of the circulatory system for evaluating artificial hearts," *Biomaterials, Medical Devices, and Artificial Organs*, Vol. 3, no. 4, pp. 439–449, 1975.

30. Cornhill, J., "An aortic–left ventricular pulse duplicator used in testing prosthetic aortic heart valves," *The Journal of Thoracic and Cardiovascular Surgery*, Vol. 73, no. 4, pp. 550–558, 1977.

31. Rosenberg, G., W. M. Phillips, D. L. Landis, and W. Pierce, "Design and evaluation of the pennsylvania state university mock circulatory system," *ASAIO Journal*, Vol. 4, no. 2, pp. 41–49, 1981.

32. Koenig, S. C., G. M. Pantalos, K. J. Gillars, D. L. Ewert, K. N. Litwak, and S. W. Etoch, "Hemodynamic and pressure–volume responses to continuous and pulsatile ventricular assist in an adult mock circulation," *ASAIO Journal*, Vol. 50, no. 1, pp. 15–24, 2004.

33. Pantalos, G. M., S. C. Koenig, K. J. Gillars, G. A. Giridharan, and D. L. Ewert, "Characterization of an adult mock circulation for testing cardiac support devices," *ASAIO Journal*, Vol. 50, no. 1, pp. 37–46, 2004.

34. Litwak, K. N., S. C. Koenig, R. C. Cheng, G. A. Giridharan, K. J. Gillars, and G. M. Pantalos, "Ascending aorta outflow graft location and pulsatile ventricular assist provide optimal hemodynamic support in an adult mock circulation," *Artificial Organs*, Vol. 29, no. 8, pp. 629–635, 2005.

35. Liu, Y., P. Allaire, H. Wood, and D. Olsen, "Design and initial testing of a mock human circulatory loop for left ventricular assist device performance testing," *Artificial Organs*, Vol. 29, no. 4, pp. 341–345, 2005.

36. Timms, D., M. Hayne, K. McNeil, and A. Galbraith, "A complete mock circulation loop for the evaluation of left, right, and biventricular assist devices," *Artificial Organs*, Vol. 29, no. 7, pp. 564–572, 2005.

37. Timms, D. L., S. D. Gregory, N. A. Greatrex, M. J. Pearcy, J. F. Fraser, and U. Steinseifer, "A compact mock circulation loop for the in vitro testing of cardiovascular devices," *Artificial Organs*, Vol. 35, no. 4, pp. 384–391, 2011.

38. Eken, E. G., "Design and control of left and right ventricles for cardiovascular system mock circuit," Master's thesis, Bahçeşehir University, Istanbul, Turkey, 2013.

39. Ottesen, J., M. Olufsen, and J. Larsen, *Applied Mathematical Models in Human Physiology*, SIAM e-books, Society for Industrial and Applied Mathematics (SIAM), 2004.

40. Westerhof, N., F. Bosman, C. J. De Vries, and A. Noordergraaf, "Analog studies of the human systemic arterial tree," *Journal of Biomechanics*, Vol. 2, no. 2, pp. 121–143, 1969.

41. Ding, X., and P. Frank, "Modelling, control and monitoring of circulatory systems with an artificial heart," *International Journal of Quality & Reliability Management*, Vol. 11, no. 2, pp. 41–50, 1994.

42. Mitsui, N., S. Fukunaga, T. Sueda, Y. Matsuura, P. Havlik, J. Trinkl, J.-L. Demunck, T. Mesana, and J.-R. Montiès, "Study of left ventricular bypass using wankel type semipulsatile blood pump," *Artificial Organs*, Vol. 22, no. 5, pp. 419–425, 1998.

43. Vollkron, M., H. Schima, L. Huber, and G. Wieselthaler, "Interaction of the cardiovascular system with an implanted rotary assist device: simulation study with a refined computer model," *Artificial Organs*, Vol. 26, no. 4, pp. 349–359, 2002.

44. Wu, Y., P. Allaire, G. Tao, H. Wood, D. Olsen, and C. Tribble, "An advanced physiological controller design for a left ventricular assist device to prevent left ventricular collapse," *Artificial Organs*, Vol. 27, no. 10, pp. 926–930, 2003.

45. Vrettos, A., "The importance of arterial compliance, when blood flows and pressures are assumed to be random processes," in *The Twenty-Fourth IASTED International Conference on Modelling, Identification and Control*, (Innsbruck, Austria), IASTED, 2005.

46. Hassani, K., M. Navidbakhsh, and M. Rostami, "Modeling of the aorta artery aneurysms and renal artery stenosis using cardiovascular electronic system," *Biomedical Engineering Online*, Vol. 6, no. 1, pp. 22–32, 2007.

47. Gregory, S. D., "Simulation and development of a mock circulation loop with variable compliance," Master's thesis, Queensland University of Technology, Brisbane, Australia, 2009.

48. Westerhof, N., J.-W. Lankhaar, and B. E. Westerhof, "The arterial windkessel," *Medical and Biological Engineering and Computing*, Vol. 47, no. 2, pp. 131–141, 2009.

49. Bruinsma, P., T. Arts, J. Dankelman, and J. Spaan, "Model of the coronary circulation based on pressure dependence of coronary resistance and compliance," *Basic Research in Cardiology*, Vol. 83, no. 5, pp. 510–524, 1988.

50. Garcia, D., P. G. Camici, L.-G. Durand, K. Rajappan, E. Gaillard, O. E. Rimoldi, and P. Pibarot, "Impairment of coronary flow reserve in aortic stenosis," *Journal of Applied Physiology*, Vol. 106, no. 1, pp. 113–121, 2009.

51. Arthurs, C. J., K. D. Lau, K. N. Asrress, S. R. Redwood, and C. A. Figueroa, "A mathematical model of coronary blood flow control: simulation of patient–specific three–dimensional hemodynamics during exercise," *American Journal of Physiology-Heart and Circulatory Physiology*, Vol. 310, no. 9, pp. H1242–H1258, 2016.

52. Baloa, L., J. Boston, and J. Antaki, "Elastance-based control of a mock circulatory system," *Annals of Biomedical Engineering*, Vol. 29, no. 3, pp. 244–251, 2001.

53. Loh, M., and Y.-C. Yu, "Feedback control design for an elastance-based mock circulatory system," in *Proceedings of American Control Conference*, Vol. 2, pp. 1639–1644, IEEE, 2004.

54. Colacino, F. M., F. Moscato, F. Piedimonte, G. Danieli, S. Nicosia, and M. Arabia, "A modified elastance model to control mock ventricles in real-time: numerical and experimental validation," *ASAIO Journal*, Vol. 54, no. 6, pp. 563–573, 2008.

55. Yu, Y.-C., and S. Gopalakrishnan, "Elastance control of a mock circulatory system for ventricular assist device test," in *Proceedings of American Control Conference*, pp. 1009–1014, IEEE, 2009.

56. Jewell, B., "The changing face of the length–tension relation," in *The Physiological Basis of Starling's Law of the Heart*, pp. 7–12, Associated Scientific Publishers, 1974.

57. Allen, D., and J. Kentish, "The cellular basis of the length–tension relation in cardiac muscle," *Journal of Molecular and Cellular Cardiology*, Vol. 17, no. 9, pp. 821–840, 1985.

58. Greger, R., and U. Windhorst, *Comprehensive Human Physiology: From Cellular Mechanisms to Integration*, Springer Berlin Heidelberg, 2013.

59. Hudsmith, L. E., S. E. Petersen, J. M. Francis, M. D. Robson, and S. Neubauer, "Normal human left and right ventricular and left atrial dimensions using steady state free precession magnetic resonance imaging," *Journal of Cardiovascular Magnetic Resonance*, Vol. 7, no. 5, pp. 775–782, 2005.

60. Helak, J. W., and N. Reichek, "Quantitation of human left ventricular mass and volume by two-dimensional echocardiography: in vitro anatomic validation," *Circulation*, Vol. 63, no. 6, pp. 1398–1407, 1981.

61. Haddad, F., S. A. Hunt, D. N. Rosenthal, and D. J. Murphy, "Right ventricular function in cardiovascular disease, part i," *Circulation*, Vol. 117, no. 11, pp. 1436–1448, 2008.

62. Barrett, K., S. Barman, S. Boitano, and H. Brooks, *Ganong's Review of Medical Physiology, 23th Edition*, LANGE Basic Science, Mcgraw-Hill, 2012.

63. Ganz, W., R. Donoso, H. Marcus, and H. Swan, "Coronary hemodynamics and myocardial oxygen metabolism during oxygen breathing in patients with and without coronary artery disease," *Circulation*, Vol. 45, no. 4, pp. 763–768, 1972.

64. Robinson, D. A., "Quantitative analysis of the control of cardiac output in the isolated left ventricle," *Circulation Research*, Vol. 17, no. 3, pp. 207–221, 1965.

65. Burkhoff, D., I. Mirsky, and H. Suga, "Assessment of systolic and diastolic ventricular properties via pressure–volume analysis: a guide for clinical, translational, and basic researchers," *American Journal of Physiology–Heart and Circulatory Physiology*, Vol. 289, no. 2, pp. H501–H512, 2005.

66. Kass, D. A., and R. Beyar, "Evaluation of contractile state by maximal ventricular power divided by the square of end–diastolic volume," *Circulation*, Vol. 84, no. 4, pp. 1698–1708, 1991.

67. Glower, D. D., J. A. Spratt, N. D. Snow, J. S. Kabas, J. W. Davis, C. Olsen, G. Tyson, D. Sabiston, and J. Rankin, "Linearity of the frank–starling relationship in the intact heart: the concept of preload recruitable stroke work.," *Circulation*, Vol. 71, no. 5, pp. 994–1009, 1985.

68. Pfisterer, M., A. Battler, and B. Zaret, "Range of normal values for left and right ventricular ejection fraction at rest and during exercise assessed by radionuclide angiocardiography," *European Heart Journal*, Vol. 6, no. 8, pp. 647–655, 1985.

69. Falsetti, H. L., R. E. Mates, C. Grant, D. G. Greene, and I. L. Bunnell, "Left ventricular wall stress calculated from one–plane cineangiography," *Circulation Research*, Vol. 26, no. 1, pp. 71–83, 1970.

70. Arts, T., P. Bovendeerd, F. W. Prinzen, and R. S. Reneman, "Relation between left ventricular cavity pressure and volume and systolic fiber stress and strain in the wall," *Biophysical Journal*, Vol. 59, no. 1, pp. 93–102, 1991.

71. Noldus, E. J., "Optimal control aspects of left ventricular ejection dynamics," *Journal of Theoretical Biology*, Vol. 63, no. 2, pp. 275–309, 1976.

72. Yamashiro, S., J. Daubenspeck, and F. Bennett, "Optimal regulation of left ventricular ejection pattern," *Applied Mathematics and Computation*, Vol. 5, no. 1, pp. 41–54, 1979.

73. Livnat, A., and S. M. Yamashiro, "Optimal control evaluation of left ventricular systolic dynamics," *American Journal of Physiology–Regulatory, Integrative and Comparative Physiology*, Vol. 240, no. 5, pp. R370–R383, 1981.

74. Munford, R. S., G. K. Mcmullan, and W. D. Love, "Circulating coronary blood volume," *Circulation Research*, Vol. 17, no. 2, pp. 155–159, 1965.

75. Haag, U., O. Hess, S. Maier, M. Jakob, K. Liu, D. Meier, R. Jenni, P. Boesiger, M. Anliker, and H. Krayenbuehl, "Left ventricular wall thickness measurements by magnetic resonance: a validation study," *The International Journal of Cardiac Imaging*, Vol. 7, no. 1, pp. 31–41, 1991.